A COMPARISON OF EXPERIMENTAL AND THEORETICAL RESULTS FOR ROTORDYNAMIC COEFFICIENTS OF FOUR ANNULAR GAS SEALS

prepared by
David Elrod, Research Assistant
Colby Nicks, Research Assistant

Principal Investigators
Dara W. Childs, Ph.D. P.E.
Clayton Nelson, Ph.D. P.E.

July 1985

TRC-Seals-5-85

Turbomachinery Laboratories
Mechanical Engineering Department

A COMPARISON OF EXPERIMENTAL AND THEORETICAL RESULTS FOR ROTORDYNAMIC COEFFICIENTS OF FOUR ANNULAR GAS SEALS

PROGRESS REPORT
NASA CONTRACT NAS8-33716

prepared by

David Elrod, Research Assistant

Colby Nicks, Research Assistant[1]

Principal Investigators
Dara W. Childs, Ph.D. P.E.
Clayton Nelson, Ph.D. P.E.

Texas A&M University

Turbomachinery Laboratories

Mechanical Engineering Department

College Station, Texas 77843

July 1985

TRC-Seals-5-85

[1]Now employed by Bell Helicopter, Fort Worth, Texas.

TABLE OF CONTENTS

LIST OF TABLES

NOMENCLATURE

A,B = Fourier coefficients for rotor motion

C,c = direct and cross-coupled damping coefficients (FT/L)

C_i = inlet seal clearance (L)

C_o = exit seal clearance (L)

$\overline{C}$ = average seal clearance (L)

e_o = displacement of seal rotor from centered position (L)

K,k = direct and cross-coupled stiffness coefficients (F/L)

$\overline{k}$ = entrance-loss coefficient

M,m = direct and cross-coupled added-mass coefficients (M)

m = fluid mass flow rate (M/T)

ns,ms = stator Hirs' coefficients

nr,mr = rotor Hirs' coefficients

p = fluid pressure (F/L_2)

q = taper parameter

R = seal radius (L)

R_a = $2\rho UC/\mu$ = nominal axial Reynolds number

U = mean fluid flow velocity (L/T)

X,Y = radial seal displacements (L)

γ = ratio of specific heats for air

ε_o = e_o / C_r = equilibrium eccentricity ratio

ρ = fluid density (M/L_3)

λ = fanning friction-factor

τ = fluid shear stress (F/L_2)

ω = shaft angular velocity (1/T)

Ω = shaft precessional velocity (1/T)

μ = fluid viscosity (FT/L_2)

INTRODUCTION

With turbomachinery design trends tending toward increased speeds and loadings, lighter weight, and reduced clearances between rotating and stationary parts, considerable concern with instability and synchronous response has arisen. Synchronous response refers to vibration of the turbomachine rotor assembly at a frequency coincident with the rotational speed. Characteristically, the vibration amplitude increases to a maximum at each critical speed (coincidence of the running speed with a rotor's damped natural frequency), and then decreases to a relatively steady level. Operation of turbomachines at rotational speeds above any of the critical speeds requires the rotor to traverse them during start-up and shut-down. Therefore, in order to limit the peak synchronous vibration levels, the machine designer aspires to introduce damping into the rotor system.

In contrast to synchronous vibration, "unstable" or "self-excited" motion is typically subsynchronous. This motion takes the form of whirling of the rotor shaft at a natural frequency less than the rotational speed. The exciting force for this whirling motion is a tangential force acting on the rotor due to some fluid or friction mechanism. This vibration often occurs with large amplitudes which sustain or grow as running speed increases. At best, this self-excited whirling prevents further speed increases; at worst, it results in damage to or catastrophic failure of the equipment. One of the rotordynamic force mechanisms which plays a role in self-excited

Journal Model: ASME Journal of Lubrication Technology

rotor motion and synchronous response is that of the forces developed by annular seals. Until recently, most investigations of annular seals in turbomachinery have been concerned with reducing the leakage of the working fluid through the seal (i.e., improving the sealing effect). However, recent experiences have shown that forces developed by these seals can have considerable influence on the stability and synchronous response of rotating machinery. Black et al. [1-3] have demonstrated the critical effects that forces developed by neck-ring and interstage seals have on the rotordynamic behavior of pumps. Also, stability difficulties with the Space Shuttle Main Engine (SSME) high-pressure fuel turbopump [4] have prompted further research into these forces developed by liquid seals.

Experiences have shown that various gas seal configurations can have similar influences on the rotordynamic behavior of turbomachinery. In the high-pressure oxygen turbopump of the SSME, for example, initial vibration problems were remedied by changing the turbine interstage seal from a stepped-labyrinth configuration to a convergent taper seal with a honeycomb stator and a smooth rotor [5]. A lack of experimental data to completely explain this and other gas seal behavior makes obvious the need for research in this area.

The purpose of this report is threefold. It describes the test facility and initial test program developed to experimentally measure the fluid forces induced by annular gas seals, it provides a comparison of theoretically predicted and experimentally obtained data for smooth and honeycomb seals, and it provides a comparison of experimental data from the tests of three smooth-rotor/smooth-stator seals. The leakage of the working fluid through the seal, the

pressure gradient along the seal length, entrance pressure-loss data, and rotordynamic coefficients provide a basis for comparison. A short discussion on seal theory is included, and various rotordynamic coefficient identification schemes are described. The work presented herein is intended to add to the rapidly expanding database on seal forces, and to determine the validity of one theoretical analysis for predicting those forces.

ANNULAR SEAL ANALYSIS REVIEW

As related to rotordynamics, seal analysis has the objective of determining the reaction forces acting on the rotor arising from shaft motion within the seal. Due to similarities between plain journal bearings and annular seals, seal analysis is generally based on governing equations which have previously been developed for bearings.

Annular seals and plain bearings are geometrically similar, but seals typically have radial clearance-to-radius ratios on the order of 0.005, versus C_r/R ratios of 0.001 for bearings. Due to seal clearances and pressure differentials, fully-developed turbulent flow normally exists. Also, seals are nominally designed to operate in a centered position. Journal bearings, on the other hand, have operating eccentricities which vary with running speed and load. Therefore, most of the rotordynamic work for bearings has been done to determine dynamic coefficient versus eccentricity relationships.

Two linearized seal models, expressed in terms of dynamic coefficients, have been suggested for the motion/reaction-force relationship. For small motions of the rotor about an arbitrary position in the seal, as shown in Fig.1, the relation can be written

$$-\begin{Bmatrix} F_X \\ F_Y \end{Bmatrix} = \begin{bmatrix} K_{XX}(\varepsilon_o) & K_{XY}(\varepsilon_o) \\ K_{YX}(\varepsilon_o) & K_{YY}(\varepsilon_o) \end{bmatrix} \begin{Bmatrix} X \\ Y \end{Bmatrix} + \begin{bmatrix} C_{XX}(\varepsilon_o) & C_{XY}(\varepsilon_o) \\ C_{YX}(\varepsilon_o) & C_{YY}(\varepsilon_o) \end{bmatrix} \begin{Bmatrix} \dot{X} \\ \dot{Y} \end{Bmatrix} + \begin{bmatrix} M_{XX}(\varepsilon_o) & M_{XY}(\varepsilon_o) \\ M_{YX}(\varepsilon_o) & M_{YY}(\varepsilon_o) \end{bmatrix} \begin{Bmatrix} \ddot{X} \\ \ddot{Y} \end{Bmatrix} \quad (1)$$

where the dynamic coefficients $\{K_{XX}, K_{YY}, C_{XX}, C_{YY}, M_{XX}, M_{YY}\}$ and $\{K_{XY}, K_{YX}, C_{XY}, C_{YX}, M_{XY}, M_{YX}\}$ represent the "direct" and "cross-coupled" stiffness, damping, and added-mass terms, respectively. These coefficients are functions of the equilibrium

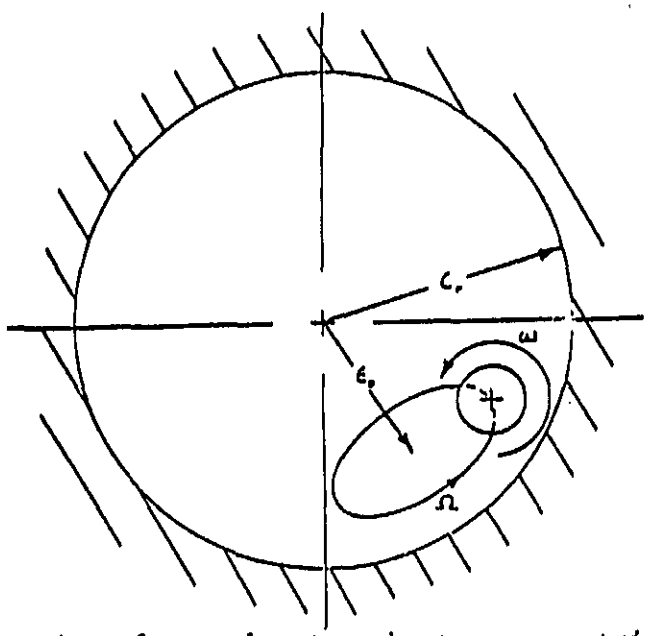

Fig. 1 Small motion of a seal rotor about an eccentric position; ω is the rotor spin speed, Ω is the precessional orbit frequency.

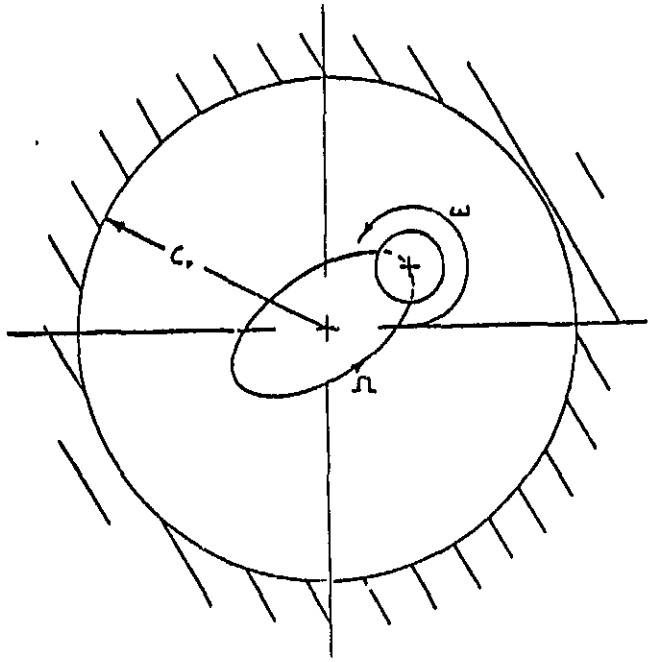

Fig. 2 Small motion of a seal rotor about a centered position; ω is the rotor spin speed, Ω is the precessional orbit frequency.

eccentricity ratio $\varepsilon_o = e_o / C_r$, where the eccentricity ratio ε_o equals the displacement (e_o) of the rotor from the centered position divided by the nominal radial clearance (C_r). The term "cross-coupled" refers to the coupling effect exhibited by the off-diagonal terms; specifically, motion in one plane introduces reaction forces in an orthogonal one. These cross-coupled terms arise from the fluid's circumferential velocity component, and show a strong dependency on both the magnitude and direction (with respect to rotor rotation) of the fluid velocity. This circumferential velocity component may arise from the prerotation of the fluid as it enters the seal due to some rotating element upstream, or it may develop as the fluid passes through the seal, with rotor shear forces "dragging" the viscous fluid around its periphery. The cross-coupled stiffness term usually produces a destabilizing force component, and therefore is of considerable interest. The cross-coupled damping and added-mass terms are generally much less influential than the cross-coupled stiffness term with respect to stability. For no fluid rotation, these cross-coupled terms are zero.

The second linearized seal model applies for small motions of the rotor about a centered position in the seal, as shown in Fig. 2 . This model can be expressed

$$-\begin{Bmatrix} F_X \\ F_Y \end{Bmatrix} = \begin{bmatrix} K & k \\ -k & K \end{bmatrix} \begin{Bmatrix} X \\ Y \end{Bmatrix} + \begin{bmatrix} C & c \\ -c & C \end{bmatrix} \begin{Bmatrix} \dot{X} \\ \dot{Y} \end{Bmatrix} + \begin{bmatrix} M & m \\ -m & M \end{bmatrix} \begin{Bmatrix} \ddot{X} \\ \ddot{Y} \end{Bmatrix} \quad (2)$$

where the dynamic coefficient matrices are skew-symmetric.

Theoretical work on annular seals has been done for both incompressible and compressible fluids. Black et al. [6] have

developed analytical "short-seal" solutions for incompressible seals, which account for circumferential fluid flow due to wall shear stresses but not pressure perturbations. The analysis employs a bulk-flow assumption and accounts for fluid prerotation as it enters the seal. Childs' [7] incompressible seal analysis provides "finite-length " solutions, in which both shear and pressure-induced flow are included. Childs' utilizes Hirs' [8] turbulent bulk-flow model, and accounts for inlet swirl as well as perturbations in axial and circumferential Reynolds numbers due to clearance perturbations.

Compressible flow in seals has been analyzed by Fleming [9, 10] and Nelson [11, 12]. Fleming presents a short seal solution for the leakage, direct stiffness, and direct damping coefficients for straight and tapered, smooth, annular gas seals, but does not include the cross-coupled damping terms. Nelson, whose analysis is used for comparison in this report, analyzes both smooth and surface-roughened annular seals in the straight and tapered configurations. An outline of Nelson's analysis is included in the section that follows.

NELSON'S ANALYSIS

Nelson [11, 12] has developed an analysis which provides both static and dynamic results for annular gas seals. The static results include fluid leakage through the seal, pressure gradient along the seal axis, and the fluid axial and circumferential velocities through the seal. Dynamic data provided by the analysis consists of the rotordynamic coefficients (direct and cross-coupled stiffness and damping terms) for small rotor motion about a centered position (equation (2)). Nelson assumes that the added-mass terms are negligible for gas seals, and, hence, equation(2) is written

$$-\begin{Bmatrix} F_X \\ F_Y \end{Bmatrix} = \begin{bmatrix} K & k \\ -k & K \end{bmatrix} \begin{Bmatrix} X \\ Y \end{Bmatrix} + \begin{bmatrix} C & c \\ -c & C \end{bmatrix} \begin{Bmatrix} \dot{X} \\ \dot{Y} \end{Bmatrix}. \tag{3}$$

Nelson utilizes a modified Hirs' [8] turbulent bulk-flow fluid model to develop governing axial and circumferential momentum equations, and his model is completed by the continuity and energy equations. Hirs' model defines the wall shear stress τ_w as

$$\tau_w = 1/2\ \rho U_m^2\ no(2\rho U_m H\ /\ \mu)^{mo} = 1/2\ \rho U_m^2\ noR_a^{mo} \tag{4}$$

where U_m is the mean flow velocity relative to the surface upon which the shear stress acts, and H is the local seal clearance. Hirs' formulation assumes that the surface roughness is the same on the rotor and stator. However, if the bulk-flow velocities relative to the rotor and stator are substituted into equation (4), the shear stresses at the rotor and stator are, respectively,

$$\tau_r = 1/2\ \rho U_r^2\ nr(2\rho U_r H\ /\ \mu)^{mr}$$

$$\tau_s = 1/2\ \rho U_s^2\ ns(2\rho U_s H\ /\ \mu)^{ms}$$

Hence, different surface roughnesses in the seal elements can be accounted for via the empirical coefficients mr, nr and ms, ns for the rotor and stator surfaces. These coefficients must be calculated from static-pressure-gradient test data, and are then provided as input parameters for Nelson's analysis.

Assuming small motion of the rotor about a centered position, Nelson uses a perturbation analysis similar to that employed by Childs [7] to develop zeroth and first-order perturbation equations. The zeroth-order solution represents a zero-eccentricity flow condition, with rotor rotation but without precession. This solution is iterative and yields the mass-leakage flow rate, and the axial distribution of pressure, axial velocity, density, and circumferential velocity. An iterative solution scheme is employed, using initial guesses for the zeroth-order seal entrance Mach number and entrance pressure-loss coefficient. The entrance-loss relationship is defined by

$$p_o(0) = \{1 + [(\gamma-1)(\bar{k}+1)M_o^2(0)] / 2\}^{\gamma/(1-\gamma)} \qquad (6)$$

where $p_o(0)$ is the seal entrance/reservoir pressure ratio and $M_o(0)$ is the entrance Mach number. The entrance Mach number is iteratively adjusted, and the loss coefficient k is recalculated according to a least-squares curve fit

$$\bar{k} + 1 = a + b(R_a)^c \qquad (7)$$

for a given seal. In equation (7), R_a is the axial Reynolds number, and a, b, and c are constants calculated from test data and provided as input parameters for Nelson's analysis. The iterative solution procedure for $M_o(0)$ and k continues until either:

1) the Mach number at the exit reaches unity and the exit pressure is greater than the sump pressure (choked flow), or
2) the exit pressure equals the sump pressure and the exit Mach number is less than unity (unchoked flow).

The pressure, density, and velocity distribution and their derivatives which are determined in the zeroth-order solution and the entrance-loss relationship determined from test data are used in defining coefficients of the first-order perturbation equations. These equations define the pressure, density, and axial and circumferential velocity perturbations due to rotor motion, and are transformed to sixteen ordinary differential equations in the axial coordinate z. The four physical boundary conditions required for the solution of these equations depend on the perturbation conditions that are specified at the seal entrance and exit. The inlet circumferential velocity perturbation is zero. Expansion of the entrance pressure-loss relationship of equation (6) yields a second boundary condition. For choked flow, the first-order perturbation in the exit Mach number is zero, while for unchoked flow, the first-order perturbation in the exit pressure is zero.

Application of these boundary conditions and numerical integration of the ordinary differential equations provides the first-order solution. Integration of the first-order pressure solution along and around the seal periphery yields the direct and cross-coupled stiffness and damping coefficients, K, k, C, and c, respectively.

The input parameters which can be varied in Nelson's analysis include:

1) reservoir pressure and temperature,

2) sump pressure,

3) seal geometry (i.e. radius, length, clearances),

4) rotor rotational speed and precession rate,

5) entrance circumferential velocity of the fluid,

6) rotor and stator surface roughness (Hirs constants),

7) empirical entrance-loss relationship,

8) fluid viscosity, gas constant, and ratio of specific heats.

It is apparent that a large amount of theoretical data can be generated to determine the influence that these various parameters have on the fluid forces in annular gas seals. However, there is a lack of experimental data with which to compare the results of Nelson's analysis. Currently, test results of Wachter and Benckert [13] exist for labyrinth seals, a special class of non-contacting seals which have stepped surfaces or "teeth" on the rotor, stator, or both. Experimental results for smooth and/or surface-roughened gas seals are limited to data from static tests of honeycomb seals also published by Wachter and Benckert. Hence, there was a need for a test apparatus which could be used to study the effects of the same variables provided for in Nelson's analysis. The experimental data generated by such an apparatus would be valuable for comparison to both Nelson's theories and others which may be developed in the future.

TEST CONCEPTS

A number of test programs have been implemented to measure the stabilizing and destabilizing fluid forces which are developed by turbomachinery elements. Some are concerned mainly with the study of seal forces, while others examine the forces developed by centrifugal pump impellers. In each case, reaction force and relative motion measurements are used for rotordynamic coefficient identification. Four general approaches have been employed, and will be reviewed here.

Wachter and Benckert [13] employ a static displacement method for determining stiffness coefficients. In this method, as shown in Fig. 3, the rotor is displaced statically to some measured eccentric position, while an axial pressure differential forces the working fluid past the seal. By measuring the reaction force components which are parallel and perpendicular to the static displacement vector, the direct and cross-coupled stiffnesses can be determined. Referring to equation (2) for small rotor motion about a centered position, a static rotor displacement in the X-direction yields

$$K = -F_X/e_o \ , \ k = F_Y/e_o \tag{8}$$

Since this static displacement method has no dynamic motion, no damping or added-mass terms can be evaluated.

A second approach to rotordynamic coefficient identification is utilized by Childs [14]. Depicted in Fig. 4, this method uses a circular orbit of the rotor within the seal. The rotor is mounted eccentrically on a shaft which rotates. Thus, the rotor precesses in a circular orbit at the same rate and direction as shaft rotation. This synchronous precession provides for the determination of the

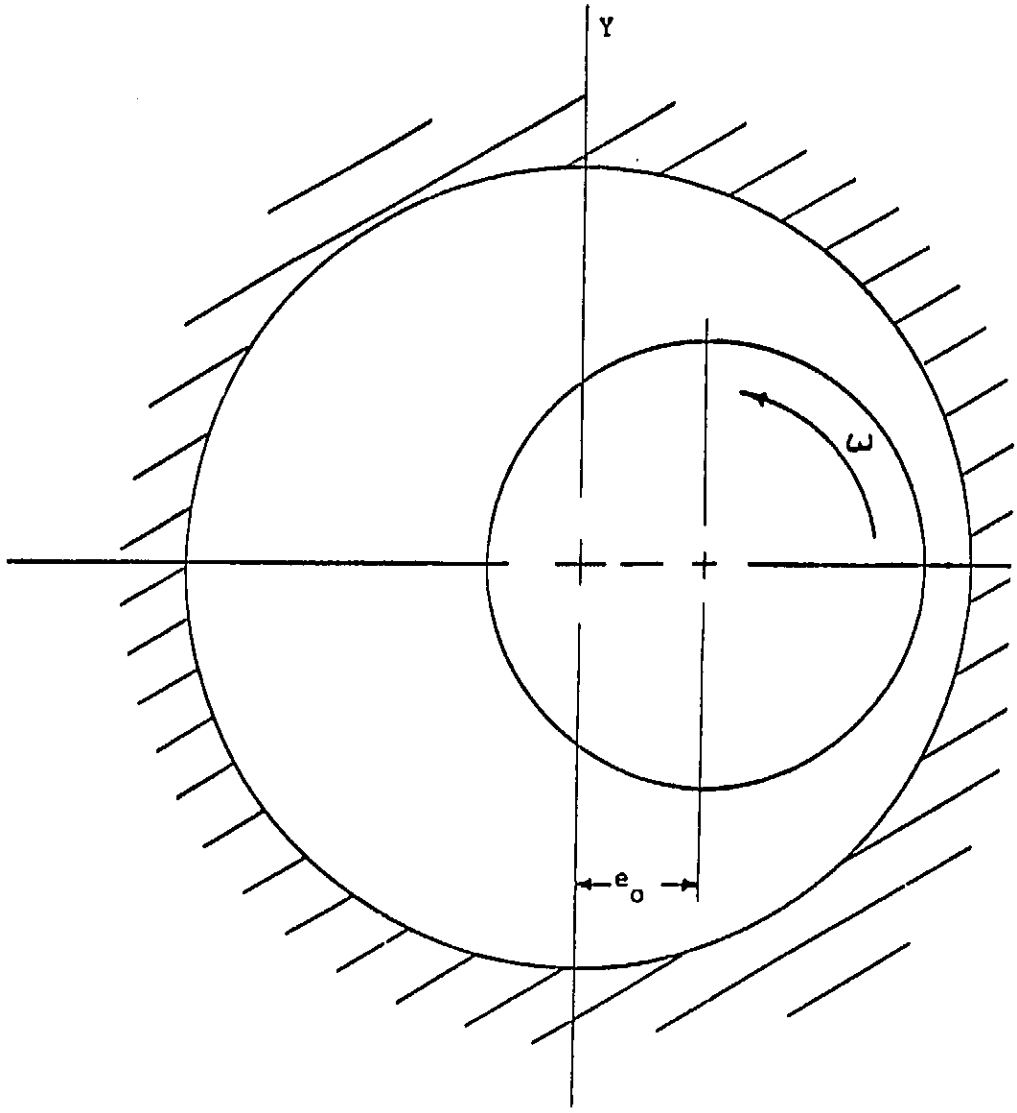

Fig. 3 Static displacement method used for stiffness determination.

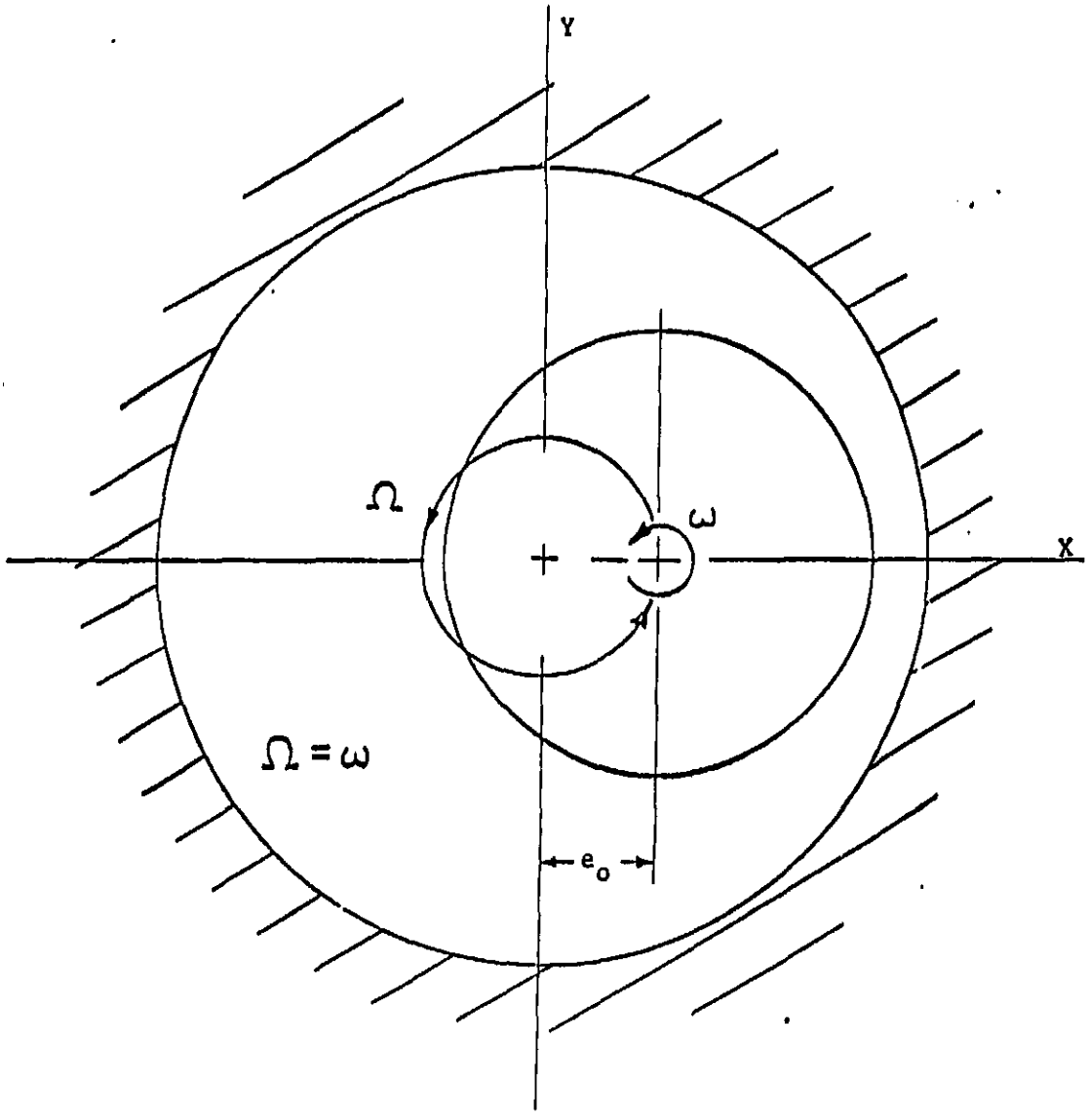

Fig. 4 Synchronous rotation and precession method used for equivalent coefficient identification.

radial and tangential components of the seal reaction force. The F_r and F_t components are obtained through integration of the measured pressure distribution along and around the seal periphery. Expressing measured rotor motion as

$$X = e_o \cos(\omega t)$$
$$Y = e_o \sin(\omega t) \tag{9}$$

for small circular orbit of radius e_o and precessional frequency $\omega=\Omega$, and substituting into equation (2) yields the radial and tangential force coefficient definitions

$$F_r / e_o = M\omega^2 - c\omega - K = -K_{ef} + M_{ef}(\omega^2)$$
$$F_t / e_o = k - C\omega = -C_{ef}(\omega) \tag{10}$$

where the cross-coupled mass coefficient is assumed negligible with respect to the influence of k and C. Because the cross-coupled coefficients k and c are linear functions of ω, identification of the individual dynamic coefficients is not possible in this method. However, equivalent direct stiffness, damping, and added-mass coefficients can be calculated as indicated in equation (10).

Independent rotation and precession control, as shown in Fig. 5, is a third testing method which is currently employed both in impeller and seal studies [15], [16], [17]. Various means are used to produce a circular orbit (precession) of the rotor or impeller at a rate different from its rotational speed. For a small circular orbit of radius e_o and precessional frequency Ω, the measured precessional motion of the rotor is

$$X = e_o \cos(\Omega t)$$
$$Y = e_o \sin(\Omega t)$$

The F_X and F_Y reaction force components are measured and can be

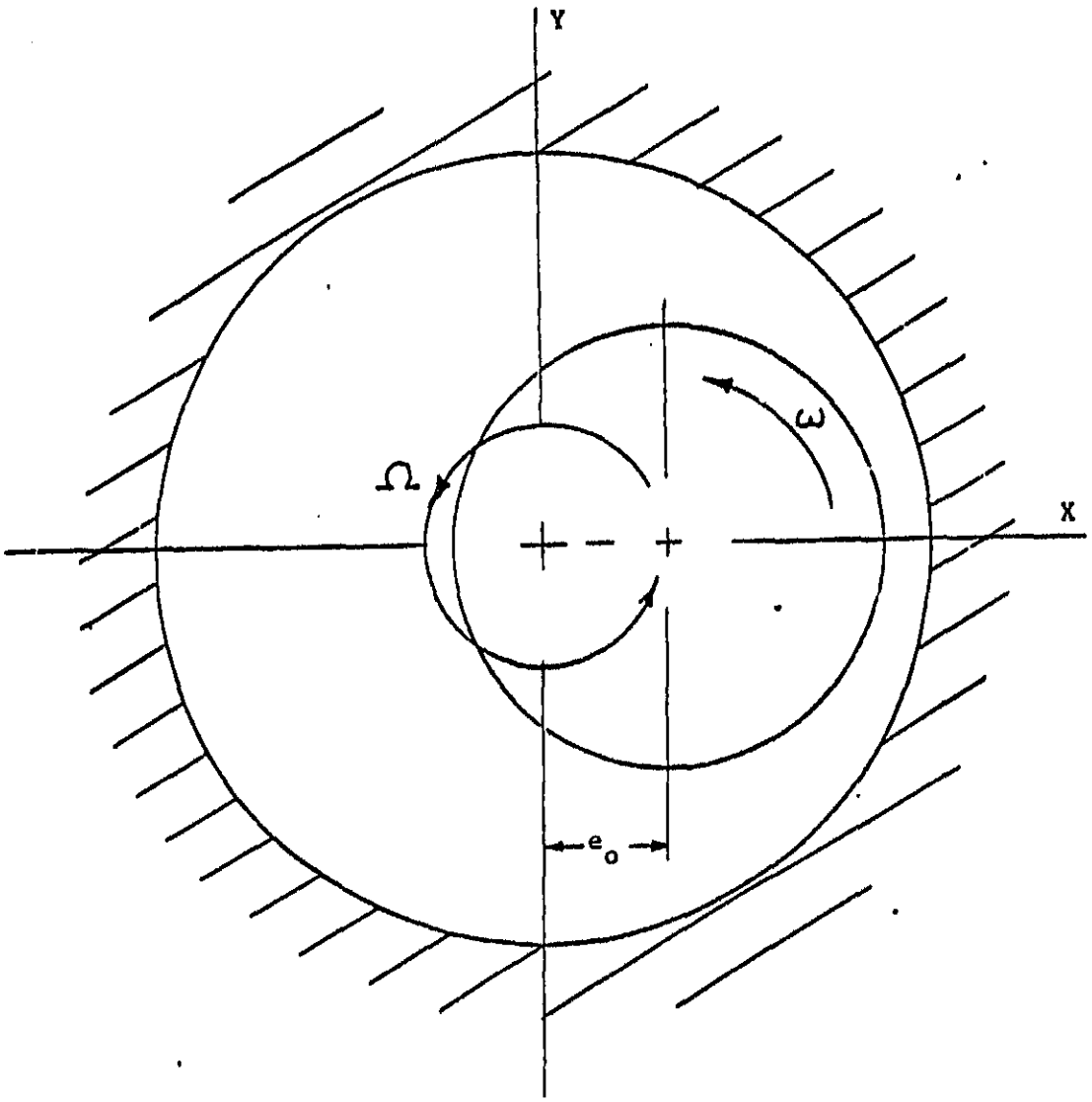

Fig. 5 Independent rotation and precession method used for coefficient identification.

expressed

$$F_X = F_{XS} \sin(\Omega t) + F_{XC} \cos(\Omega t)$$
$$F_Y = F_{YS} \sin(\Omega t) + F_{YC} \cos(\Omega t). \qquad (11)$$

By substituting these expressions into equation (2) and equating coefficients of sine and cosine terms, the following equations are obtained

$$-F_{XC} / e_o = K + c\Omega - M\Omega^2 \qquad -F_{YC} / e_o = -k + C\Omega + m\Omega^2$$
$$-F_{XS} / e_o = k + C\Omega - m\Omega^2 \qquad -F_{YS} / e_o = K + c\Omega + M\Omega^2 \qquad (12)$$

Hence, by measuring the reaction force components and rotor motion at two different precession frequencies, eight equations in six unknowns are obtained, and the rotordynamic coefficients can be calculated.

A fourth testing method has been used by Iino and Kaneko [18] for determining dynamic coefficients, and this same method is employed at the TAMU gas seal test facility. An external hydraulic shaker is used to impart translatory harmonic motion to the rotating seal, and rotor motion relative to the stator and the reaction force components acting on the stator are measured.

Fig. 6 shows the manner in which the rotor could be positioned and oscillated in order to identify the dynamic coefficients of the seal for small motion about e_o. If the added-mass terms are assumed negligible, equation (1) is rewritten

$$-\begin{Bmatrix} F_X \\ F_Y \end{Bmatrix} = \begin{bmatrix} K_{XX}(\varepsilon_o) & K_{XY}(\varepsilon_o) \\ K_{YX}(\varepsilon_o) & K_{YY}(\varepsilon_o) \end{bmatrix} \begin{Bmatrix} X \\ Y \end{Bmatrix} + \begin{bmatrix} C_{XX}(\varepsilon_o) & C_{XX}(\varepsilon_o) \\ C_{YX}(\varepsilon_o) & C_{YX}(\varepsilon_o) \end{bmatrix} \begin{Bmatrix} \dot{X} \\ \dot{Y} \end{Bmatrix} \qquad (13)$$

First, harmonic horizontal motion of the rotor is assumed, where

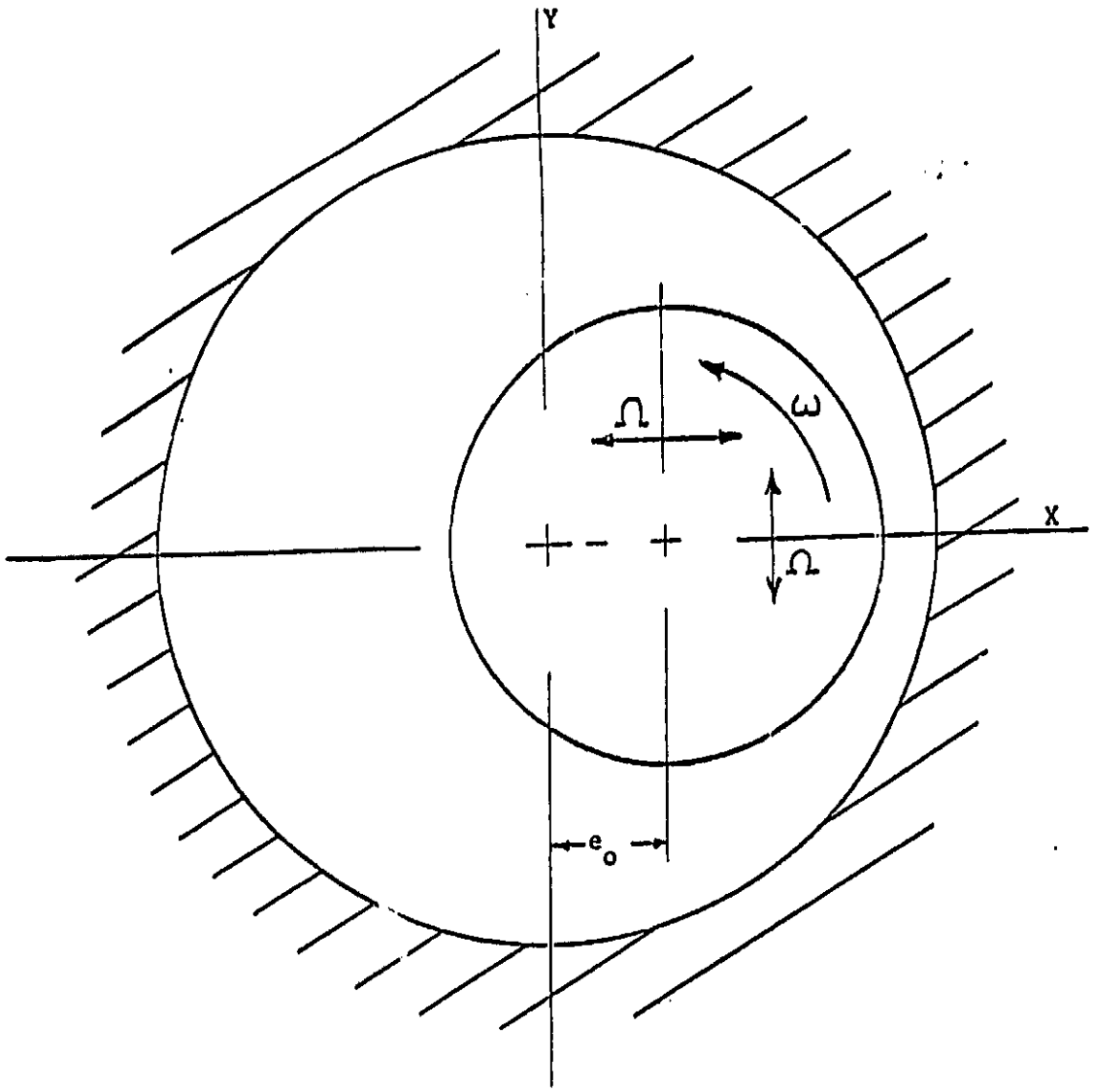

Fig. 6 External shaker method used for coefficient identification.

$$X = e_o + \sin(\Omega t) + B \cos(\Omega t)$$

$$\dot{X} = A\Omega \cos(\Omega t) - B\Omega \sin(\Omega t)$$

$$Y = \dot{Y} = 0 .$$

This yields small motion parallel to the static eccentricity vector, where Ω is the shaking frequency. In a similar fashion, the X and Y-direction force components can be expressed

$$\begin{aligned} F_X &= F_{XS} \sin(\Omega t) + F_{XC} \cos(\Omega t) \\ F_Y &= F_{YS} \sin(\Omega t) + F_{YC} \cos(\Omega t) . \end{aligned} \tag{14}$$

Substituting these expressions into equation (13) and equating coefficients of sine and cosine terms yields the following four equations

$$\begin{aligned} F_{XS} &= K_{XX} A - C_{XX} B \\ F_{XC} &= K_{XX} B + C_{XX} A \\ F_{YS} &= K_{YX} A - C_{YX} B \\ F_{XC} &= K_{YX} B + C_{YX} A . \end{aligned} \tag{15}$$

Solving this system of four equations in four unknowns defines the dynamic coefficients as

$$\begin{aligned} K_{XX}(\varepsilon_o) &= (F_{XC} B + F_{XS} A) / (A^2 + B^2) \\ K_{YX}(\varepsilon_o) &= (F_{YS} A + F_{YC} B) / (A^2 + B^2) \\ C_{XX}(\varepsilon_o) &= (F_{XC} A - F_{XS} B) / \Omega(A^2 + B^2) \\ C_{YX}(\varepsilon_o) &= (F_{YC} A - F_{YS} B) / \Omega(A^2 + B^2). \end{aligned} \tag{16}$$

Therefore, by measuring the reaction forces due to known rotor motion, determining the Fourier coefficients (A, B, F_{XS}, F_{XC}, F_{YS}, F_{YC}), and substituting into the above definitions, the indicated dynamic coefficients can be identified. If the rotor is shaken about a centered position, then the process is complete. Since the

linearized model has skew-symmetric stiffness and damping matrices, all of the coefficients are identified. If, however, the rotor is shaken about an eccentric position, as initially postulated, then it must be shaken vertically about that same point in order to complete the identification process.

Assuming harmonic vertical motion of the rotor, as defined by

$$X = e_o, \dot{X} = 0,$$

$$Y = A \sin(\Omega t) + B \cos(\Omega t),$$

$$\dot{Y} = A\Omega \cos(\Omega t) - B\Omega \sin(\Omega t),$$

yields oscillatory motion that is perpendicular to the assumed static eccentricity vector. A similar process as before results in the coefficient definitions

$$\begin{aligned} K_{YY}(\varepsilon_o) &= (F_{XS} A + F_{XC} B) / (A^2 + B^2) \\ K_{XY}(\varepsilon_o) &= -(F_{YC} B + F_{YS} A) / (A^2 + B^2) \\ C_{YY}(\varepsilon_o) &= (F_{XC} A - F_{XS} B) / \Omega(A^2 + B^2) \\ C_{XY}(\varepsilon_o) &= (F_{YS} B - F_{YC} A) / \Omega(A^2 + B^2) . \end{aligned} \tag{17}$$

All eight dynamic coefficients are thus determined by alternately shaking the rotor at one frequency Ω in directions which are parallel and perpendicular to the static eccentricity vector.

TEST APPARATUS OVERVIEW

Detailed design of the TAMU gas seal apparatus was carried out by J. B. Dressman of the University of Louisville. It is of the external shaker configuration, and the dynamic coefficient identification process is as described in the latter part of the preceding section.

Considering both the coefficient identification process and Nelson's analysis, some objectives for the design of the test apparatus are apparent. First, in order to determine the dynamic coefficients, the apparatus must provide the necessary rotor motion within the seal, and measurement of the reaction-force components due to this motion must be possible. Secondly, it would be advantageous (for purposes of comparison) if the apparatus could provide the same variable seal parameters afforded by Nelson's analysis (i.e., pressures, seal geometry, rotor rotational speed, fluid prerotation, and rotor/stator surface roughness). With this capability, the influence of each independent parameter could be examined and compared for correlation between theoretical predictions and experimental results.

With these design objectives in mind, the discussion of the test apparatus is presented in three sections. The first section, Test Hardware, describes how the various seal parameters are physically executed and controlled. For example, the manner in which the dynamic "shaking" motion of the seal rotor is achieved and controlled is described in this section. The second section, Instrumentation, describes how these controlled parameters, such as rotor motion, are measured. Finally, the Data Acquisition and Reduction section

explains how these measurements are used to provide the desired information.

TEST HARDWARE

This section deals only with the mechanical components and operation of the test apparatus. It provides answers to the following questions:

1) How is the static position of the seal rotor controlled?
2) How is the dynamic motion of the rotor executed and controlled?
3) How is compressed air obtained and supplied to the apparatus, and how is the pressure ratio across the seal controlled?
4) How is the incoming air prerotated before it enters the seal?
5) How are the seal rotor and stator mounted and replaced?
6) How is the seal rotor driven (rotated)?

Recalling the rotordynamic coefficient identification process described earlier, the external shaker method requires that the seal rotor be set in some static position and then be oscillated about that point. The test apparatus meets those requirements by providing independent static and dynamic displacement control, which are described below.

Static Displacement Control. The test apparatus is designed to provide control over the static eccentricity position both horizontally and vertically within the seal. The rotor shaft is suspended pendulum-fashion from an upper, rigidly mounted pivot shaft, as shown in Figs. 7 and 8. This arrangement allows a side-to-side (horizontal) motion of the rotor, and a cam within the pivot shaft allows vertical positioning of the rotor.

The cam which controls the vertical position of the rotor is

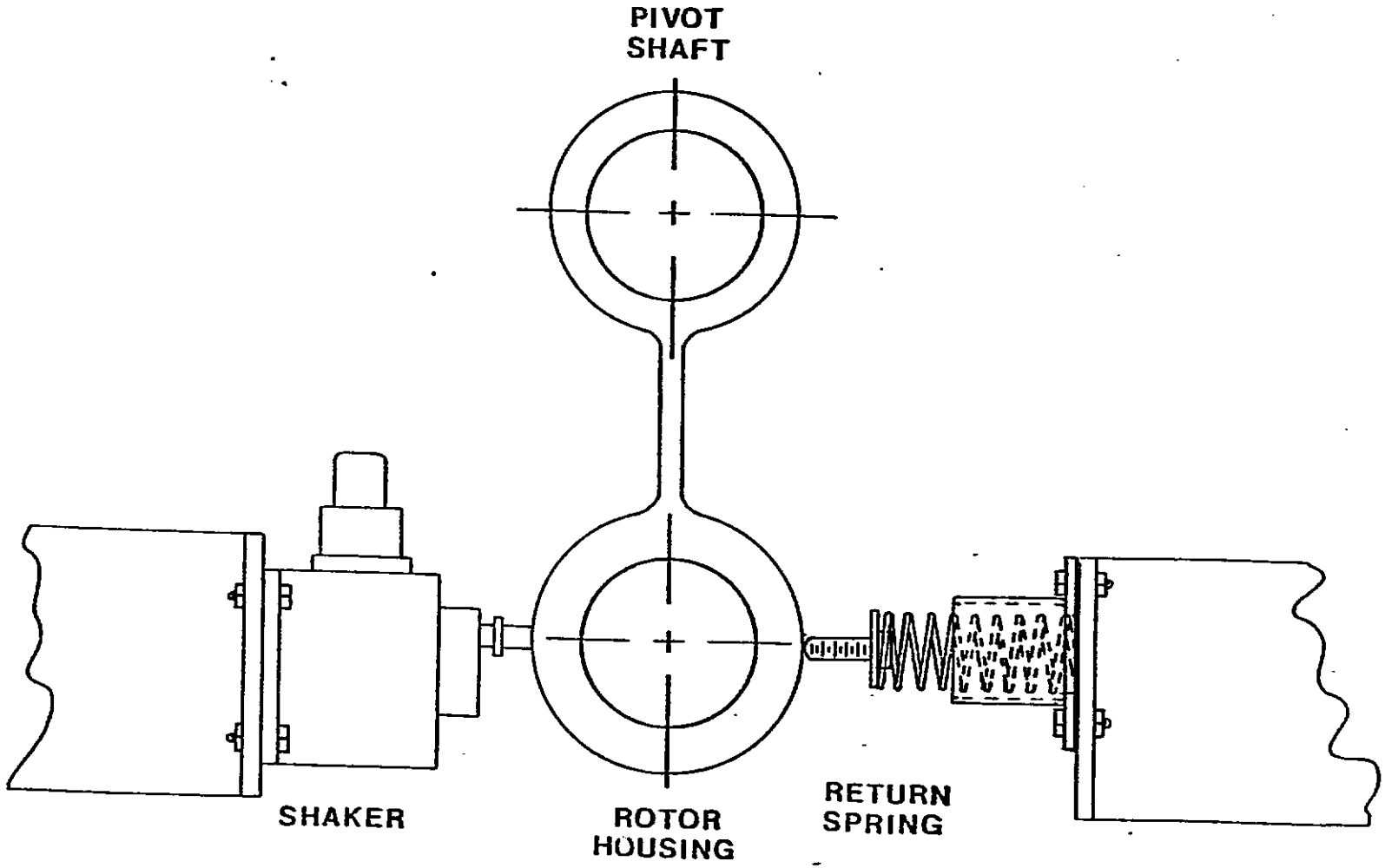

Fig. 7 Components used for static and dynamic displacement of seal rotor.

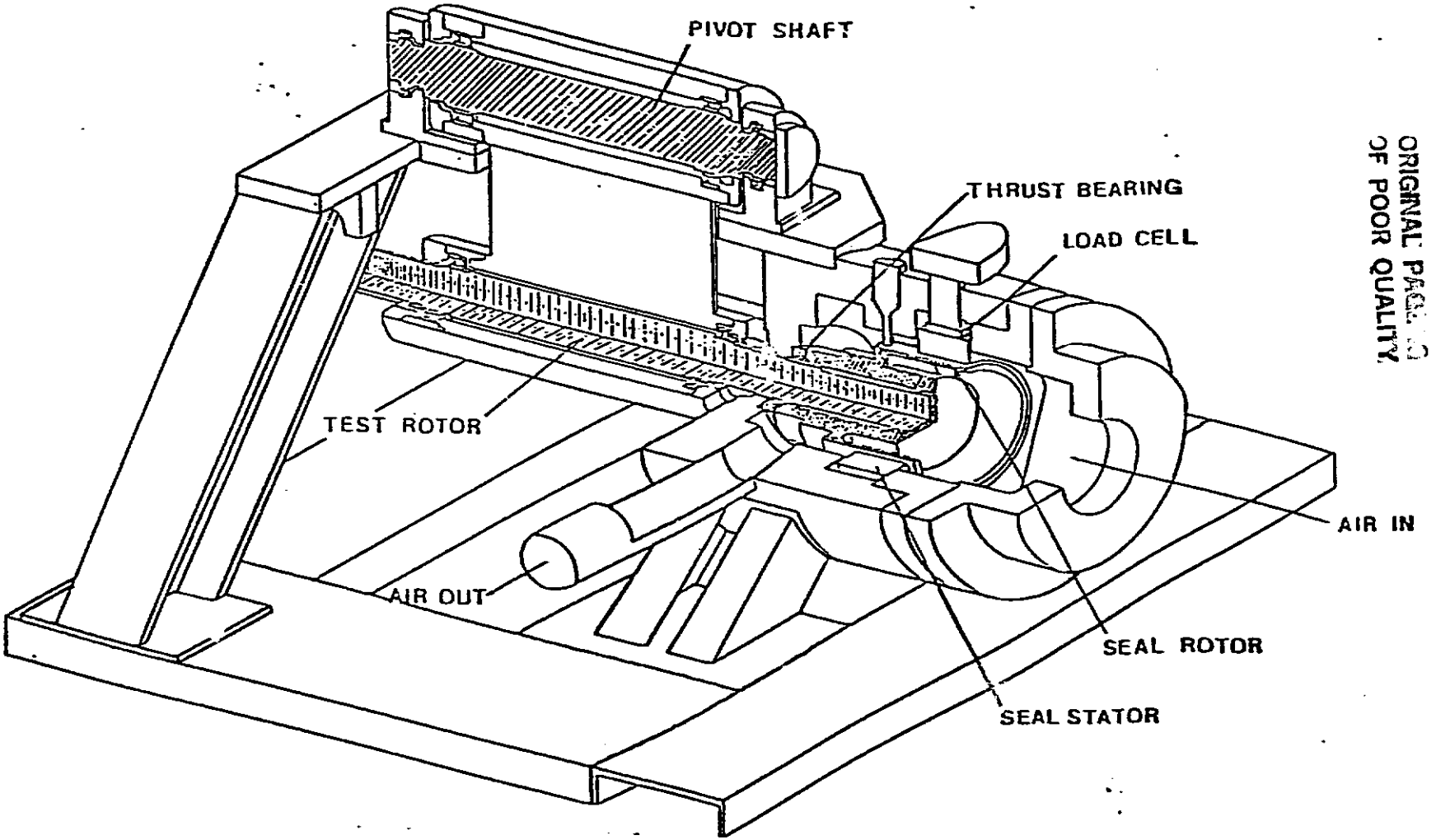

Fig. 8 Test apparatus.

driven by a remotely-operated DC gearhead motor, allowing accurate positioning of the rotor during testing. Horizontal positioning of the rotor is accomplished by a Zonic hydraulic shaker head and master controller, which provide independent static and dynamic displacement or force control. The shaker head is mounted on an I-beam support structure, and can supply up to 4450 N (1000 lbf) static and 4450 N dynamic force. As illustrated in Fig. 7, the shaker head output shaft acts on the rotor shaft bearing housing, and works against a return spring mounted on the opposite side of the bearing housing. The return spring maintains contact between the shaker head shaft and the bearing housing, thereby preventing hammering of the shaker shaft and the resulting loss of control over the horizontal motion of the rotor.

Dynamic Displacement Control. The dynamic motion of the seal rotor within the stator is horizontal. In addition to controlling the static horizontal position of the rotor, the Zonic shaker head moves the rotor through horizontal harmonic oscillations as the test is run. A Wavetek function generator provides the sinusoidal input signal to the Zonic controller, and both the amplitude and frequency of the rotor oscillations are controlled.

Although the test rig design provides for dynamic motion of the rotor only in the horizontal X-direction, all of the coefficients for either seal model (equation (3) or (13)) can still be determined. As Fig. 9 shows, the required rotor motion perpendicular to the static eccentricity vector can be accomplished in an equivalent manner by statically displacing it the same amount (e_o) in the vertical direction and continuing to shake horizontally.

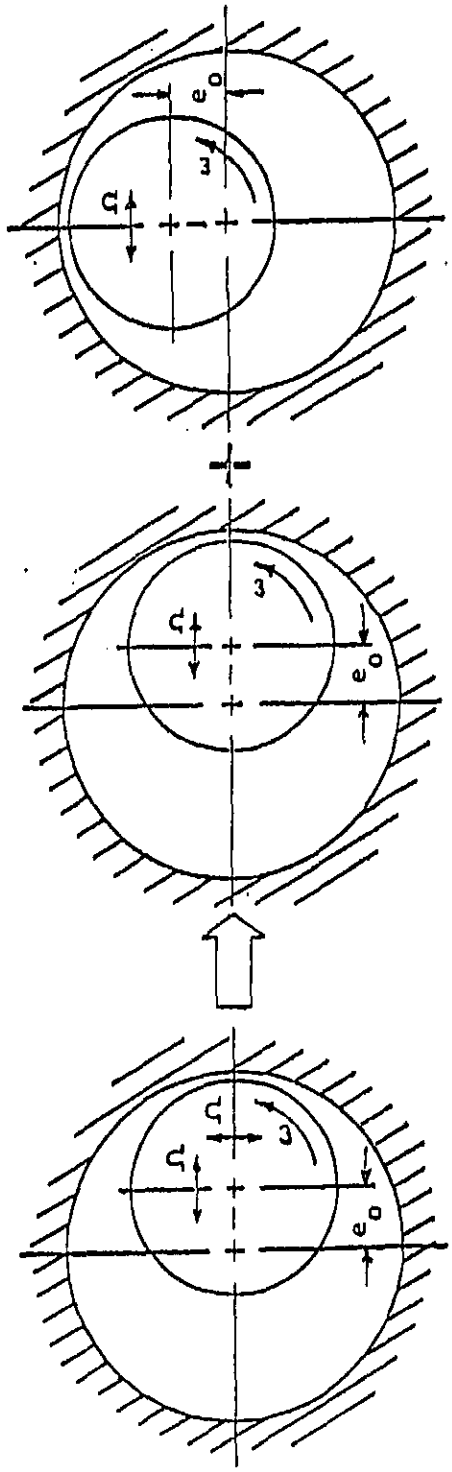

Fig. 9 Shaking motion used for rotordynamic coefficient identification.

In addition to providing control over the rotor's static position and dynamic motion, the test apparatus allows other seal parameters to be controlled independently, providing insight into the influence these parameters have on seal behavior. These parameters coincide with the variable input parameters for Nelson' analysis, and they include:

1) pressure ratio across the seal,
2) prerotation of the incoming fluid,
3) seal configuration, and
4) rotor rotational speed.

Pressure Ratio. The inlet air pressure and attendant mass flow rate through the seal are controlled by an electric-over-pneumatically actuated Masoneilan Camflex II flow control valve located upstream of the test section. An Ingersoll-Rand SSR-2000 single stage screw compressor rated at 34 m^3/min @ 929 kPa (1200 scfm @ 120 psig) provides compressed air, which is then filtered and dried before entering a receiver. Losses through the dryers, filters, and piping result in an actual maximum inlet pressure to the test section of approximately 825 kPa (105 psig) and a maximum flow rate of 27 m^3/min (950 scfm). A four-inch inlet pipe from the surge tank supplies the test rig, and after passing through the seal, the air exhausts to atmosphere through a manifold with muffler.

Inlet Circumferential Velocity Control. In order to determine the effects of fluid rotation on the rotordynamic coefficients, the test rig design also allows for prerotation of the incoming air as it enters the seal. This prerotation introduces a circumferential component to the air flow direction, and is accomplished by guide

vanes which direct and accelerate the flow towards the annulus of the seal. Three sets of guide vanes were used in testing all seals; one rotates the flow in the direction of rotor rotation, another introduces no fluid rotation, and the third rotates the flow opposite the direction of rotor rotation. These vanes were machined from brass disks. In addition, two sets of aluminum guide vanes were used in testing the constant 16 mil clearance smooth seal; one rotates the flow in the direction of rotor rotation, the other rotates the flow opposite the direction of rotor rotation. Due to a smaller annular clearance, the aluminum vanes cause a higher circumferential air velocity than the brass vanes for a given applied air pressure. Fig. 10 and Table 1 illustrate the vane configurations.

Seal Configuration. The design of the test rig permits the installation of various rotor/stator combinations. As shown in Figs. 11-16, the stator is supported in the test section housing by three Kistler quartz load cells in a trihedral configuration. Figs. 11-14 show the smooth-rotor/smooth-stator seals, while the smooth-rotor/honeycomb-stator seal is illustrated in Figs. 15 and 16. The seal rotor is press-fitted and secured axially by a bolt circle to the rotor shaft. Seals with different geometries (i.e., clearances, tapers, lengths) can be tested, as well as seals with different surface roughnesses. The replacement of these rotor/stator combinations can be accomplished with minimal downtime.

Rotational Speed. A Westinghouse 50-hp variable-speed electric motor drives the rotor shaft through a belt-driven jackshaft arrangement. This shaft is supported by two sets of Torrington hollow-roller bearings [19]. These bearings are extremely precise, radially

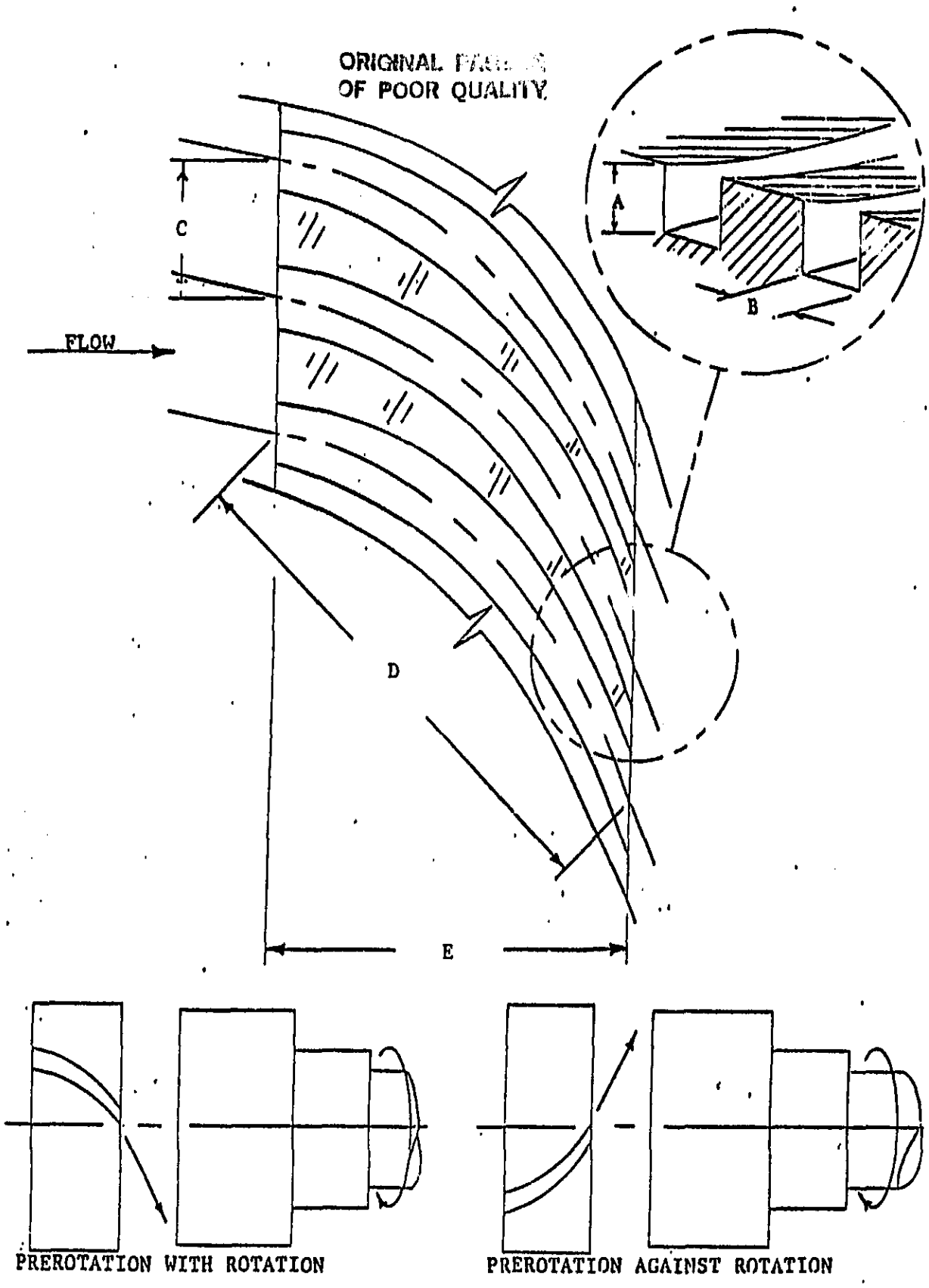

Fig. 10 Inlet guide vane detail.

Table 1. Inlet guide vane dimensions as illustrated in figure 10.

Vane material	Brass		Aluminum		Aluminum	
Swirl direction	Both		With Rotation		Against Rotation	
Dimensions	cm	(in)	cm	(in)	cm	(in)
A	0.615	(0.242)	0.216	(0.085)	0.216	(0.085)
B	0.335	(0.132)	0.358	(0.141)	0.427	(0.168)
C	2.54	(1.00)	2.42	(0.951)	2.42	(0.951)
D	8.89	(3.50)	8.00	(3.149)	8.00	(3.149)
E	6.03	(2.375)	5.87	(2.312)	5.87	(2.312)

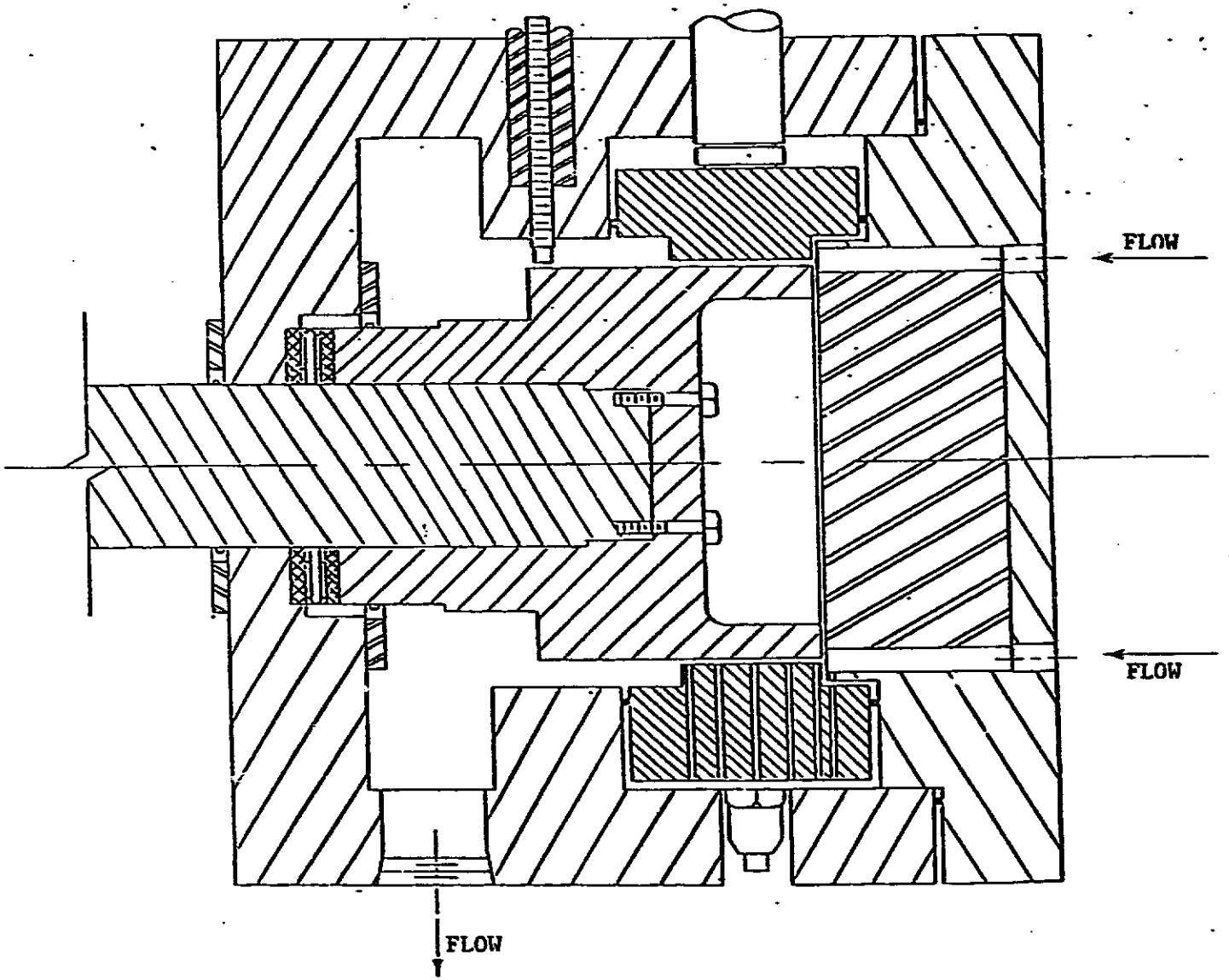

Fig. 11 Typical cross-sectional view of test section showing smooth stator.

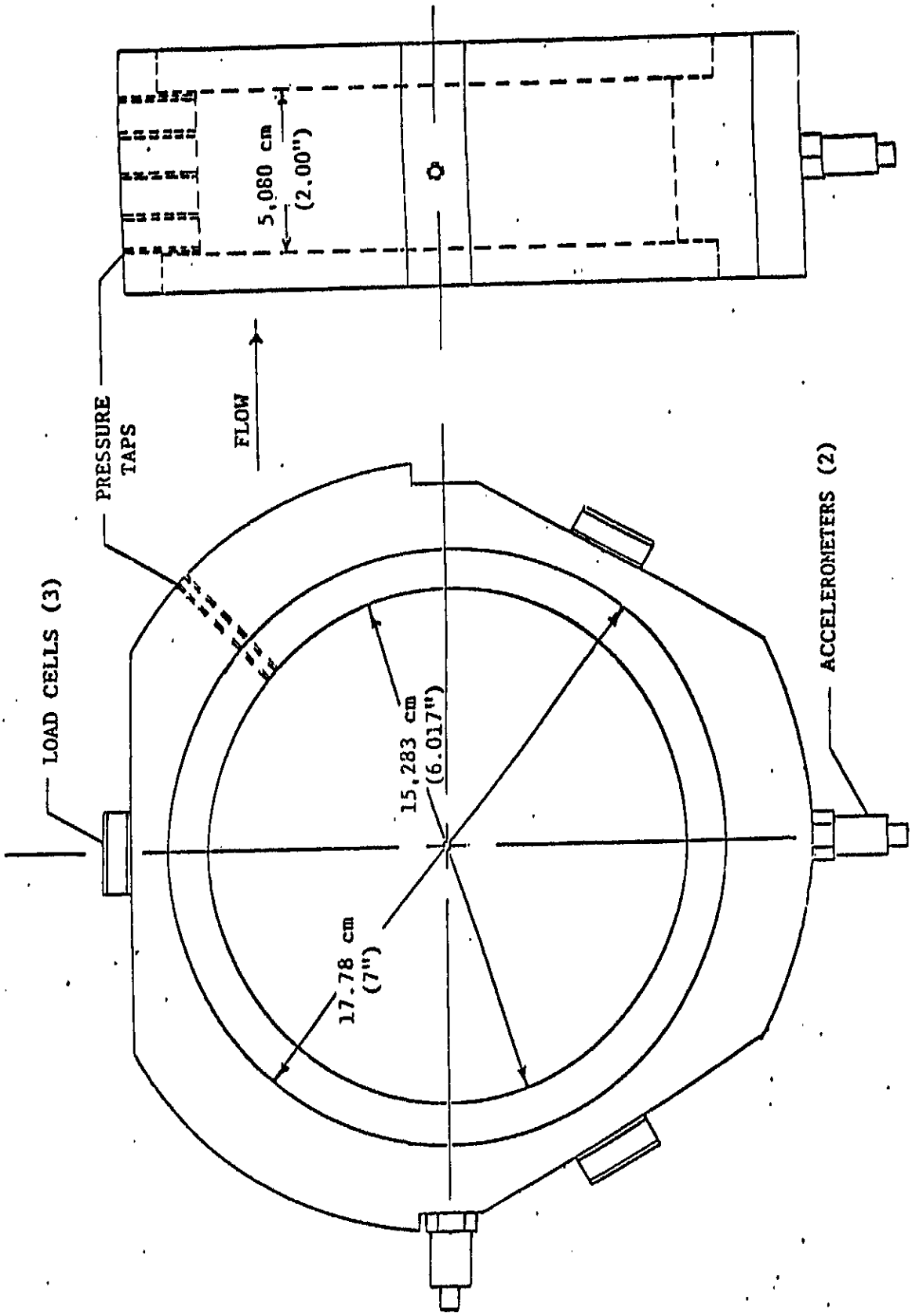

Fig. 12 Detail of constant diameter smooth stator #1.

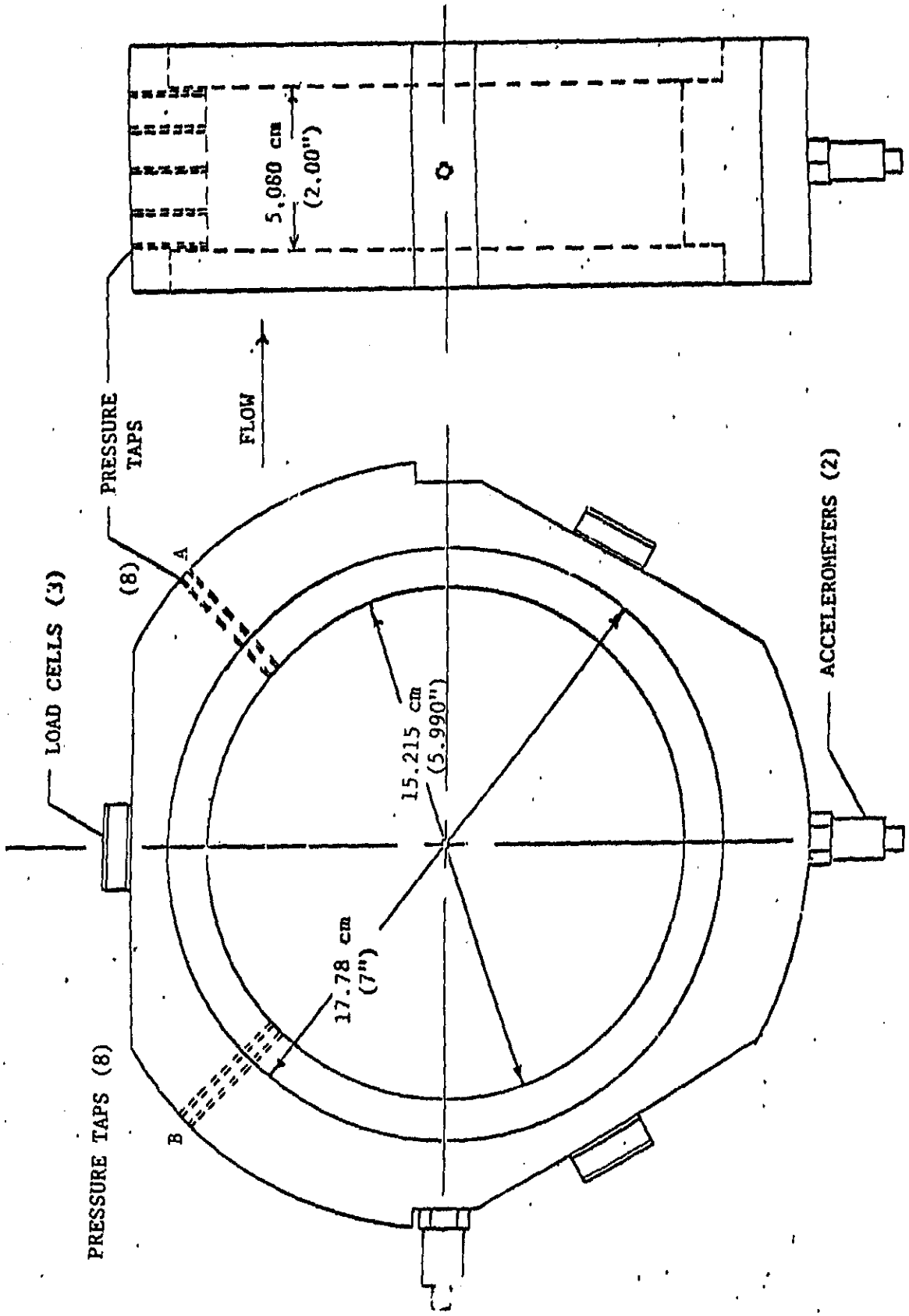

Fig. 13 Detail of constant diameter smooth stator #2.

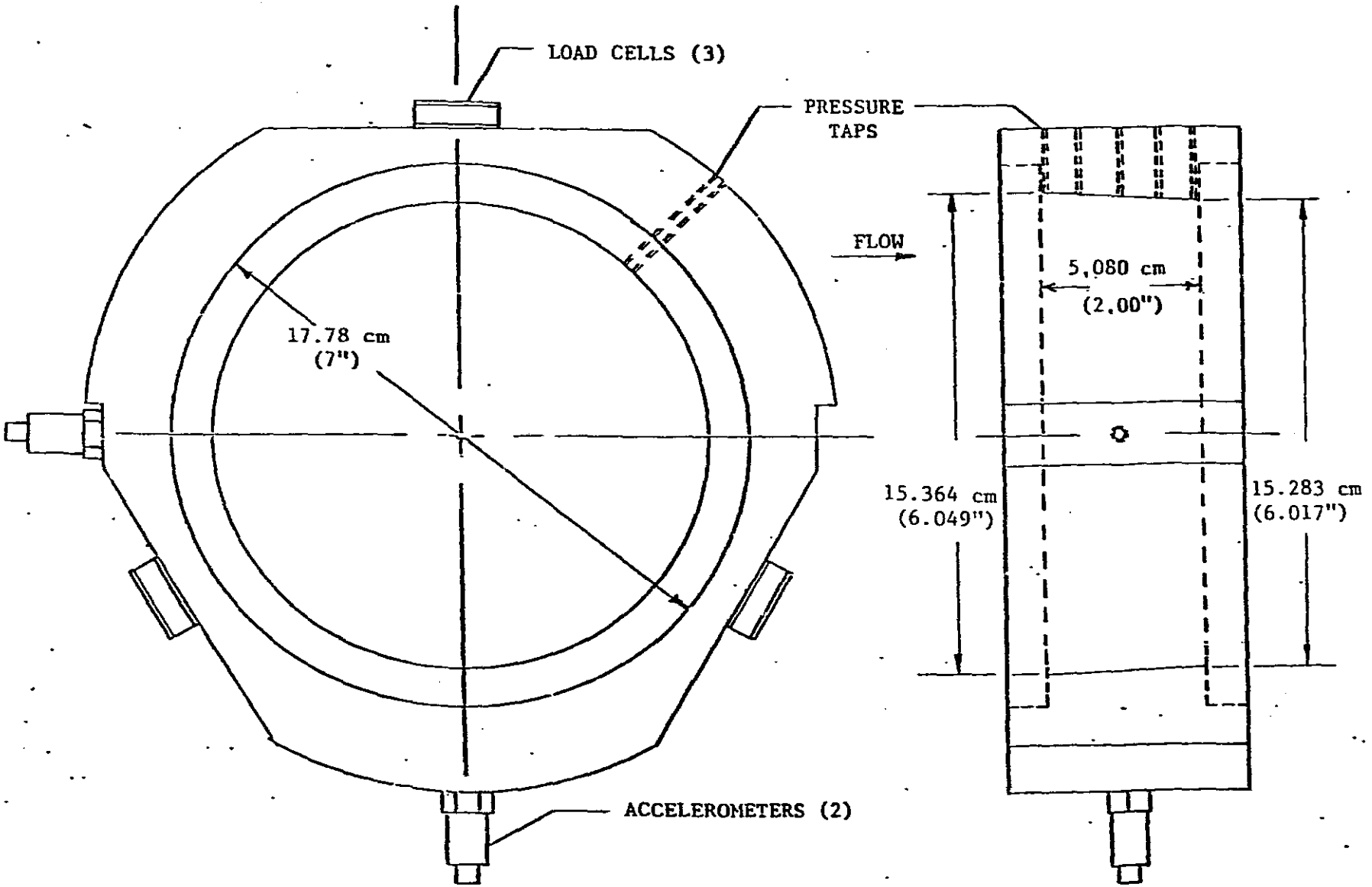

Fig. 14 Detail of tapered stator.

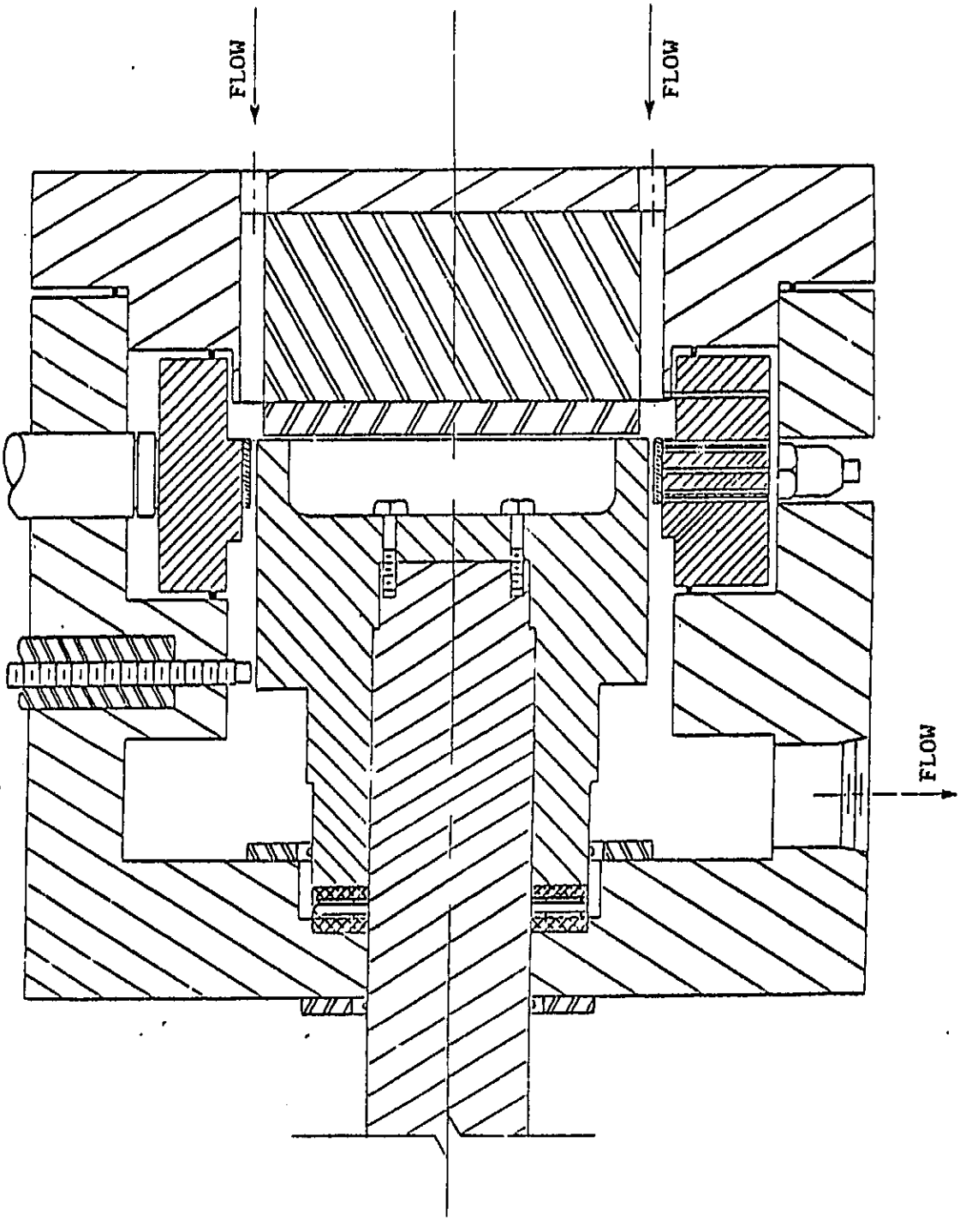

Fig. 15 Cross-sectional view of test section showing honeycomb stator.

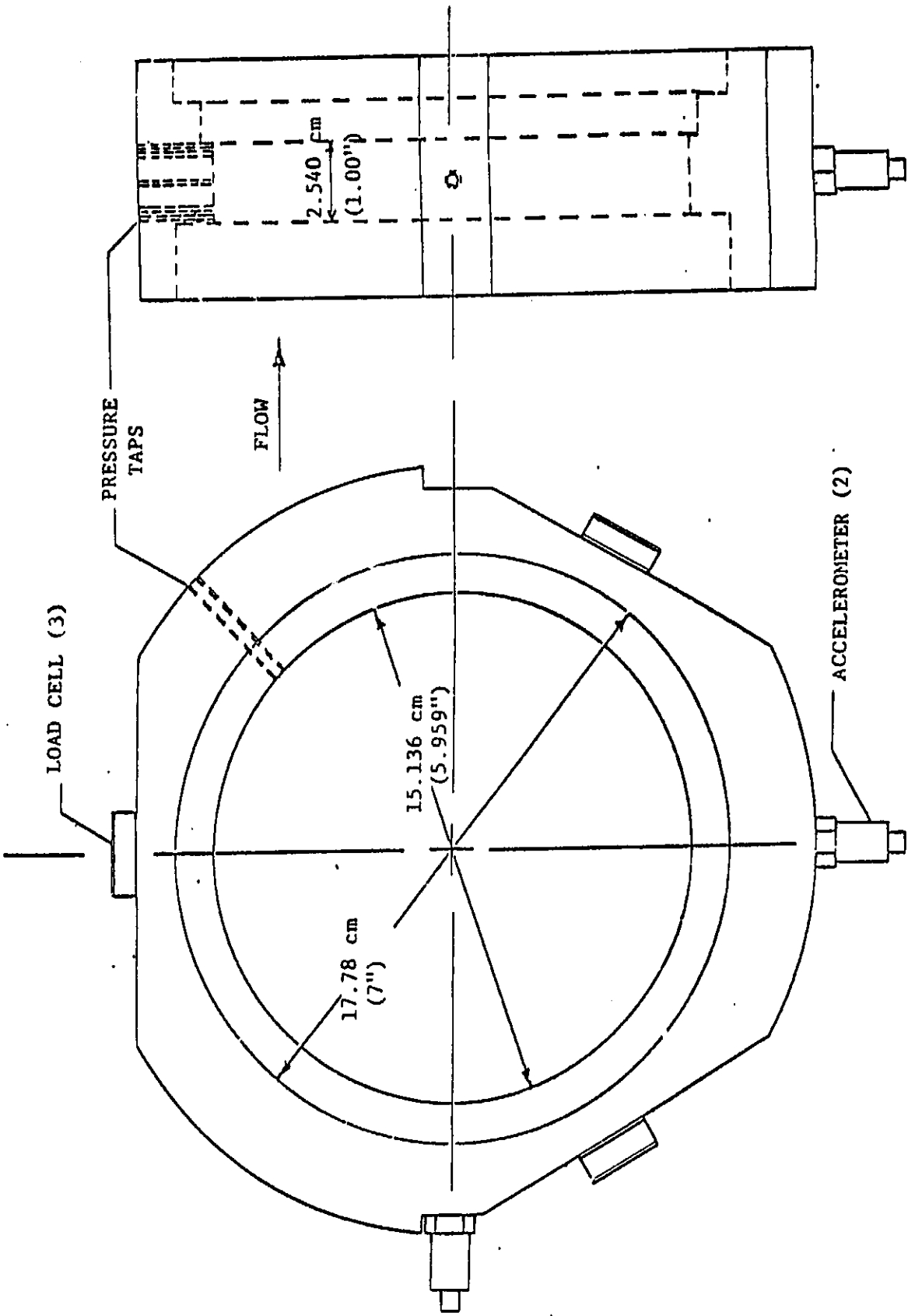

Fig. 16 Detail of honeycomb stator.

preloaded, and have a predictable and repeatable radial stiffness. Axial thrust due to the pressure differential across the seal is absorbed by a flat, roller-type caged thrust bearing at the rear of the rotor. Both the shaft and thrust bearings are lubricated by a positive-displacement gear-type oil pump.

Different jackshaft drive-pulleys can be fitted to provide up to a 4:1 speed increase from motor to rotor shaft, which would result in a rotor shaft speed range of 0-21,200 rpm. Current design limitations, however, prevent the attainment of this upper rotational speed. High bearing temperatures, reduction of interference in the rotor-shaft fitment due to inertia-induced radial growth of the rotor inside diameter, and excessive stresses in the drive-pulleys have served to limit shaft speed. The highest rotational speed attained at the time of this writing is 8500 rpm, although design modifications to allow higher speeds are underway.

To conclude this discussion of the test hardware, two views of the complete test apparatus are included. Fig. 17 shows the assembled rig, while an exploded view is provided in Fig. 18.

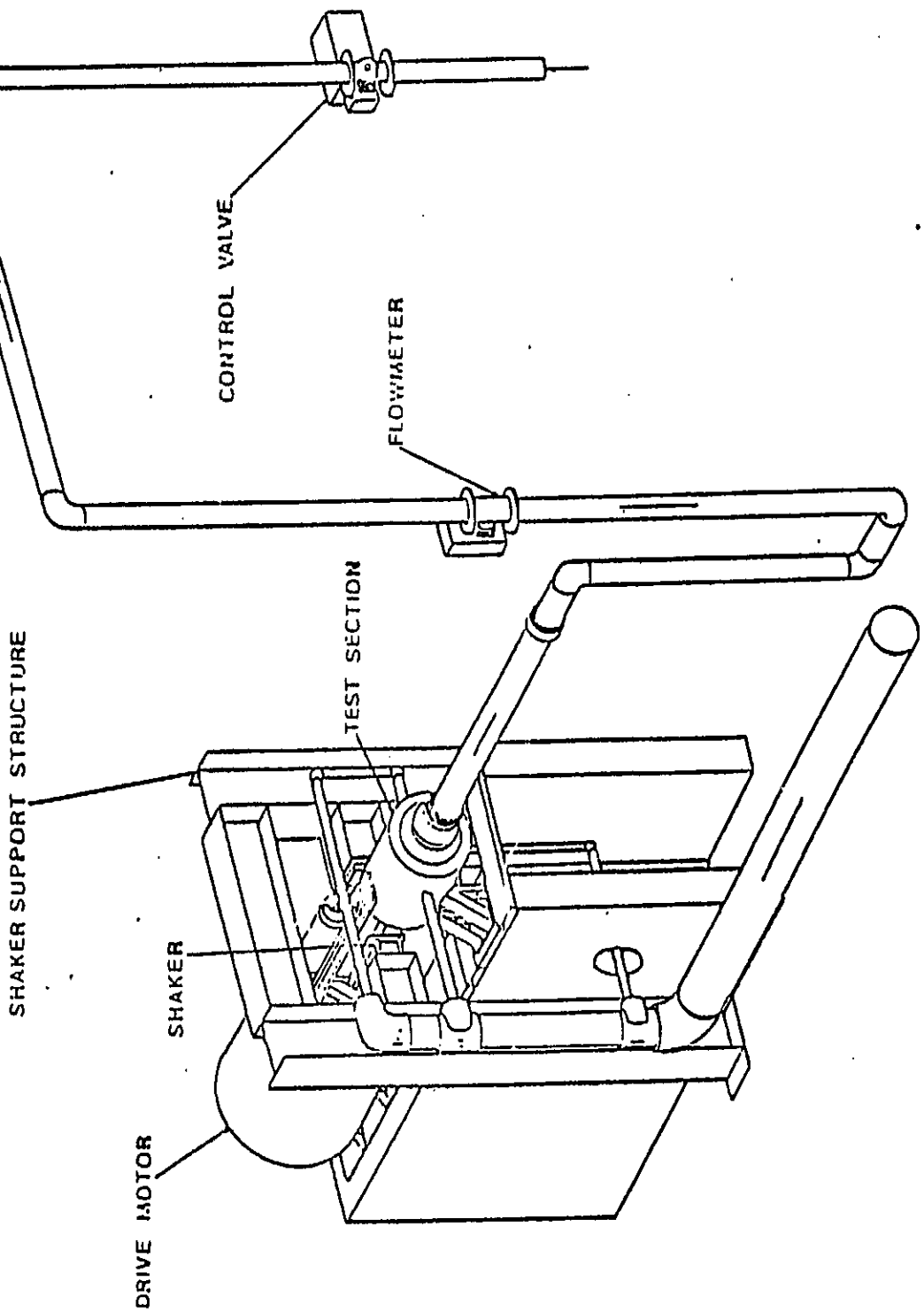

Fig. 17 Test apparatus assembly.

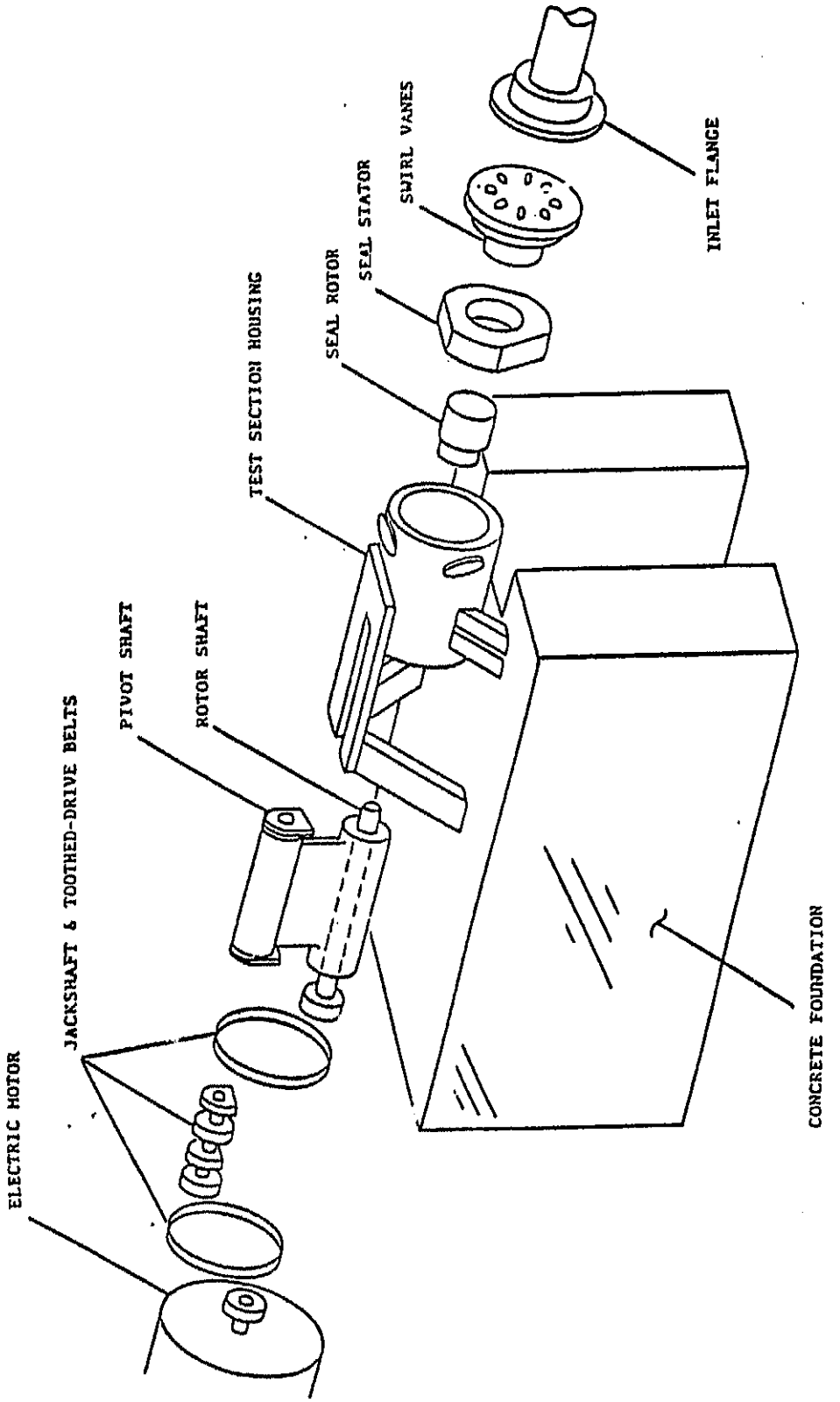

Fig. 18 Exploded view of test apparatus.

INSTRUMENTATION

Having discussed what seal parameters can be varied, and how the variations are implemented, the measurement of their respective effects can now be described. The types of measurements which are made can be grouped into three categories:

1) rotor motion,

2) reaction-force measurements, and

3) fluid flow measurements.

These categories are described individually in the sections that follow.

Rotor Motion Measurements. The position of the seal rotor within the stator is monitored by two Bently-Nevada eddy-current proximity probes, mounted in the test section housing. These probes are located 90 degrees apart, and correspond to the X- and Y-directions. The proximity probes are used to determine the static position and dynamic motion of the rotor, and their resolution is 0.0025 mm (0.1 mil).

Reaction-Force Measurements. Reaction forces arise due to the static position and dynamic motion of the seal rotor within the stator. The reaction forces (F_X, F_Y) exerted on the stator are measured by the three Kistler quartz load cells, which support the stator in the test section housing. When the rotor is shaken, vibration is transmitted to the test section housing, both through the thrust bearing and through the housing mounts. The acceleration of the housing and stator generates unwanted inertial "ma" forces which are sensed by the load cells, in addition to those pressure forces developed by the relative motion of the seal rotor and stator. For this reason, PCB

piezoelectric accelerometers with integral amplifiers are mounted in the X- and Y-directions on the stator, as shown in Figs. 12-14 and 16. These accels allow a (stator mass) x (stator acceleration) subtraction from the forces (F_X, F_Y) indicated by the load cells. With this correction, which is described more fully in the next section, only the pressure forces due to relative seal motion are measured.

Force measurement resolution is a function of the stator mass and the resolution of the load cells and accelerometers. Accelerometer resolution is 0.005 g, which must be multiplied by the stator mass in order to obtain an equivalent force resolution. The masses of the stators used in the test program reported here are presented in Table 2 along with the associated accelerometer resolution. Resolution of the load cells is 0.089 N (0.02 lb). A comparison with the entries in Table 2 reveals that the resolution of the force measurement is limited by the accelerometers. A stator with less mass, and/or accelerometers with greater sensitivity would improve force resolution.

Fluid Flow Measurements. Fluid flow measurements include the leakage (mass flow rate) of air through the seal, the pressure gradient along the seal axis, the inlet fluid circumferential velocity, and the entrance pressure loss.

Leakage through the constant 16 mil clearance smooth seal reported on here is measured with a Flow Measurement Systems Inc. turbine flowmeter located in the piping upstream of the test section. Resolution of the flowmeter is 0.0005 acf, and pressures and temperatures up and downstream of the meter are measured for mass flow rate determination. For the other seals in this report, the turbine

Table 2. Force measurement resolution.

Stator	Stator Mass		Accel. Force Resolution	
Force units	N	(lb)	N	(lb)
Smooth #1, no taper	11.4	(25.2)	0.560	(0.126)
Smooth #2, no taper	11.5	(25.3)	0.565	(0.127)
Tapered smooth	11.4	(25.1)	0.560	(0.126)
Honeycomb	3.94	(8.69)	0.191	(0.043)

flowmeter is replaced with a Fischer & Porter vortex flowmeter. Resolution of the turbine flowmeter is 0.0014 m^3 (0.05 acf).

For measurement of the axial pressure gradient, the stator has pressure taps drilled along the length of the seal in the axial direction. These pressures, as well as all others, are measured with a 0-1.034 MPa (0-150 psig) Scanivalve differential-type pressure transducer through a 48 port, remotely-controlled Scanivalve model J scanner. Transducer resolution is 0.552 kPa (0.08 psi).

In order to determine the circumferential velocity of the air as it enters the seal, the static pressure at the guide-vane exit is measured. This pressure, in conjunction with the measured flowrate and inlet air temperature, is used to calculate a guide vane exit Mach number. A compressible flow continuity equation

$$\dot{m} = p_{ex} A_{ex} M_{ex} [(\gamma/R_g T_t) (1 + (\gamma-1)M_{ex}^2 / 2)]^{1/2} \qquad (18)$$

is rearranged to provide a quadratic equation for M_{ex}

$$M_{ex}^2 = \{-1 + [1 + 2((\gamma-1)/\gamma) (\dot{m} / p_{ex}A_{ex})^2 (R_g T_t)]^{1/2} \} / (\gamma-1) \qquad (19)$$

where γ is the ratio of specific heats and R_g is the gas constant for air, p_{ex} is the static pressure at the vane exit, and A_{ex} is the total exit area of the guide vanes. Since all of the variables in the equation are either known or measured, the vane exit Mach number, and therefore the velocity, can be found.

In order to determine the circumferential component of this inlet velocity, a flow turning angle correction, in accordance with Cohen [20], is employed. The correction has been developed from guide-vane cascade tests, and accounts for the fact that the fluid generally is

not turned through the full angle provided by the shape of the guide-vanes. With this flow deviation angle calculation, the actual flow direction of the air leaving the vanes (and entering the seal) can be determined. Hence, the magnitude and direction of the inlet velocity is known, and the appropriate component is the measured inlet circumferential velocity.

The entrance-pressure-loss coefficient, defined in equation (6), is determined from the measured pressures just upstream of and just inside the seal. An entrance Mach number is calculated in the same manner as outlined previously, using the measured pressure immediately inside the seal and the annular area between the rotor and stator. This entrance Mach number, and the ratio of the seal entrance/guide vane exit pressures are substituted into equation (6), and the entrance loss coefficient, $\bar{k}$, is determined.

DATA ACQUISITION AND REDUCTION

With the preceding explanations of how the seal parameters are varied, and how these parameters are measured, the discussion of how the raw data is processed and implemented can begin. Data acquisition is directed from a Hewlett-Packard 9816 (16-bit) computer with disk drive and 9.8 megabyte hard disk. The computer controls an H-P 6940B multiprogrammer which has 12-bit A/D and D/A converter boards and transfers control commands to and test data from the instrumentation.

As was previously stated, the major data groups are seal motion/reaction force data and fluid flow data. The motion/reaction force data are used for dynamic coefficient identification. The hardware involved includes the load cells, accelerometers, X-direction motion probe, a Sensotec analog filter unit, a tunable bandpass filter, and the A/D converter. The operation of these components is illustrated in Fig. 19, and their outputs are used in a serial sampling scheme which provides the computer with the desired data for reduction. Recalling the discussion of the reaction force measurements in the preceding section, a (stator mass) x (stator acceleration) subtraction from the indicated load cell forces is necessitated due to vibration of the stator and test-section housing. This subtraction is performed with an analog circuit, and results in corrected F_X and F_Y force components due to relative seal motion.

The forced oscillatory shaking motion of the seal rotor is the key to the operation of the serial synchronous sampling (SSS) routine which is employed. The frequency of the rotor oscillation is set by a function generator, and rotor motion is sensed by the X-direction

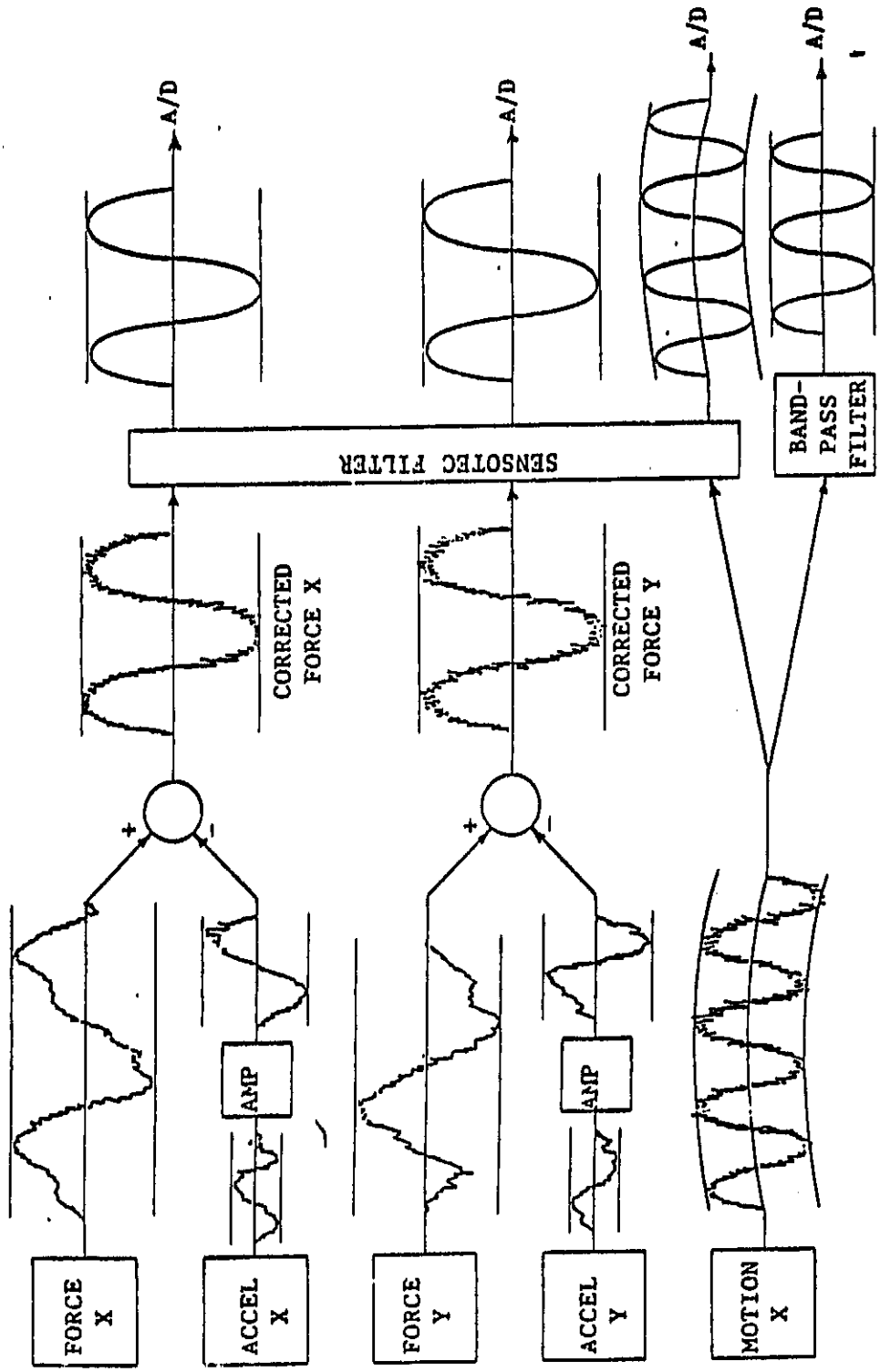

Fig. 19 Signal conditioning schematic for data acquisition.

motion probe. The motion signal is filtered by the narrow bandpass filter, and is used as a trigger signal for the SSS routine. Upon the operator's command, the SSS routine is enabled, and the next positive-to- negative crossing of the filtered motion signal triggers a quartz crystal clock/timer. Ten cycles of the corrected $F_X(t)$ signal are sampled, at a rate of 100 samples/cycle. The second positive-to-negative crossing of the filtered motion signal triggers the timer and initiates the sampling of ten cycles of the $F_Y(t)$ signal. Finally, the third positive-to-negative crossing triggers the timer again, and ten cycles of the corrected $X(t)$ signal are sampled. Thus, at every test condition, 1000 data points are obtained for $F_X(t_i)$,$F_Y(t_i)$, and $X(t_i)$, and the data arrays are stored in computer memory.

Some important points need to be stressed concerning this force/motion-data acquisition. First, the bandpass filter is used only to provide a steady signal to trigger the timer/clock. Any modulation of the motion signal due to rotor runout is eliminated by this filter, as long as the rotational frequency and shaking frequency do not coincide. Therefore, the shaking frequencies are selected to avoid coincidence with running speeds. However, the rotor motion and corrected force signals which are sampled and captured for coefficient identification are filtered only by a low-pass filter (500 Hz cutoff), and the effects of runout as well as shaking motion are present in the recorded data. A second point worth noting is that the sample rate is directly dependent on the shaking frequency. As the shaking frequency is increased, the sample rate (samples/second) also increases. In order to get the desired 100 samples/cycle, shaking frequencies must

be chosen to correspond to discrete sample rates which are available. Hence, the frequency at which the rotor is shaken is carefully chosen to provide the desired sampling rate and a steady trigger signal.

Most of the fluid flow data are used for the input parameters required by Nelson's analysis. The upstream (reservoir) pressure and temperature, downstream (sump) pressure, and the inlet circumferential velocity (determined as outlined earlier) are provided directly. The friction-factor values of the rotor and stator are supplied in the form of Hirs' coefficients, which are obtained from the pressure distribution data in the manner described below.

Recalling the discussion of Hirs' turbulent bulk-flow fluid model, the model assumes that the wall shear stresses can be written as in equation (4). For the gas seals discussed here, an adiabatic, compressible flow with friction analysis is employed, and the measured pressure gradient and mass flow rate (leakage) data are used to calculate a friction factor coefficient, λ, for each test condition. From the λ versus R_a and ω data, the Hirs coefficients mr, nr of the friction factor formula

$$\lambda = nr\ R_a^{mr}\ [\ 1 + 1\ /\ 4b^2]^{(1+mr)/2}\ ,\quad b = U\ /\ R\omega \tag{20}$$

are calculated on a least-square basis. For the constant clearance smooth-rotor/smooth-stator combinations, the values are assumed to apply for both the rotor and stator. Hence, for this case, mr=ms and nr=ns.

For the smooth-rotor/honeycomb-stator combination, a combined λ is measured, which is related to the rotor λ_r and (honeycomb) stator λ_s by

$$\lambda_c = (\lambda_r + \lambda_s)\ /\ 2 \tag{21}$$

hence,

$$\lambda_s = 2\lambda_c - \lambda_r \ . \qquad (22)$$

Therefore, λ_s is determined from measured data for λ_c and a value for λ_r as determined from equation (20) with experimental values for mr and nr. Then, as before, the λ_s versus R_a and ω data are used to calculate Hirs' coefficients for the honeycomb stator.

For the convergent tapered smooth seal, the pressure drop within the seal is affected by the change in cross-sectional area of the seal annulus as well as by friction. The pressure gradient and mass flow rate data are used to calculate a coefficient, λ_{eff}, which includes both effects. For a seal of inlet and outlet radial clearance C_i and C_o, respectively, Childs [21] has derived an expression for λ_{eff}. In this case, λ_{eff} is related to the desired friction factor, λ, by

$$\lambda_{eff} = [\ (2q\bar{C}/L) + \lambda\ ] \ / \ (1-q^2)^2 \qquad (23)$$

in which

$$q = (C_i - C_o) \ / \ (C_o + C_i)$$

and

$$\bar{C} = (C_o + C_i)/2.$$

Solving (23) for λ,

$$\lambda = \lambda_{eff}\ (1-q^2)^2 - 2q\bar{C}/L. \qquad (24)$$

Using this combined λ, Hirs' coefficients for the tapered stator are calculated using equation (22) in the same way as were those for the honeycomb stator.

As stated previously, Hirs' coefficients for the seal rotor and stator are required input parameters for Nelson's analysis, as are the fluid flow conditions up and downstream of the seal and the rotational

speed of the rotor. The appropriate input parameters for each specific test case can be provided for Nelson's analysis from static test results and measurement. In this manner, a point-by-point comparison of theoretical predictions to experimental results can be made for leakage through the seal, axial-pressure distribution, entrance-loss coefficient, and rotordynamic coefficients.

TEST PROCEDURES

At the start of each day's testing, the force, pressure, and flowmeter systems are calibrated. The total system, from transducer to computer, is calibrated for each of these variables. The force system calibration utilizes a system of pulleys and known weights applied in the X- and Y-directions. An air-operated dead-weight pressure tester is used for pressure-system calibration, and flowmeter system calibration is achieved with an internal precision quartz clock which simulates a known flowrate.

All of the tests performed to date have been made with the rotor executing small motion about a centered position. A typical test begins by centering the seal rotor in the stator with the Zonic hydraulic shaker, starting airflow through the seal, setting the rotational speed of the rotor, and then beginning the shaking motion of the rotor. Data points are taken at rotational speeds of 200, 500, and 1000-8000 cpm, in 1000 cpm increments. At each rotational speed, the inlet pressure is varied and data points are taken at one unchoked flow and four choked flow conditions. For each test case (i.e., one particular running speed, shaking frequency, inlet pressure, and prerotation condition), the measured leakage, rotordynamic coefficients, axial pressure distribution, and entrance loss coefficient are determined and recorded.

This test sequence is followed for each of three different shaking frequencies, and for three inlet swirl configurations (with rotor rotation, opposite rotation, and no swirl). Therefore, fifty data points are taken per test (i.e. one shaking frequency and inlet

swirl combination), with a total of nine tests for small motion about a centered position made per seal. With the constant 16 mil clearance smooth seal, tests were run at each of two shaking frequencies and five swirl configurations (two with rotor rotation, two opposite rotor rotation, and no swirl), for a total of ten tests. Furthermore, the 200 cpm data points were eliminated with this seal.

RESULTS

The test results reported here were developed as part of an extended, joint NASA-USAF funded program for annular gas seal studies. Tests were carried out on two smooth-rotor/smooth-stator constant-clearance seals, a smooth-rotor/smooth-stator convergent-tapered seal, and a smooth-rotor/honeycomb-stator seal. The dimensions and pertinent data for each are included in Table 3, in which the seals are referred to as C1, C2, T, and H, respectively. The honeycomb insert, provided by the Rocketdyne division of Rockwell International, is the turbine interstage seal of the HPOTP (High-Pressure Oxygen Turbopump) of the SSME (Space Shuttle Main Engine). Fig. 20 illustrates the honeycomb configuration.

The test program had the following objectives:

1) Acquire leakage, friction factor, and entrance-loss data for smooth and honeycomb seals.

2) Compare predictions from current theory to test results.

3) Compare the stability performances of the seals tested.

4) Compare the effect on leakage and rotordynamic coefficients of varying the clearance geometry of a smooth-rotor/smooth-stator seal.

The Hirs coefficients for all seals were determined in the manner described previously. The values of these coefficients are listed in Table 4.

The results provided here are grouped in static (entrance loss coefficient, leakage, pressure distribution) and dynamic (rotordynamic coefficient) sections. Experimental results are

Table 3. Test seal specifications.

Rotors		
Seal:	C1, C2, T	H
Diameter:	15.136 cm (5.959 in)	14.453 cm (5.690 in)
Material:	304 stainless steel	304 stainless steel
Surface roughness:	0.102 μm (4 μin)	0.127 μm (5 μin)
Stators		
Seal:	C1	C2
Diameter:	15.283 cm (6.017 in)	15.215 cm (5.99 in)
Material:	304 stainless steel	304 stainless steel
Surface roughness:	0.140 μm (5.5 μin)	0.700 μm (28 μin)
Seal:	T	H
Diameter:	-	14.614 cm (5.754 in)
upstream	15.364 cm (6.049 in)	-
downstream	15.283 cm (6.017 in)	-
Material:	304 stainless steel	6061-T6 Aluminum
Surface roughness:	0.889 μm (35 μin)	1.575 mm (0.062 in) Comb

Seal	Radial clearance	Seal Length
C1	0.7366 mm (29.0 mil)	5.080 cm (2.00 in)
C2	0.3937 mm (15.5 mil)	5.080 cm (2.00 in)
T	C_i = 1.1430 mm (45.0 mil) C_o = 0.7366 mm (29.0 mil) q = 0.216	5.080 cm (2.00 in)
H	0.8065 mm (31.8 mil)	2.540 cm (1.00 in)

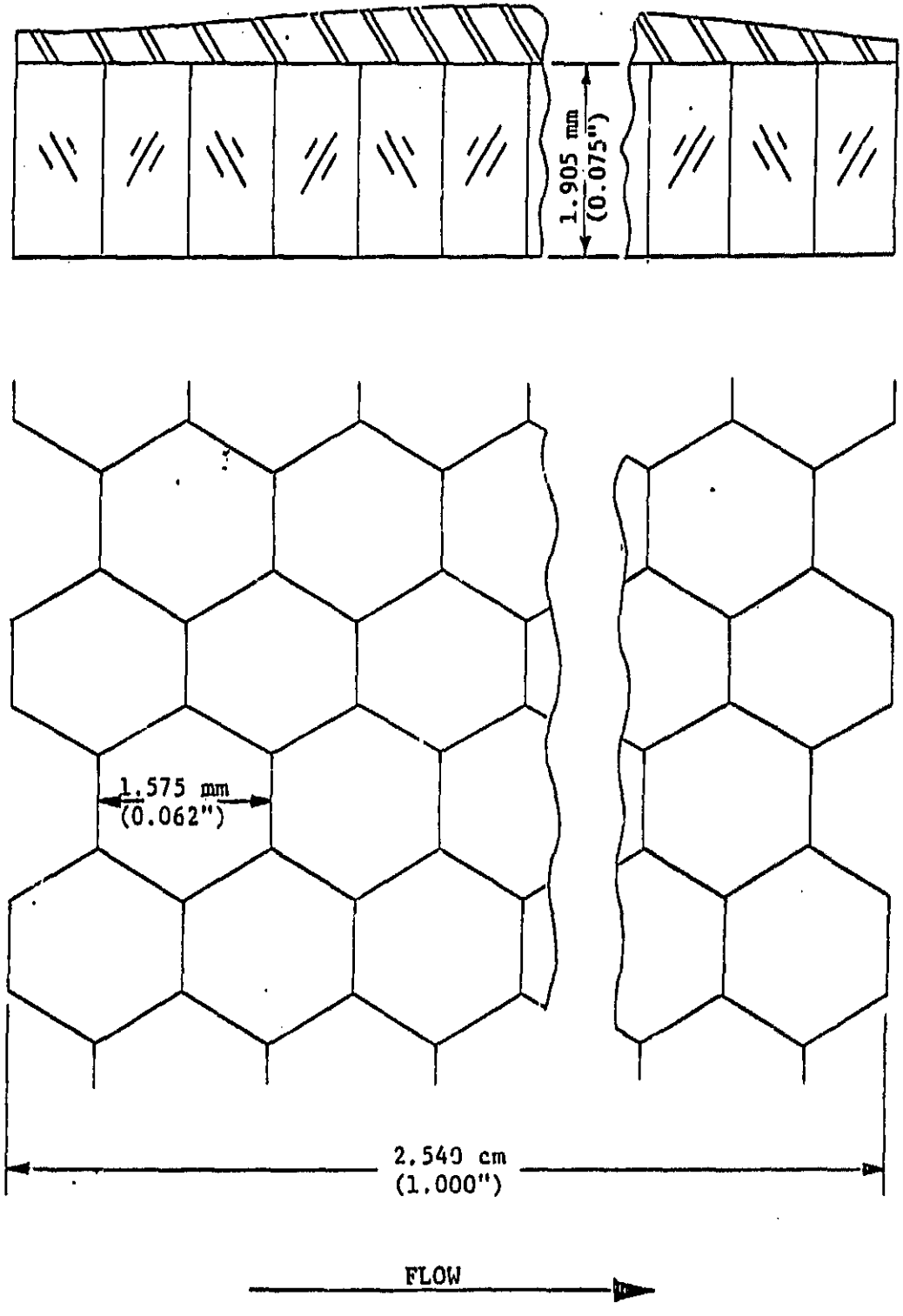

Fig. 20 Honeycomb stator insert detail.

Table 4. Friction factor data.

C1: constant 29 mil clearance smooth seal.
C2: constant 16 mil clearance smooth seal.
T: convergent tapered seal.
H: smooth-rotor/honeycomb-stator seal.

Hirs' coefficients	C1	C2	T	H
Rotor ns:	0.187	0.0419	0.187	0.187
Rotor ms:	-0.333	-0.170	-0.333	-0.333
Stator ns:	0.187	0.0419	0.349	0.187
Stator ms:	-0.333	-0.170	-0.326	-0.0778

compared to the predictions of Nelson's analysis for each seal. One-to-one comparisons of the constant 29 mil clearance smooth seal (C1) to the constant 16 mil clearance (C2) and to the tapered (T) seal are included. The only significant difference between C1 and C2 is the size of the clearance. Seal T differs from C1 only in its taper (Table 3). Since the pressure ratios applied during the testing of two different seals were not exactly the same, seal coefficient and leakage values for pressure ratios other than those for which data is available were interpolated. A one-to-one comparison of the honeycomb seal (H) and any other seal configuration is precluded due to differences in seal length, nominal clearance, and inlet guide-vane configuration, as indicated in Figs. 11 and 15.

Some plots of leakage and rotordynamic coefficients include both experimental and theoretical data. In these cases, solid lines indicate the theoretical data. The location of the symbols for the experimental data represents the average value (averaged over all running speeds) at a particular inlet pressure, and the vertical lines through the symbols indicate the measured variance over the speed range. Table 5 provides a definition of the symbols used in the figures. Tables 6 and 7 provide definitions of symbols used in other figures.

Static Results. Figs. 21-34 are plots of $(\overline{k}+1)$ versus axial Reynolds number for the seals in this study. The curves plotted in each figure correspond to test running speeds. In Nelson's analysis, the seal entrance loss $\overline{k}$ in equation (6) is modeled by equation (7), repeated here:

$$\overline{k} + 1 = a + b(R_a)^c \qquad (7)$$

Table 5. Definition of symbols
figures 35-38, 61-66, 68-77

Swirl configuration	Nelson's Prediction	Experimental Results
With rotor rotation high velocity swirl	W	▲
With rotor rotation low velocity swirl	w	△
No prerotation of inlet air	N	□
Against rotor rotation low velocity swirl	α	▽
Against rotor rotation high velocity swirl	A	▼

Table 6. Definition of symbols
figures 39-40, 78-85

Swirl configuration	Seal C1	Seals C2, T	Ratios C2/C1, T/C1
Low velocity swirl with rotor rotation	△	▲	△
No prerotation of inlet air	□	■	□
Low velocity swirl against rotor rotation	▽	▼	▽

Table 7. Definition of symbols figures 42-55, 67

Line no.	Inlet pressure kPa	(psig)
1	186.9	(12.4)
2	308.2	(30)
3	446.1	(50)
4	584.0	(70)
5	721.9	(90)
6	825.3	(105)

Theoretical results : broken lines

Experimental data : solid lines

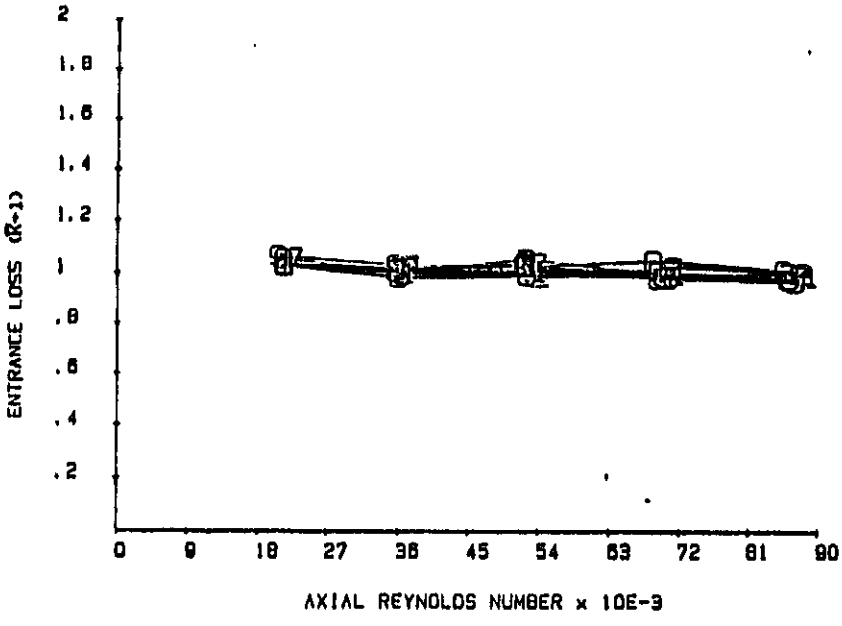

Fig. 21. Entrance loss for constant 29 mil clearance smooth seal, low speed prerotation in the direction of rotor rotation.

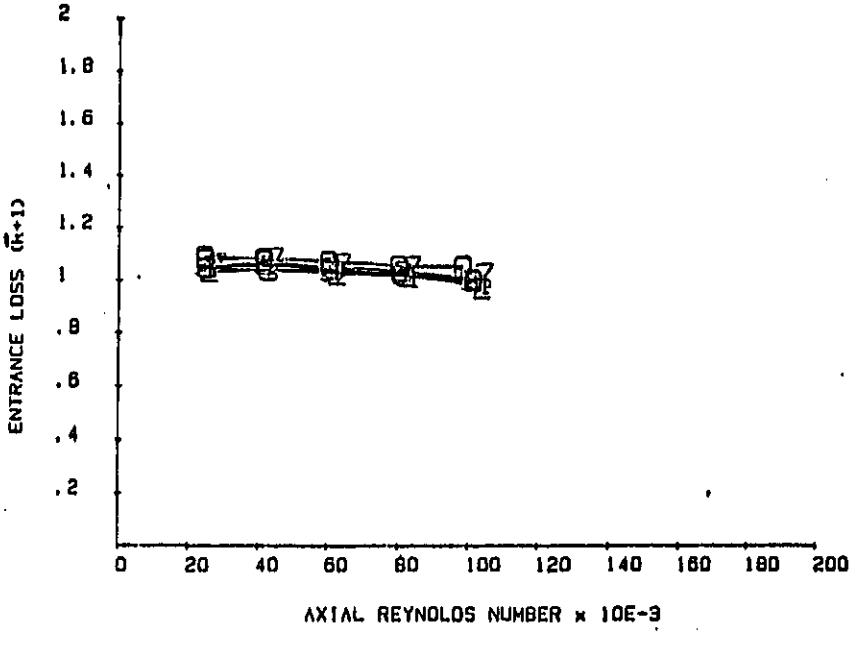

Fig. 22. Entrance loss for constant 29 mil clearance smooth seal, no prerotation of inlet air.

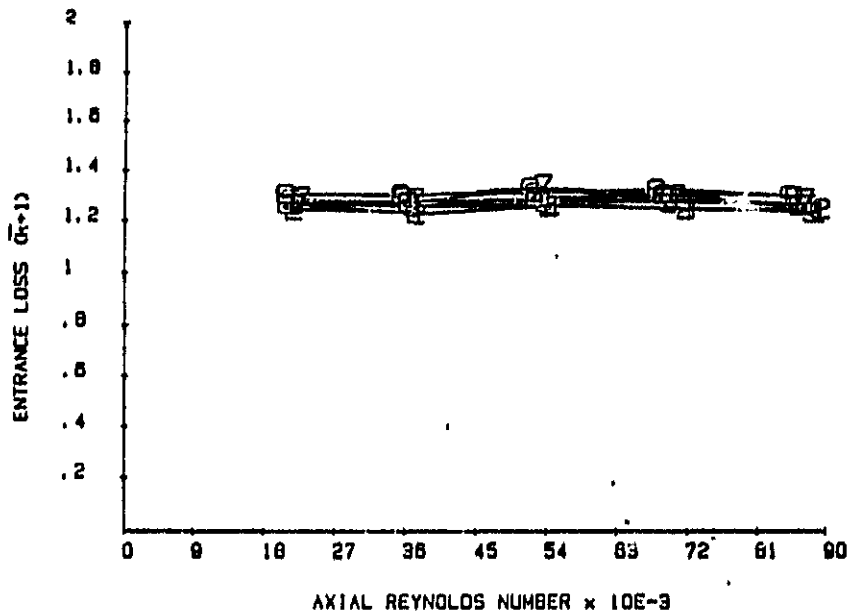

Fig. 23. Entrance loss for constant 29 mil clearance smooth seal, low speed prerotation opposing rotor rotation.

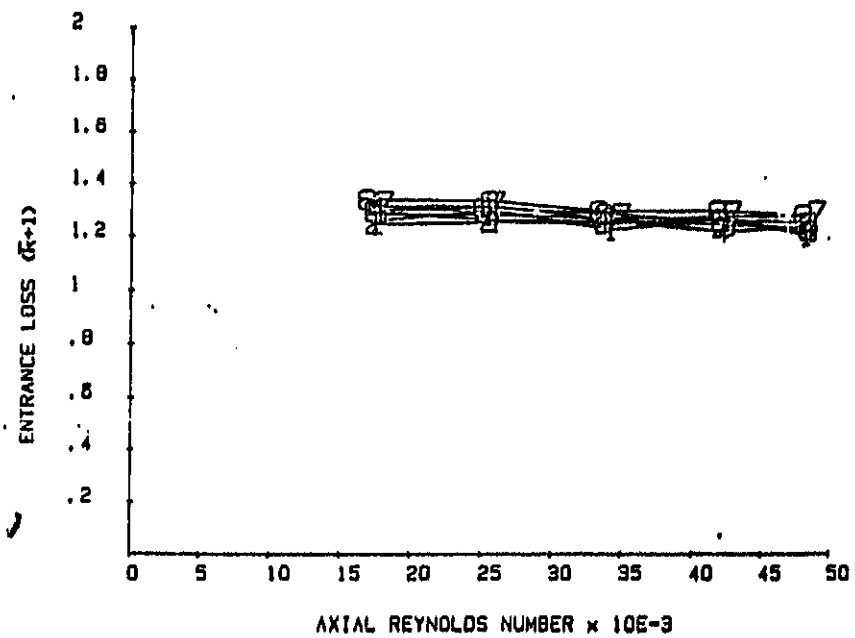

Fig. 24. Entrance loss for constant 16 mil clearance smooth seal, high speed prerotation in direction of rotor rotation.

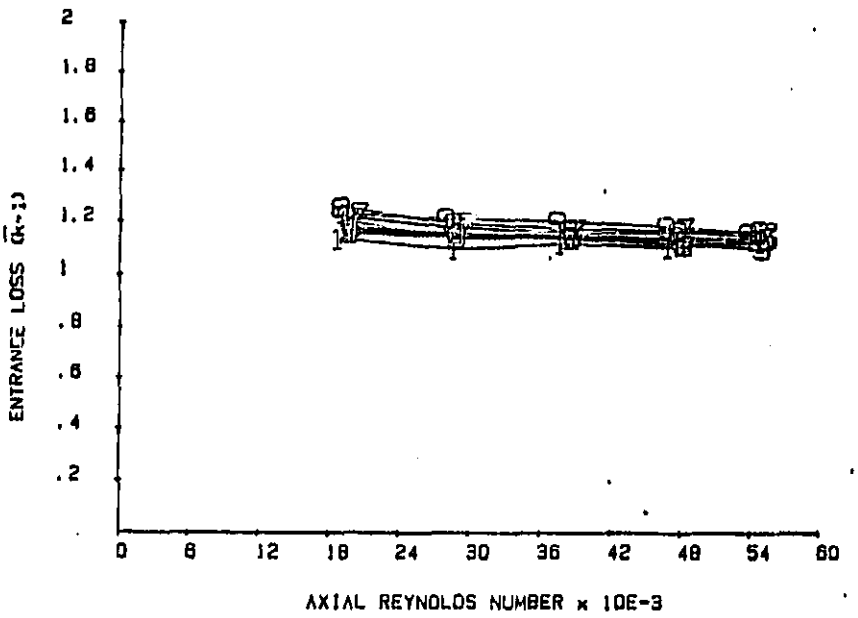

Fig. 25. Entrance loss for constant 16 mil clearance smooth seal, low speed prerotation in direction of rotor rotation.

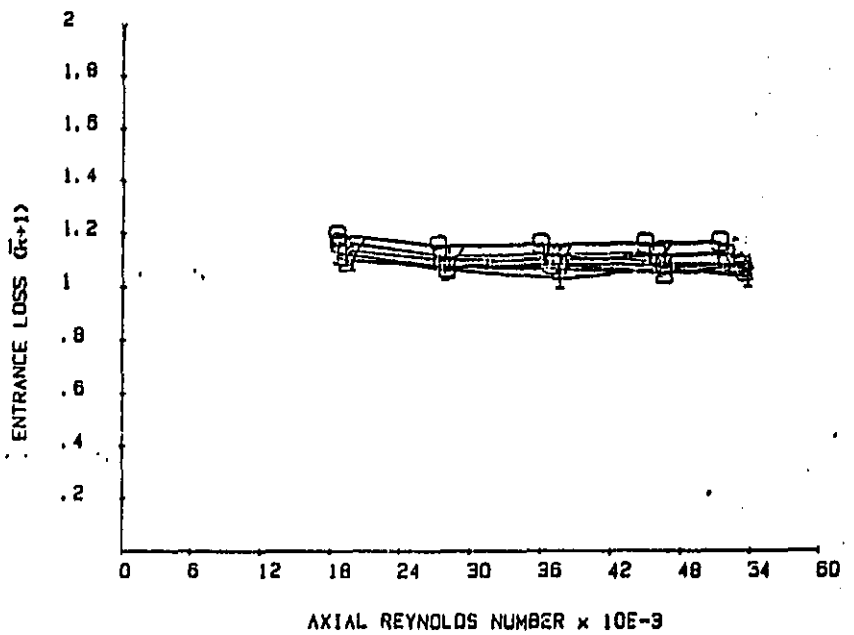

Fig. 26. Entrance loss for constant 16 mil clearance smooth seal, no prerotation of inlet air.

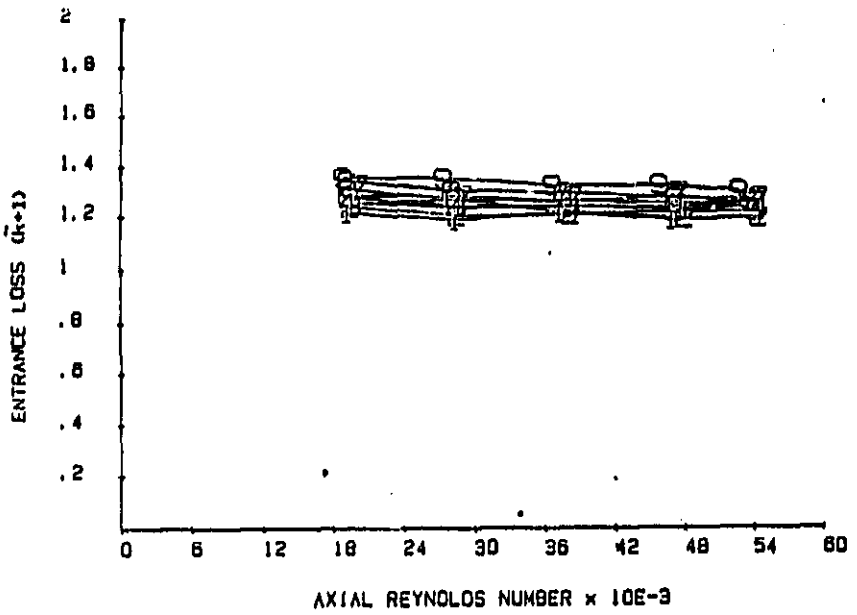

Fig. 27. Entrance loss for constant 16 mil clearance smooth seal, low speed prerotation opposing rotor rotation.

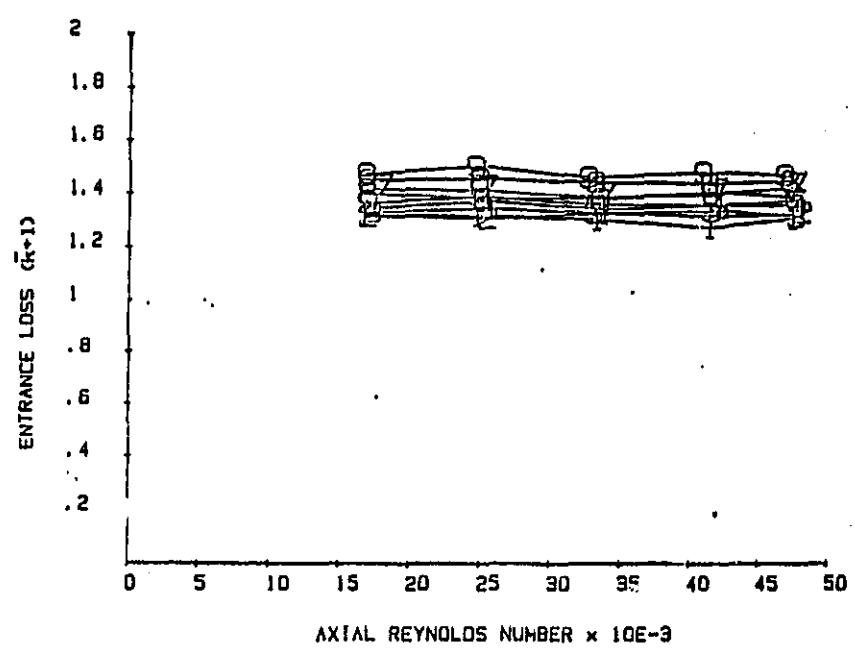

Fig. 28. Entrance loss for constant 16 mil clearance smooth seal, high speed prerotation opposing rotor rotation.

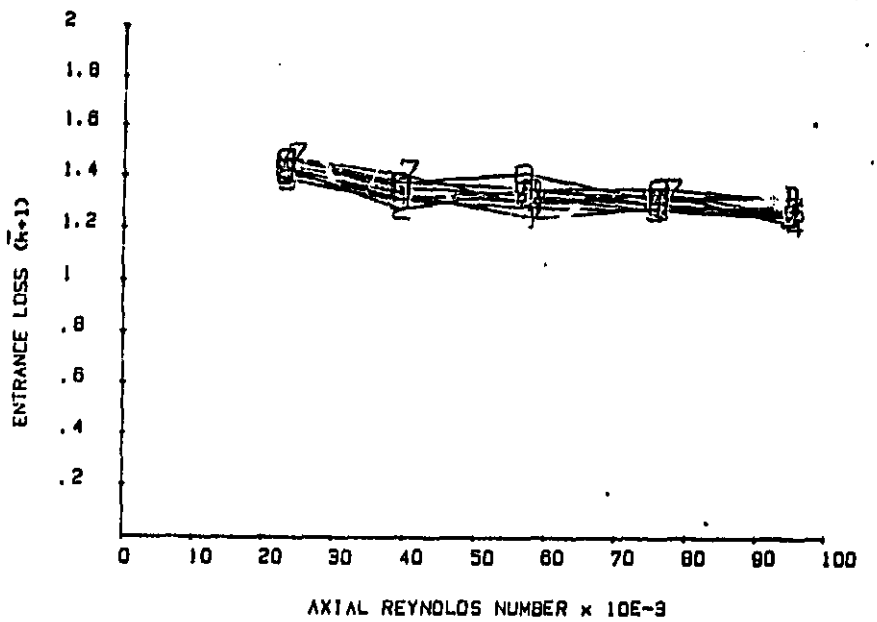

Fig. 29. Entrance loss for convergent tapered seal, low speed prerotation in direction of rotor rotation.

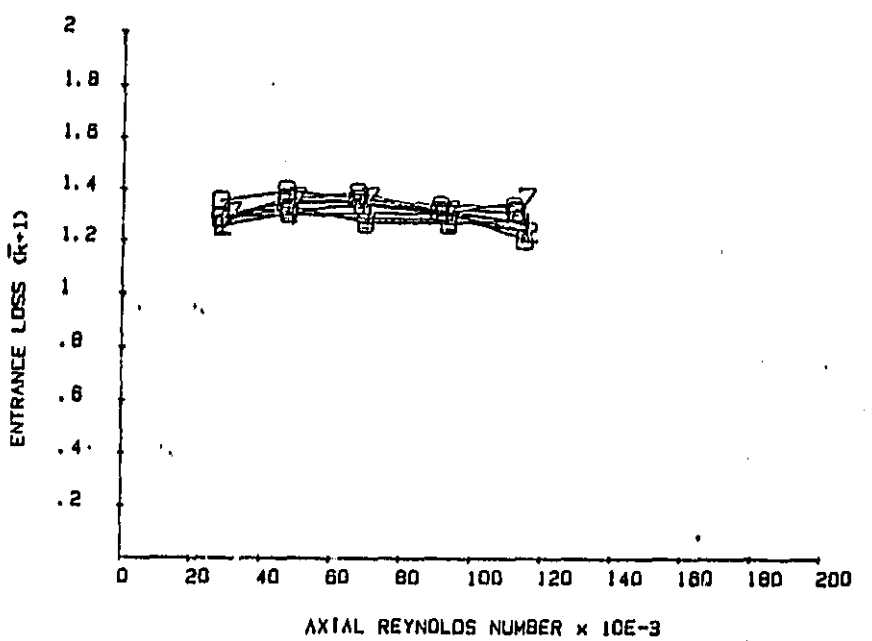

Fig. 30. Entrance loss for convergent tapered seal, no prerotation of inlet air.

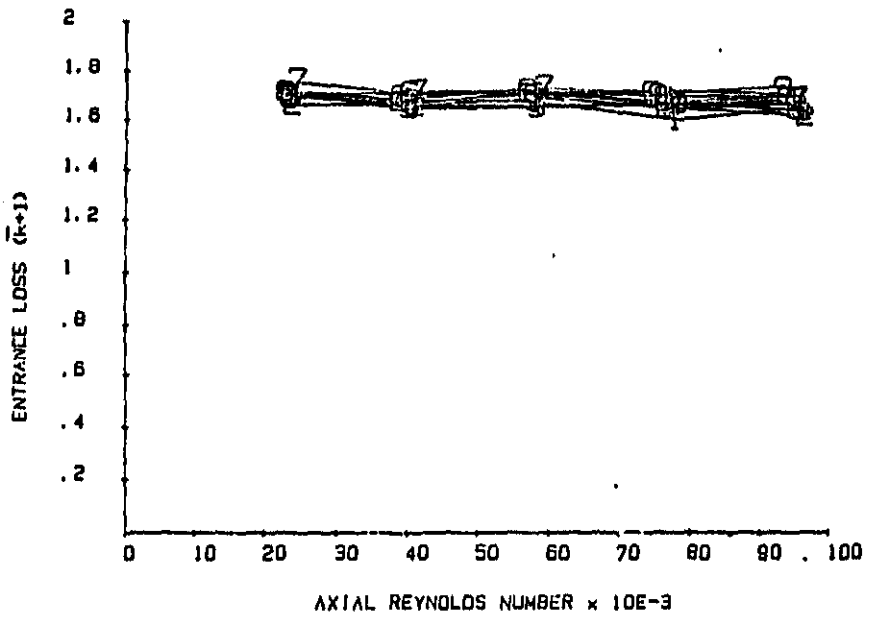

Fig. 31. Entrance loss for convergent tapered seal, low speed prerotation opposing rotor rotation.

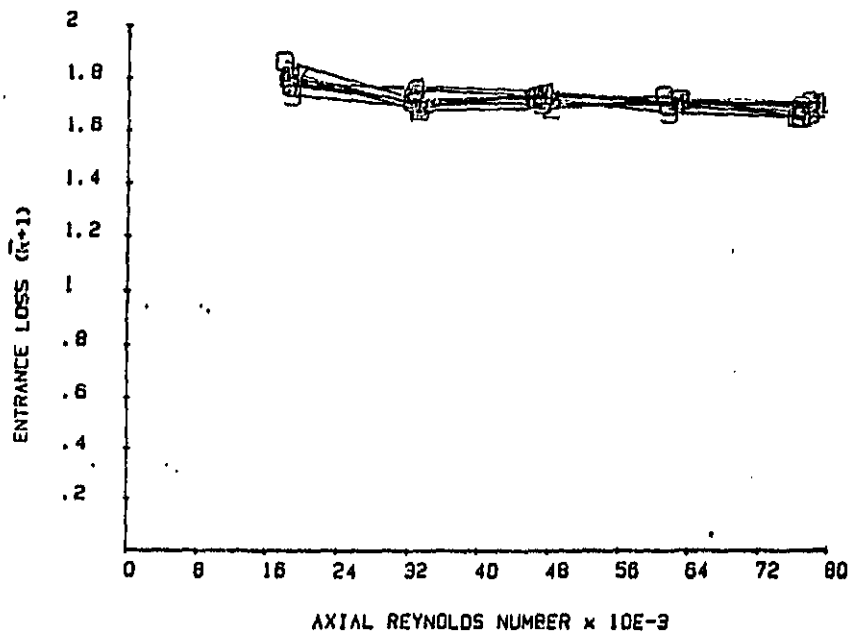

Fig. 32. Entrance loss for honeycomb seal, low speed prerotation in direction of rotor rotation.

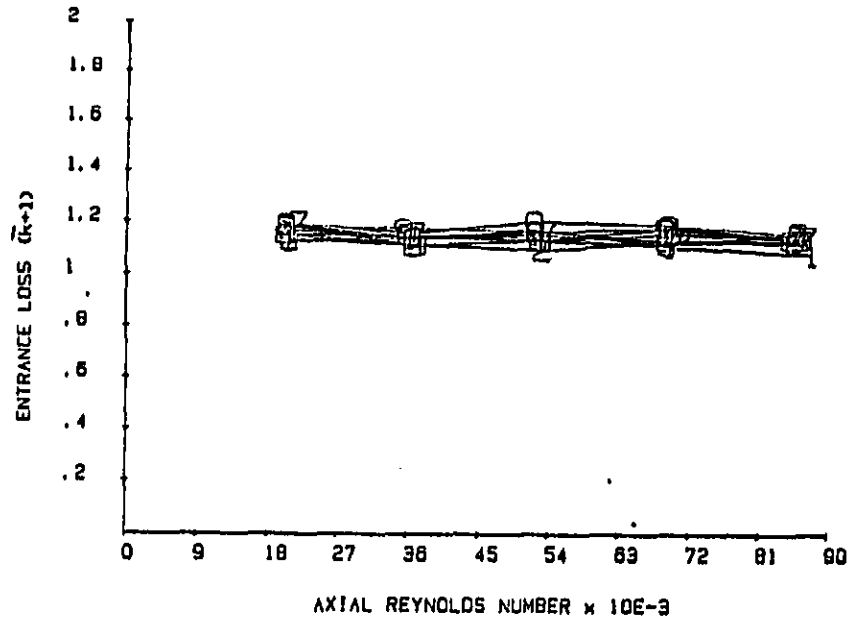

Fig. 33. Entrance loss for honeycomb seal, no prerotation of inlet air.

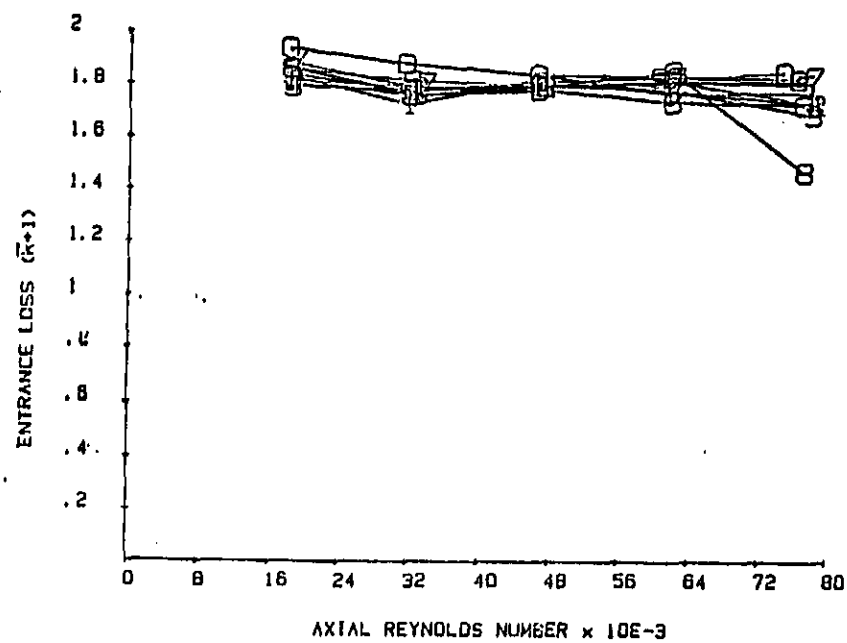

Fig. 34. Entrance loss for honeycomb seal, low speed prerotation opposing rotor rotation.

where R_a is the axial Reynolds number and a, b, and c are constants. For the data plotted here, good agreement was achieved setting

$$\bar{k} + 1 = b(R_a)^c$$

(i.e. setting a = 0) and using a least squares curve fit. The values of b and c thus determined for each swirl configuration for each seal are given in Table 8.

Comparisons of the theoretical and experimental leakage through the seals for various fluid prerotation conditions appear in Figs. 35-38. The symbols used are defined in Table 5. The figures show the leakage at various pressure ratios (reservoir pressure / sump pressure). A comparison shows that for all seals, leakage is underpredicted by less than 9% for all prerotation cases.

A comparison of the measured leakage of the two constant clearance smooth seals is presented in Fig. 39. The symbols are defined in Table 6. The 29 mil clearance seal leakage (C1) shows a greater dependence on preswirl configuration than does the 16 mil clearance seal leakage (C2). The ratio of the leakage of C2 to the leakage of C1 decreases with increasing pressure ratio. For low-speed preswirl with rotor rotation, the leakage ratio drops from 0.51 to 0.43 over a pressure ratio range of 2.8 to 5.5. For no swirl, the leakage ratio drops from 0.43 to 0.37, while for swirl against rotor rotation, the leakage ratio drops from 0.47 to 0.43.

Fig. 40 shows a comparison of the measured leakage of the constant 29 mil clearance seal and the convergent tapered seal (T). For a pressure ratio range of 1.7 to 5.5, the leakage of T exceeds that of C1 by 9% to 12% for all swirl configurations.

The pressure gradient plots are included in Figs. 41-55. Fig. 41

Table 8. Empirical coefficients of entrance loss.

Seal	Swirl	a	b	c
C1	w	0	1.46	-0.0350
	N	0	1.51	-0.0347
	α	0	1.33	-0.00435
C2	W	0	1.97	-0.0427
	w	0	2.01	-0.0530
	N	0	1.48	-0.0285
	α	0	1.79	-0.0335
	A	0	1.50	-0.00803
T	w	0	3.15	-0.0795
	N	0	1.43	-0.00847
	α	0	2.00	-0.0163
H	w	0	2.71	-0.0431
	N	0	1.35	-0.0157
	α	0	2.56	-0.0340

W = high speed swirl in the direction of rotor rotation.

w = low speed swirl in the direction of rotor rotation.

N = no prerotation of inlet air.

α = low speed swirl opposite the direction of rotor rotation.

A = high speed swirl opposite the direction of rotor rotation.

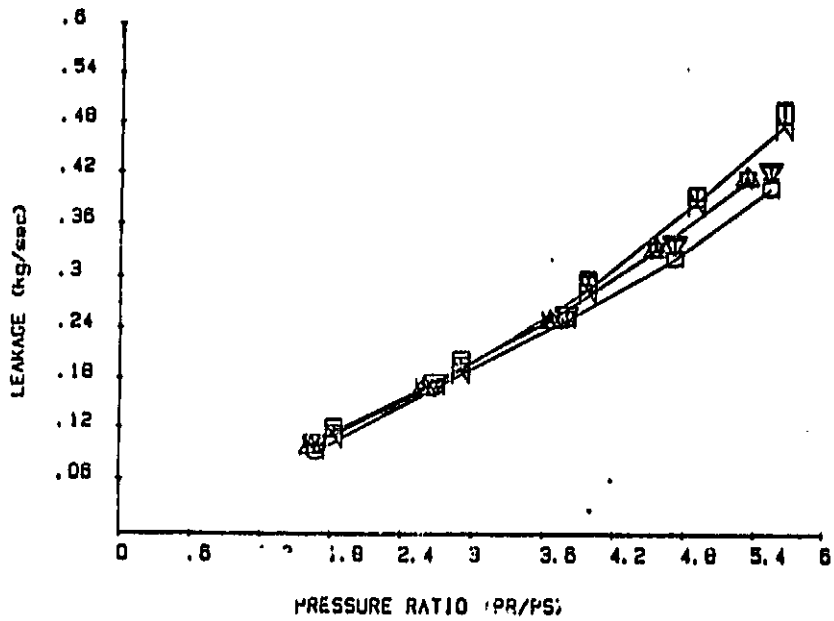

Fig. 35. Leakage of constant 29 mil clearance smooth seal, theoretical and experimental.

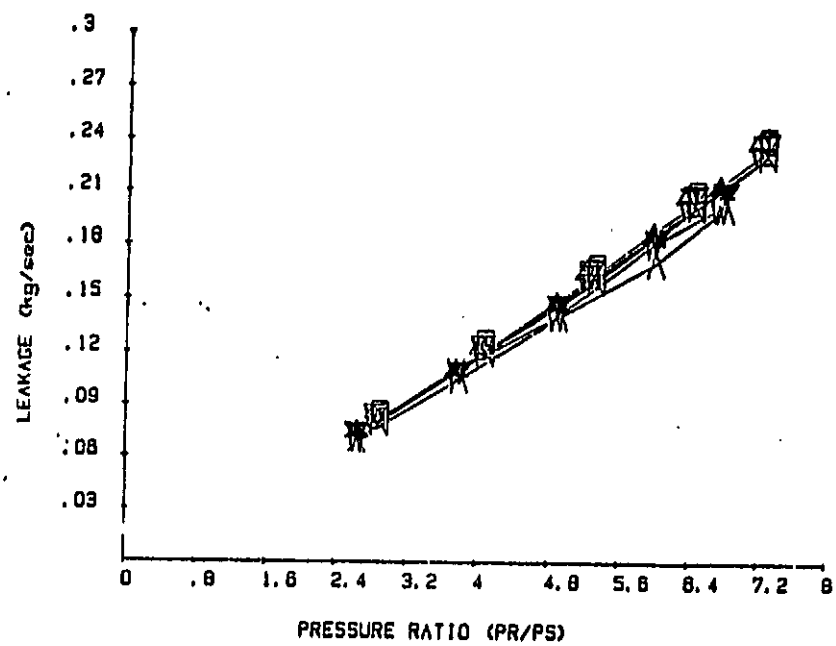

Fig. 36. Leakage of constant 16 mil clearance smooth seal, theoretical and experimental.

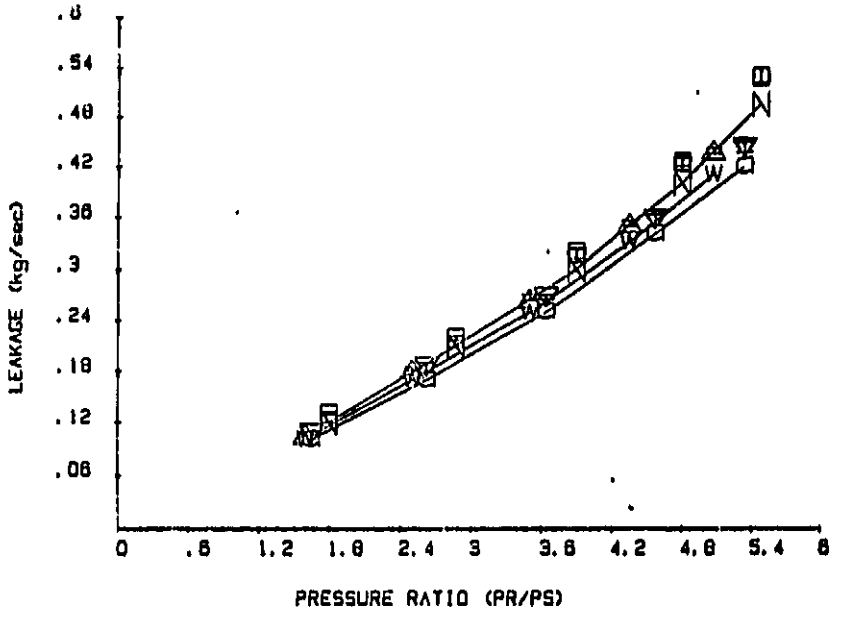

Fig. 37. Leakage of convergent tapered seal, theoretical and experimental.

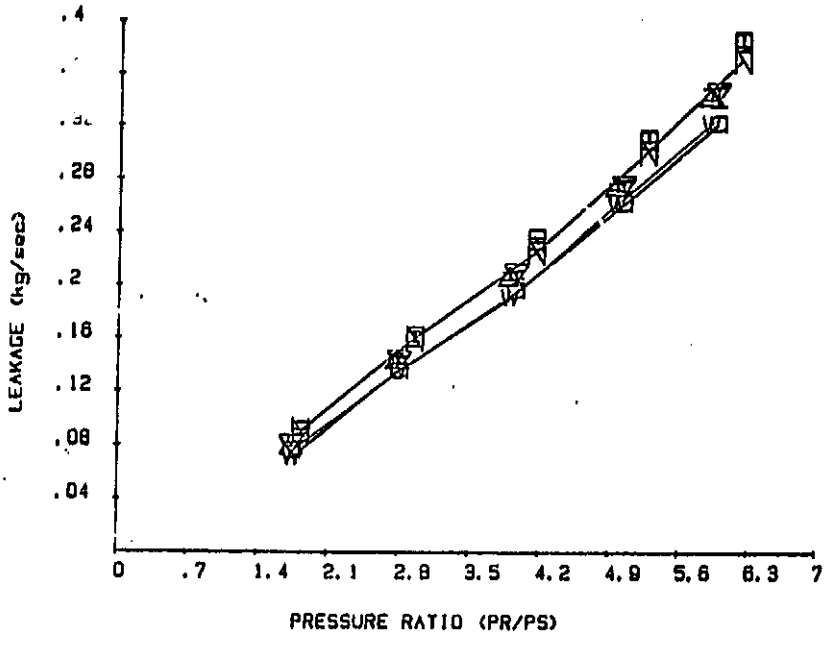

Fig. 38. Leakage of honeycomb seal, theoretical and experimental.

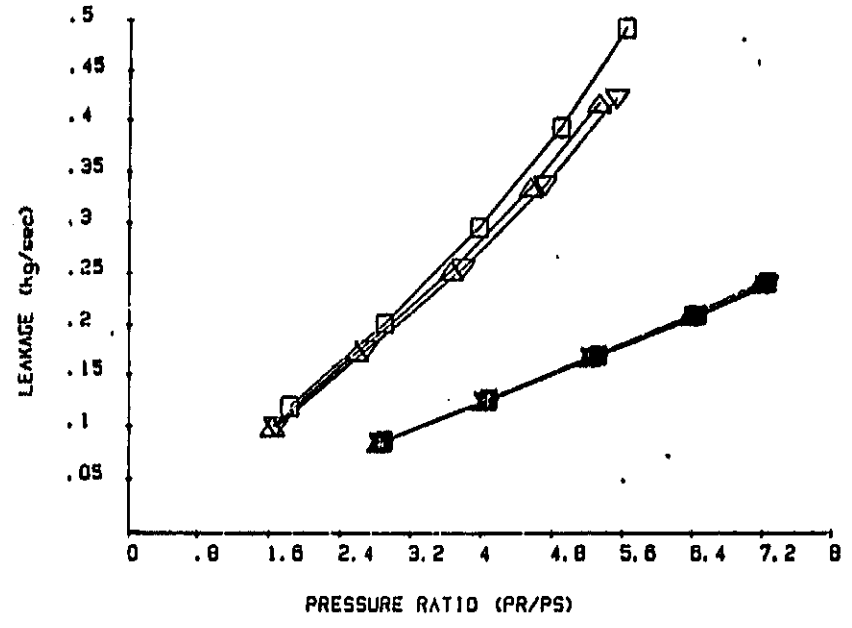

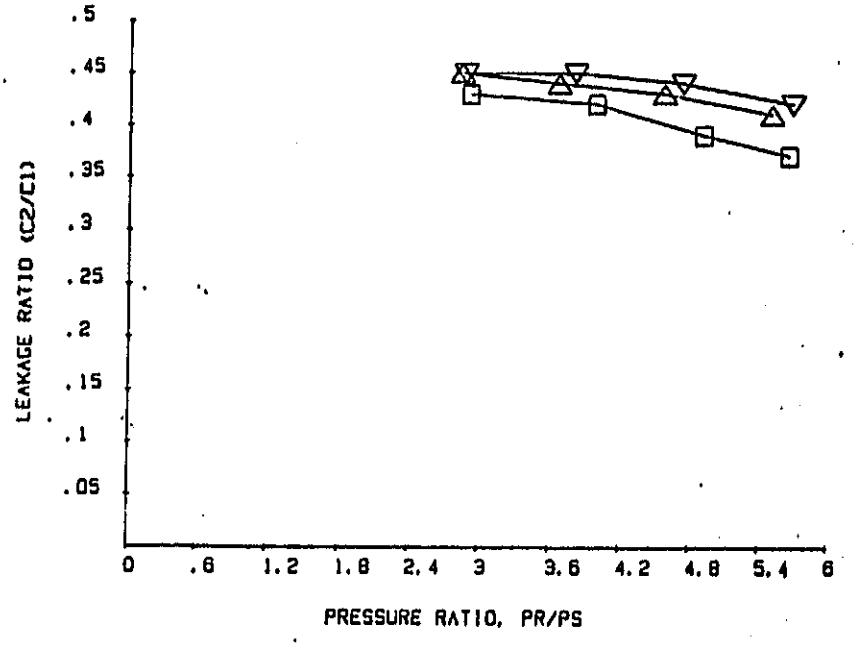

Fig. 39. Leakage comparison of constant clearance smooth seals: 29 mil clearance (C1) vs. 16 mil clearance (C2).

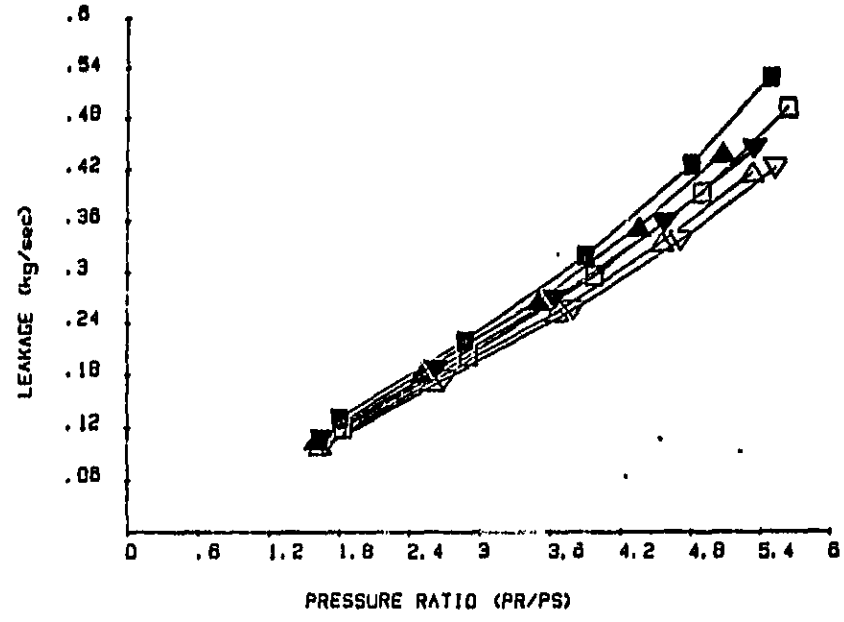

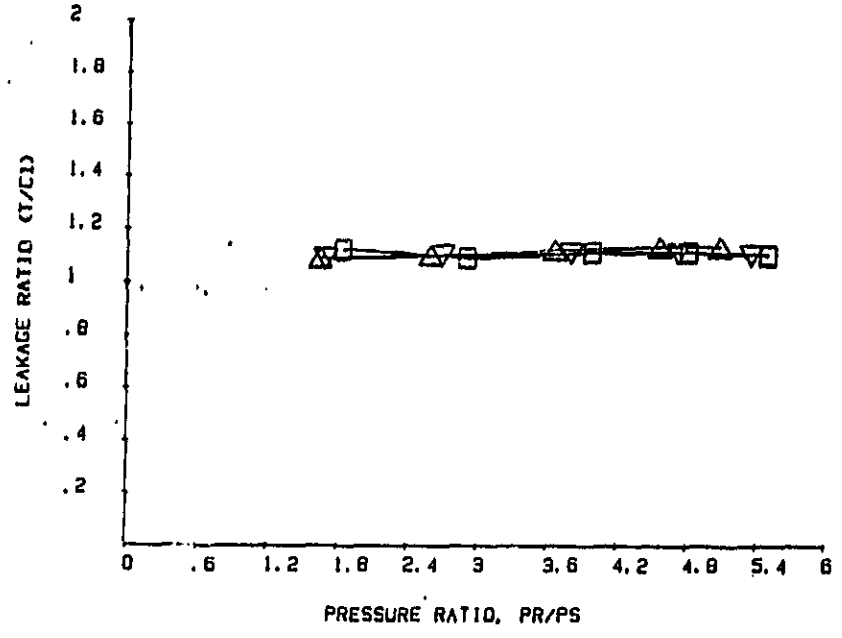

Fig. 40. Leakage comparison of constant 29 mil clearance smooth seal (C1) and convergent tapered seal (T).

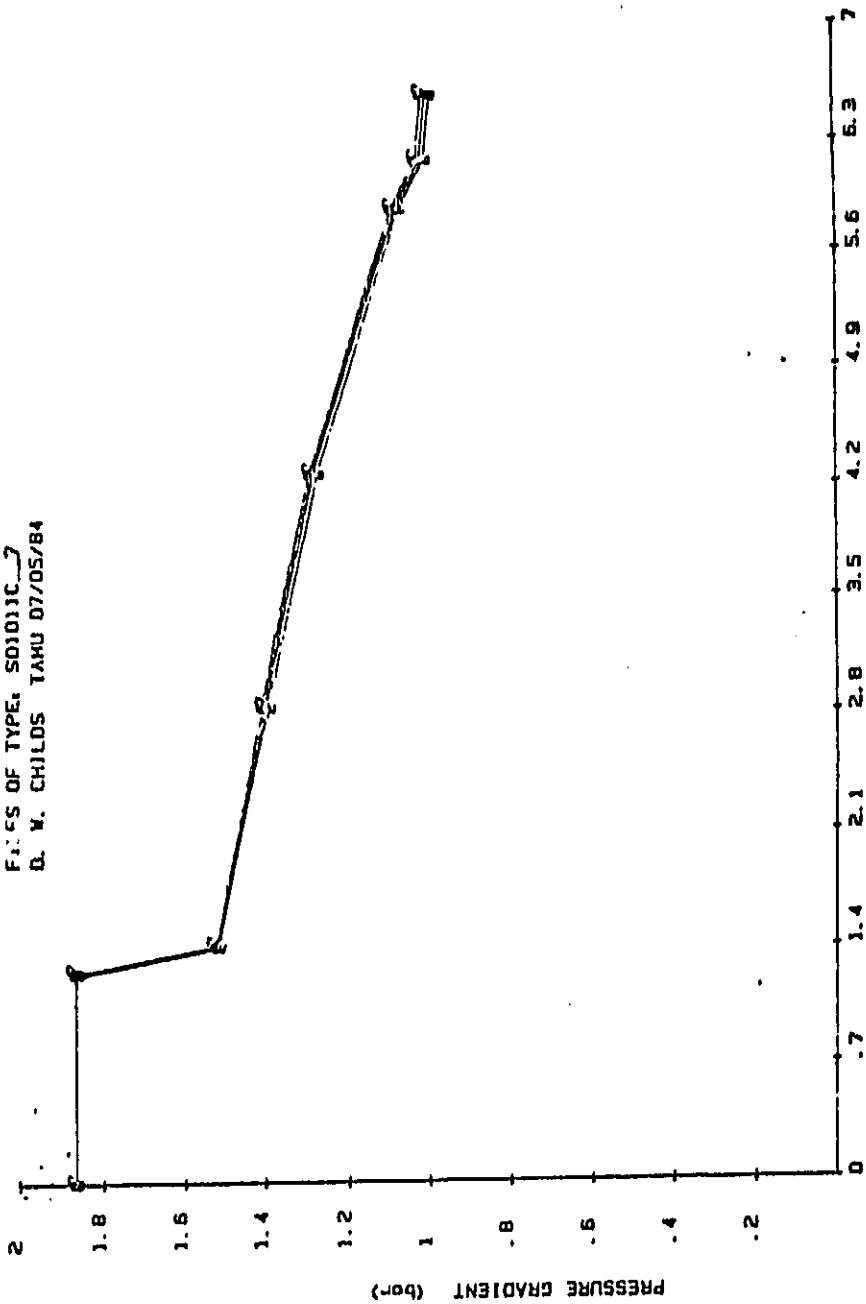

Fig. 41. Axial pressure gradient in constant 29 mil clearance smooth seal with no prerotation, unchoked flow, ten running speeds.

illustrates the negligible effect of running speed on the pressure distribution in the seal. This figure has ten curves (corresponding to the ten rotational speed increments) plotted. This accounts for the heavy lines which appear in some cases. This particular plot is of the experimental data for the non-prerotated constant 29 mil clearance smooth seal case. However, none of the pressure plots show any appreciable variation due to running speed.

Figs. 42-55 show the theoretical and experimental pressure data for each of the seals under various prerotation conditions. Due to the absence of running speed dependence, only one speed is plotted for each inlet pressure condition. The numbers on the plotted lines refer to the inlet pressure as defined in Table 7. The lowest pressure for each seal corresponds to unchoked flow through the seal, while the others are choked. The shapes of the pressure-gradient plots show fairly good correspondence between theory and experiment. This is to be expected, however, since the Hirs' coefficients and entrance loss relationship used in the anaylsis come directly from the measured pressures. Generally, the best agreement for each seal occurs for the non-prerotated flow. For prerotated flow in either direction, the theoretical gradient is shifted up slightly. This upward shift is due to a total pressure correction that is made. When the flow is prerotated by the guide-vanes, it is accelerated as well as turned, and the measured static pressure at the vane exit decreases. This explains, in part, why the experimental plots show lower seal entrance pressures for either prerotated case than for the non-prerotated case. Nelson's analysis, however, assumes that the supply pressure upstream of the seal is the total pressure. Hence, the axial component of the

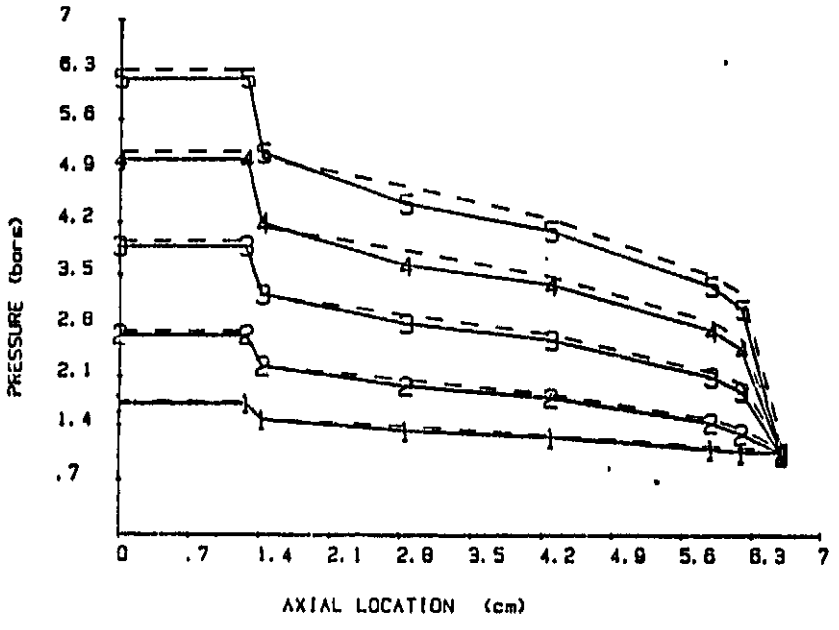

Fig. 42. Axial pressure gradient in seal C1, low speed prerotation in direction of rotor rotation.

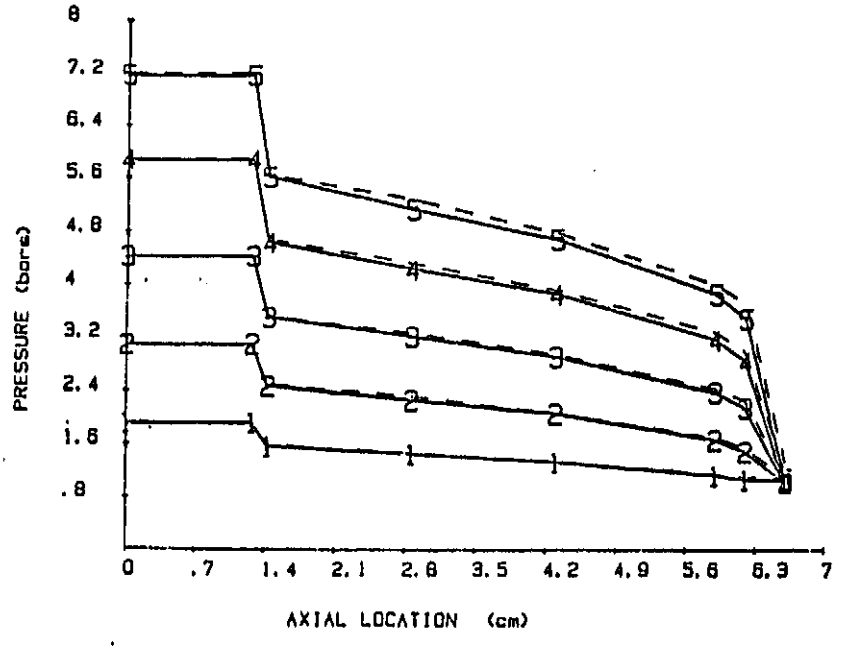

Fig. 43. Axial pressure gradient in seal C1, no prerotation of inlet air.

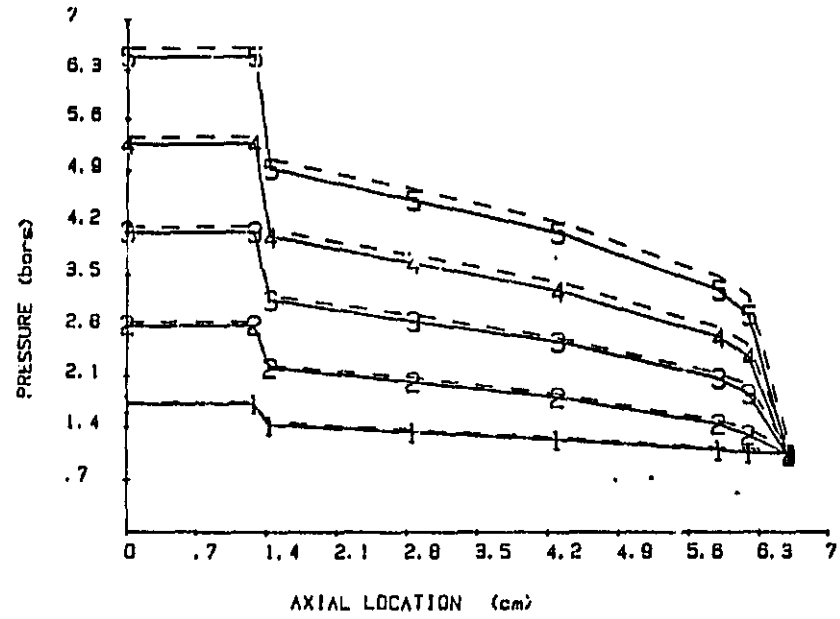

Fig. 44. Axial pressure gradient in seal C1, low speed prerotation opposing rotor rotation.

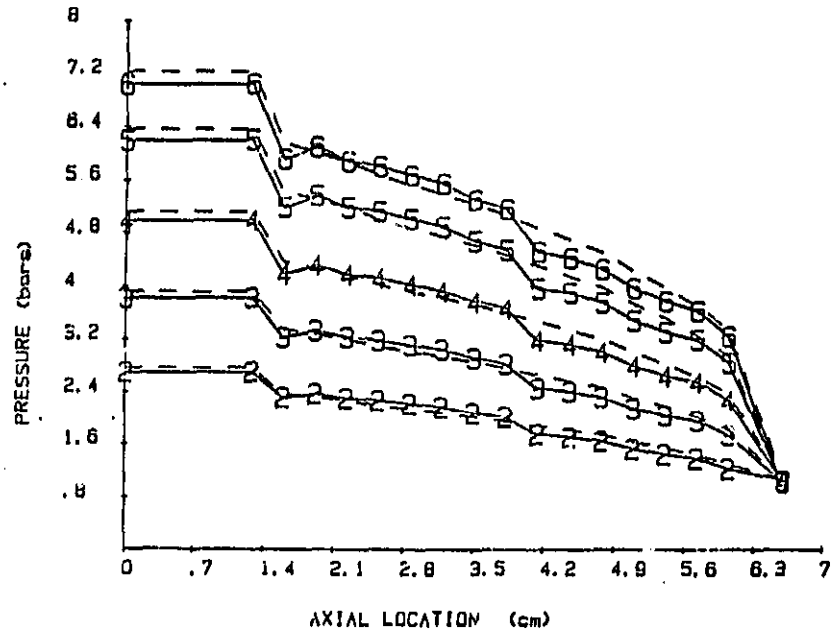

Fig. 45. Axial pressure gradient in seal C2, high speed prerotation in direction of rotor rotation.

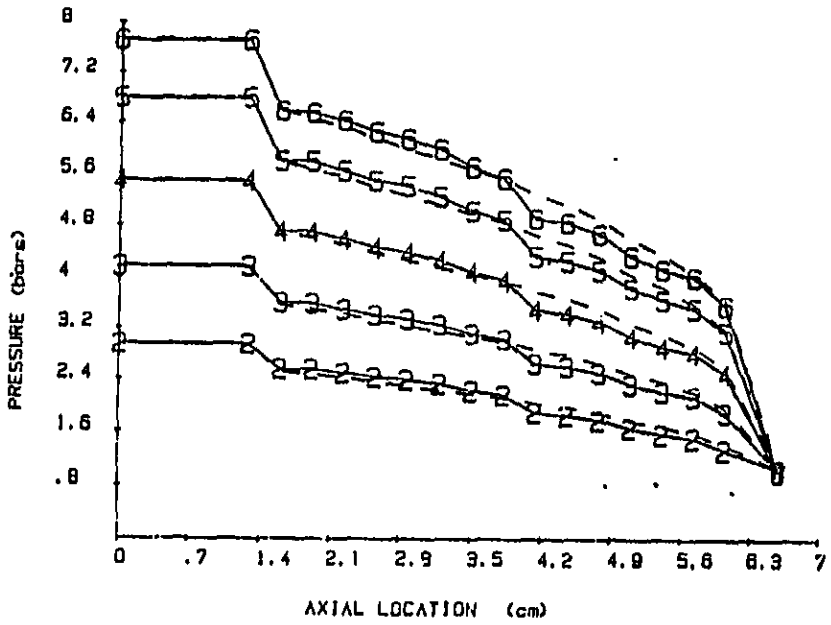

Fig. 46. Axial pressure gradient in seal C2, low speed prerotation in direction of rotor rotation.

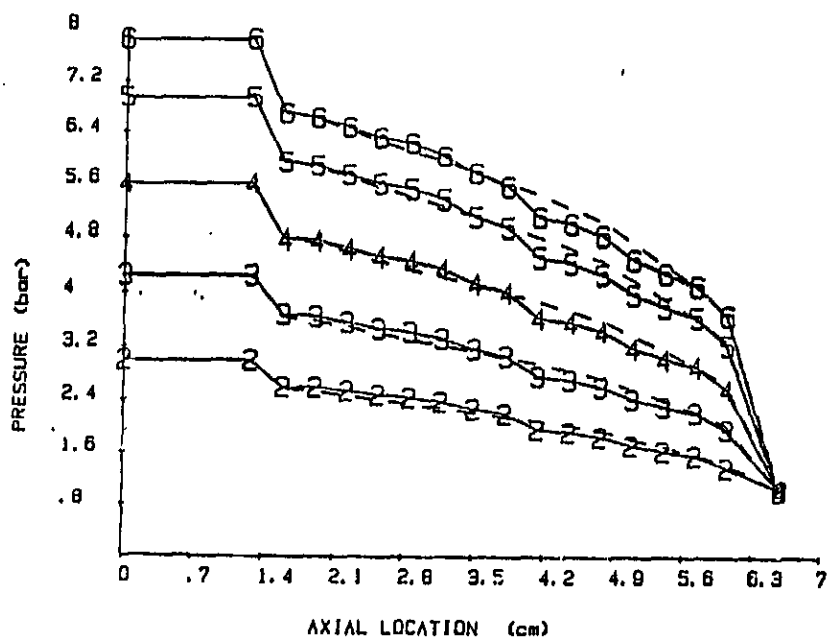

Fig. 47. Axial pressure gradient in seal C2, no prerotation of inlet air.

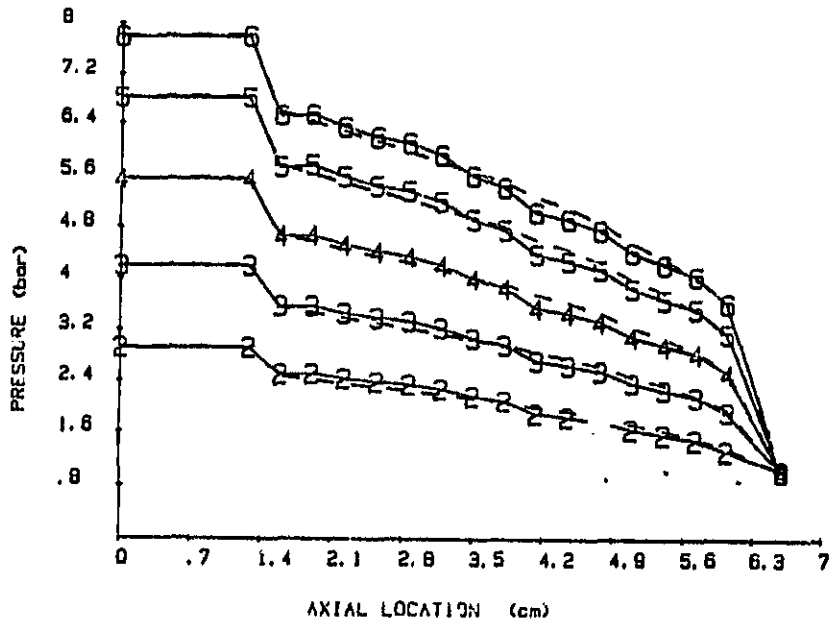

Fig. 48. Axial pressure gradient in seal C2, low speed prerotation opposing rotor rotation.

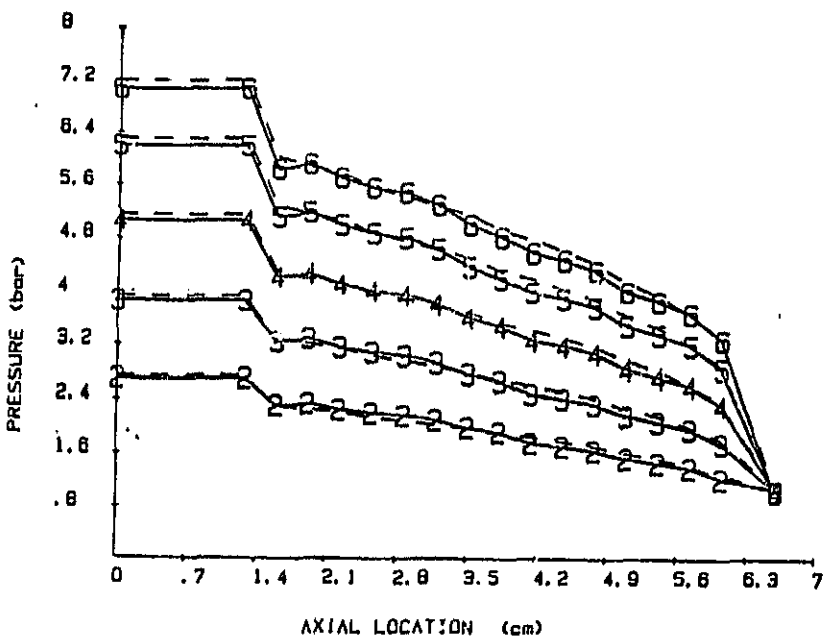

Fig. 49. Axial pressure gradient in seal C2, high speed prerotation opposing rotor rotation.

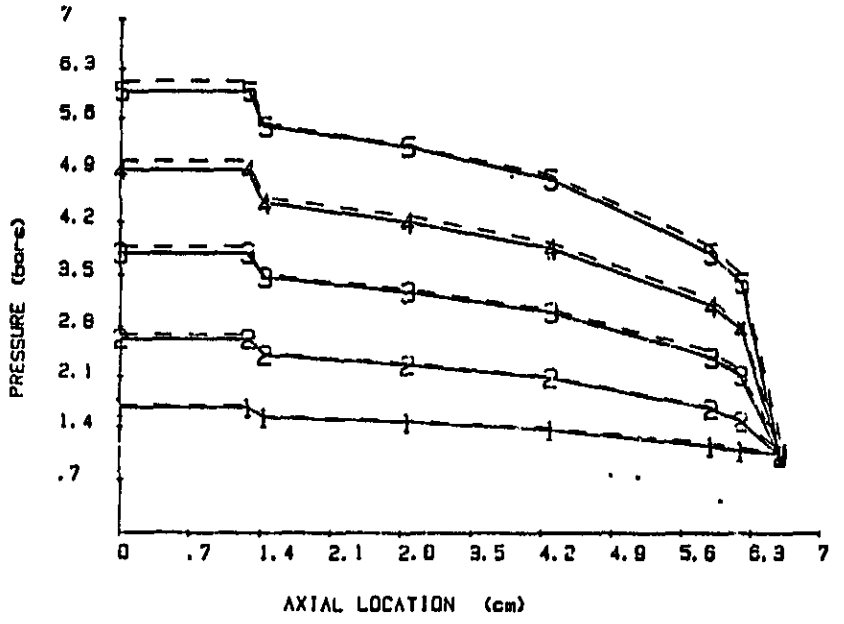

Fig. 50. Axial pressure gradient in seal T, low speed prerotation in direction of rotor rotation.

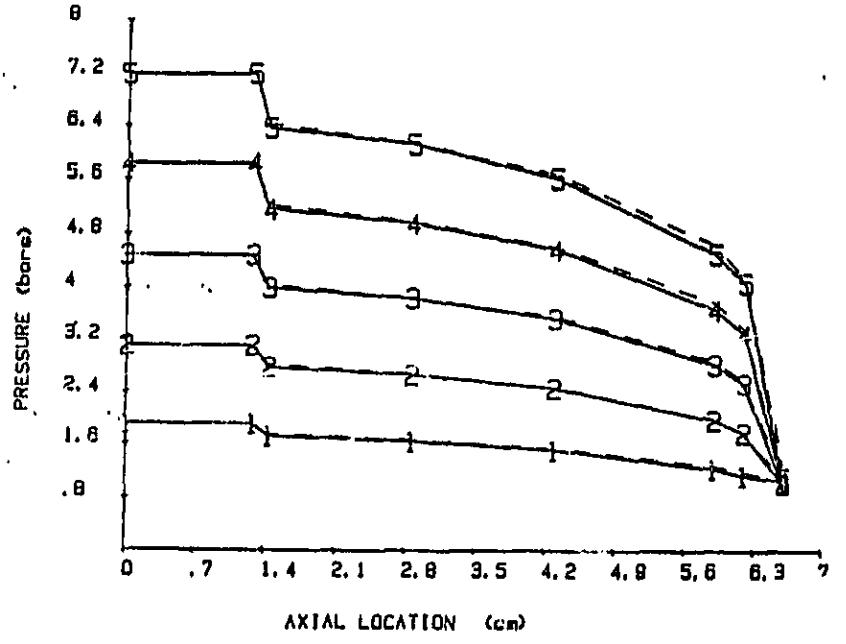

Fig. 51. Axial pressure gradient in seal T, no prerotation of inlet air.

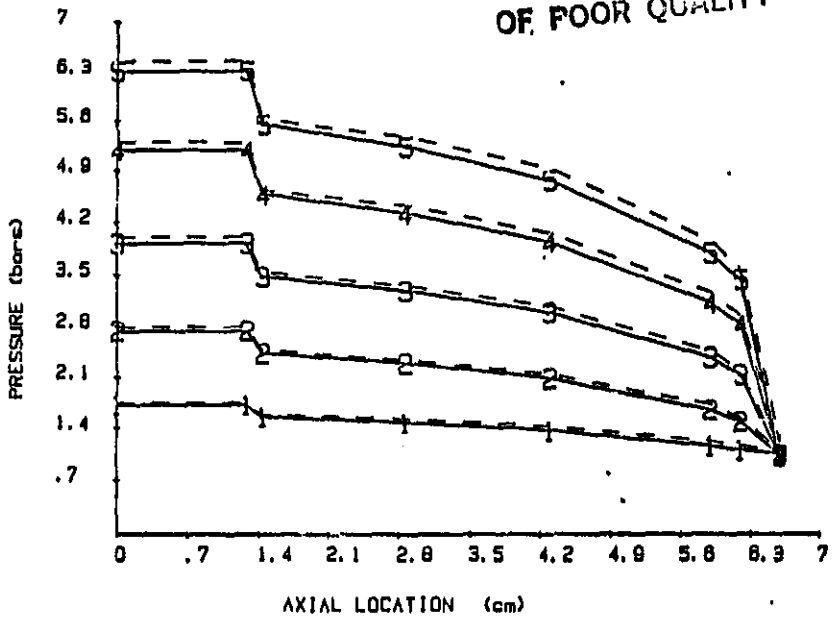

Fig. 52. Axial pressure gradient in seal T, low speed prerotation opposing rotor rotation.

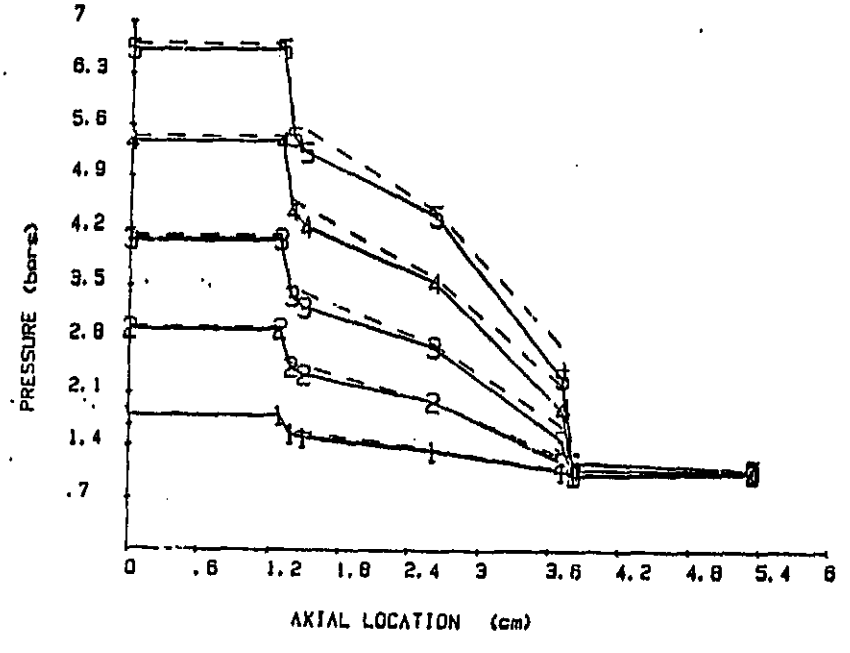

Fig. 53. Axial pressure gradient in seal H, low speed prerotation in direction of rotor rotation.

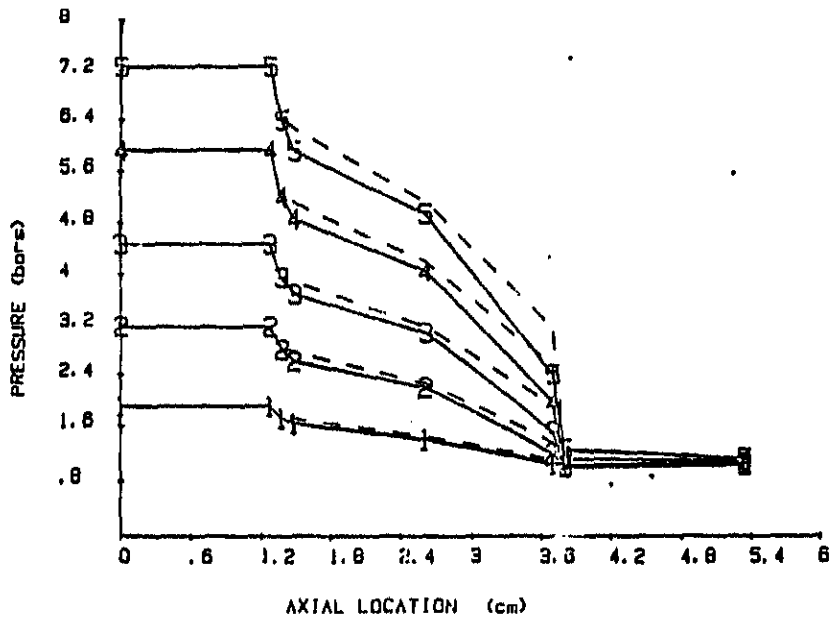

Fig. 54. Axial pressure gradient in seal H, no prerotation of inlet air.

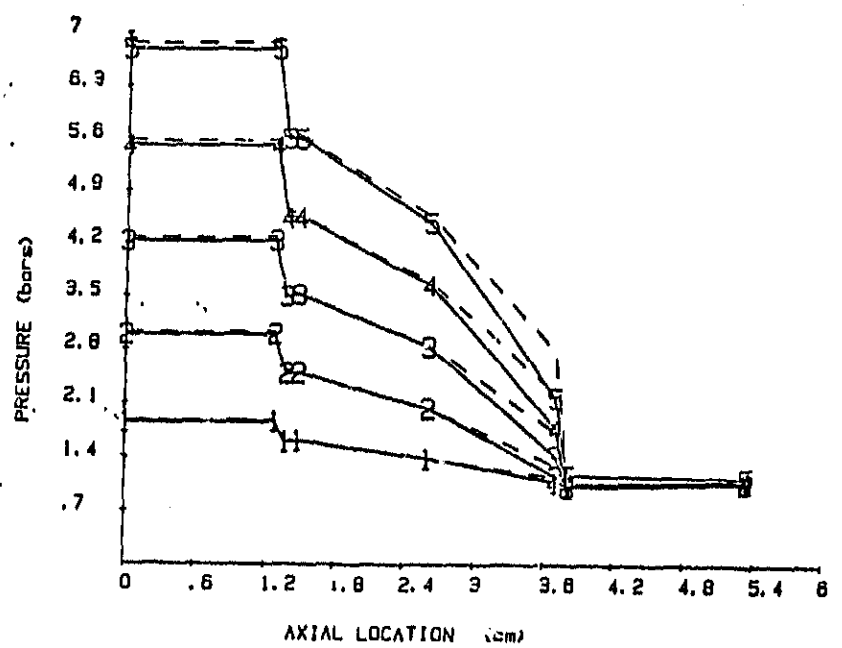

Fig. 55. Axial pressure gradient in seal H, low speed prerotation opposing rotor rotation.

fluid velocity as it leaves the guide-vanes is used to calculate an effective total pressure, which is higher than the measured static pressure. This corrected pressure is then input as the reservoir pressure to Nelson's analysis. The downward shift in the constant 16 mil clearance smooth seal experimental pressure gradient plots (Figs. 45-49) at the 3.8 cm position is partially explained by recalling Fig. 14, "Detail of smooth stator #2." Seal pressures before the shift are from pressure taps "A". Seal pressures after the shift are from pressure taps "B". The shift is greatest in Fig. 45 (high speed swirl with rotation) and diminishes to no shift in Fig. 49 (high speed swirl against rotation).

The inlet tangential velocities as a function of pressure ratio for the seals are given in Figs. 56-59. Curves 1 and 4 represent the tangential velocities attained using the aluminum swirl vanes described in "Test Hardware." Curves 2 and 3 represent the tangential velocities attained using the brass swirl vanes. The non-prerotated case is represented by the x-axis, or zero inlet tangential velocity. The figures show that the velocity remained fairly constant over the pressure ratios tested. The negative numbers shown in the figures mean that the inlet tangential velocity was opposed to the direction of rotor rotation. The positive numbers mean that the inlet tangential velocity was in the same direction as rotor rotation.

Dynamic Results. For all seals except the constant 16 mil clearance smooth seal, dynamic tests were performed at shaking frequencies of 58.8, 74.6, and 124.6 Hz. As was discussed in the Data Acquisition section of this report, these frequencies were chosen to provide the desired sample rate and a steady trigger signal. The dynamic

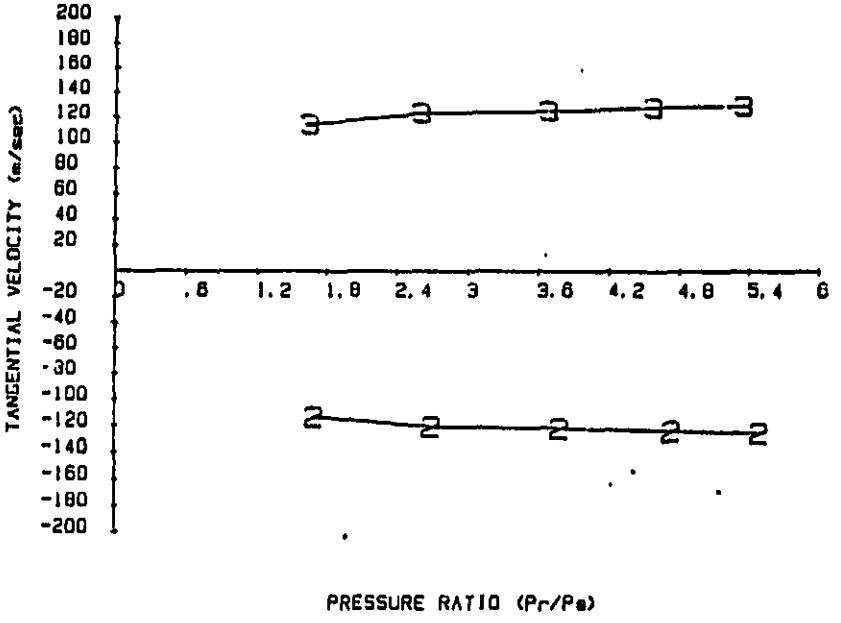

Fig. 56. Inlet tangential velocity vs. pressure ratio for 29 mil clearance seal (C1).

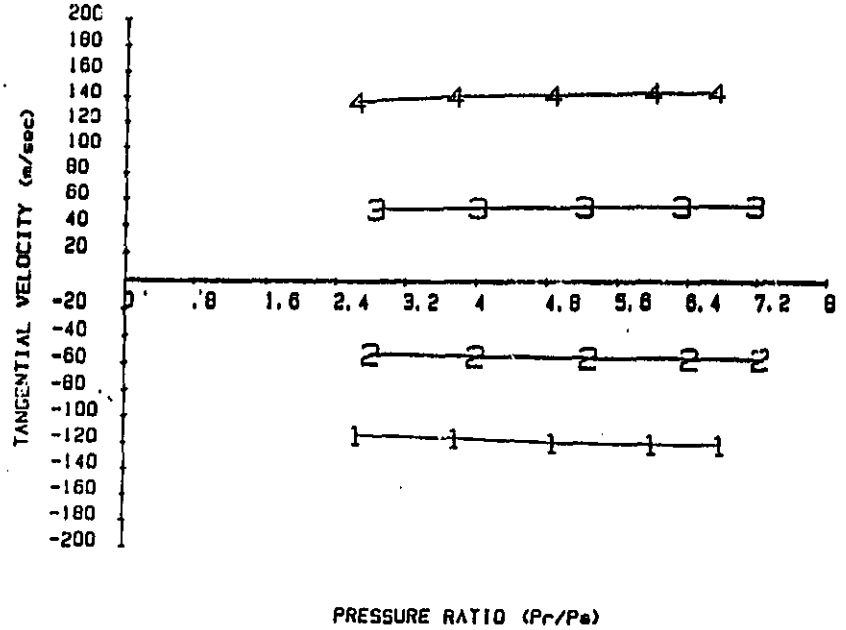

Fig. 57. Inlet tangential velocity vs. pressure ratio for 16 mil clearance seal (C2).

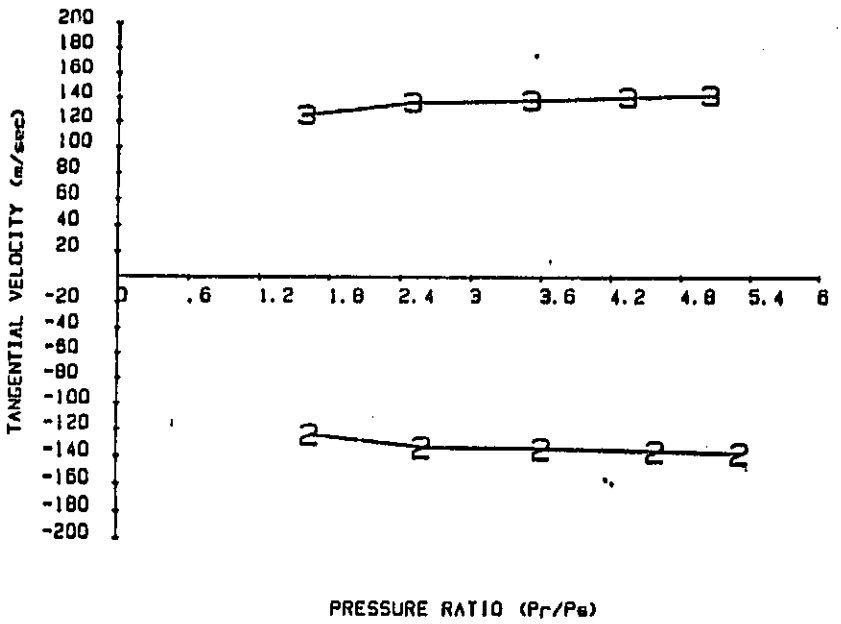

Fig. 58. Inlet tangential velocity vs. pressure ratio for convergent tapered seal (T).

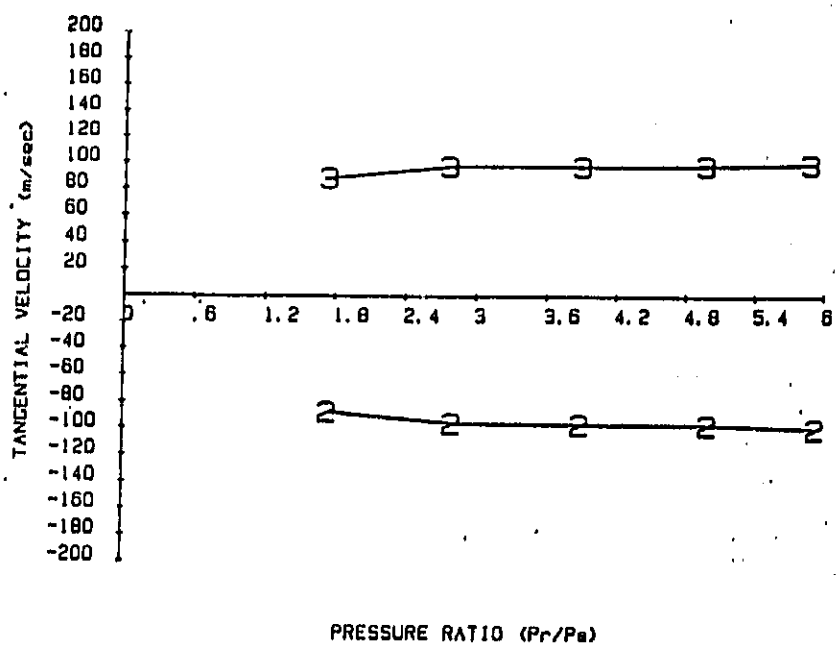

Fig. 59. Inlet tangential velocity vs. pressure ratio for honeycomb seal (H).

coefficients obtained at the two lower frequencies are essentially the same. At the 124.6 Hz shaking frequency, however, correspondence of the data to that obtained at the lower frequencies is unsatisfactory. In seeking to explain the discrepancy, tests were run to determine the relative transfer function of the test apparatus. The plots in Fig. 60 show the results of these tests, and indicate a resonance of the apparatus occurring at approximately 25 Hz (the drop in phase difference at approximately 45 Hz corresponds to a resonance of the shaker support structure). As the shaking frequency is increased above this, the input force levels required to achieve a given motion amplitude increase rapidly. At the 124.6 Hz shaking frequency, attainable motion amplitude is about 50% of that achieved at the 58.8 and 74.6 Hz frequencies. Therefore, one possible explanation for the poor agreement between the results is that as motion amplitude decreases, so does the force measured by the load cells, and the measurement system resolution suffers. For this reason, the 16 mil clearance seal was not tested at 124.6 Hz.

Relative Uncertainty. Before proceeding with the dynamic results, a statement must be made concerning the uncertainty present in the experimental results. Using the method described by Holman [22], the uncertainty in the dynamic coefficients can be determined using equations (17). As mentioned in the Instrumentation section, the uncertainty in the load cell force measurements was 0.89 N (0.2 lb), 0.13 Hz for the frequency, and 0.0013 mm (0.05 mils) for the motion. For the 16 mil clearance seal, the resulting maximum uncertainty in the stiffness coefficients was 15 kN/m (86 lb/in) and 203 N-sec/m (1.2 lb-sec/in) for the damping coefficients. Among the other three

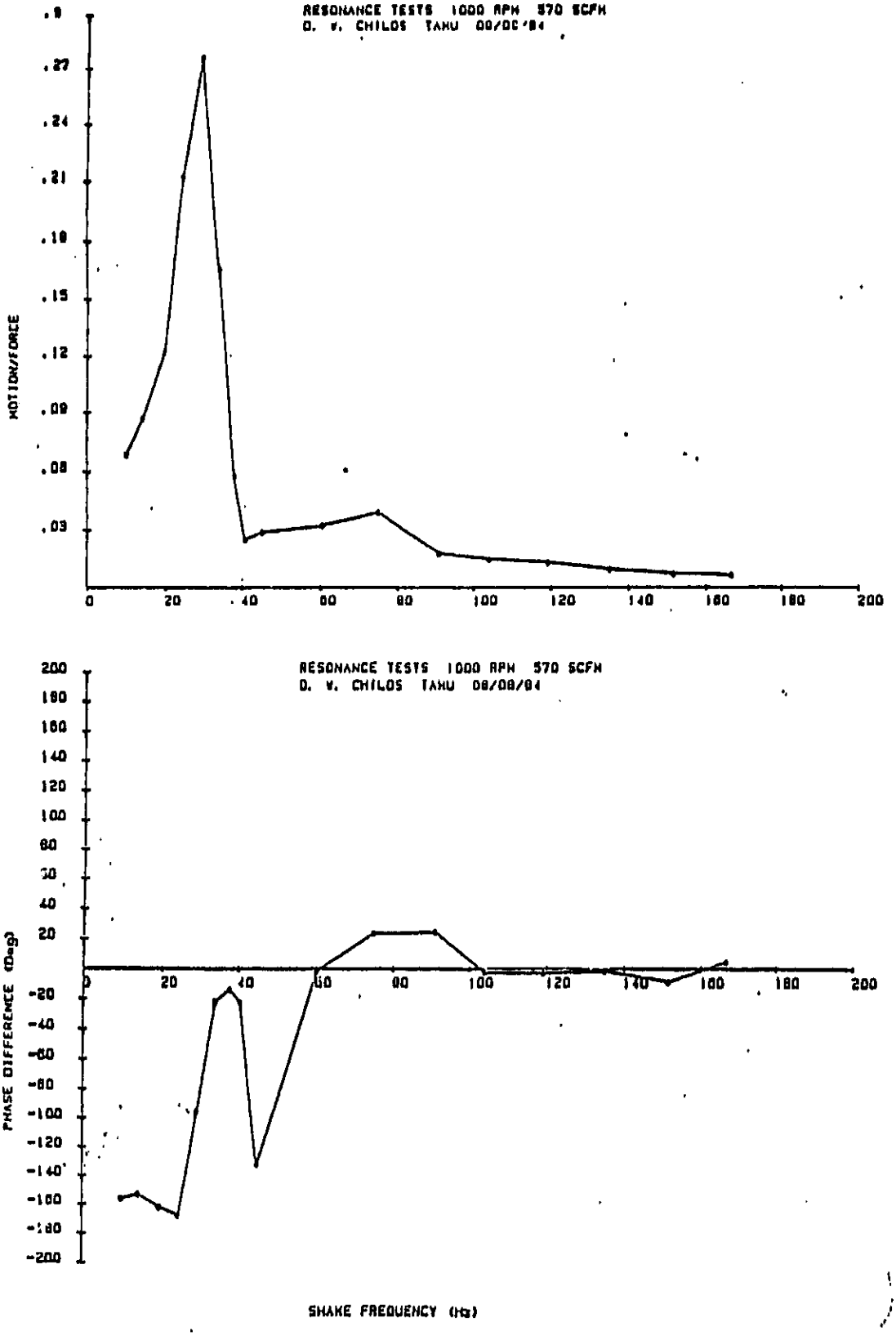

Fig. 60 Relative transfer function of test apparatus.

seals, the maximum uncertainty in the stiffness coefficients was 7.7 kN/m (44 lb/in) and 103 N-sec/m (0.59 lb-sec/in) for the damping coefficients.

Dynamic Results - Theory / Experiment Comparison. Plots of the seal rotordynamic coefficients are found in Figs. 61-76. These plots include both the theoretical and experimental data. The coefficients are plotted versus the reservoir / sump-pressure ratio, the solid lines again correspond to the theoretical data, and the symbols used are defined in Table 5. The test results plotted here were obtained by shaking the rotor with a maximum amplitude of seven mils at 74.6 Hz. In general, the predicted signs of the coefficients are consistent with test data. In addition, the generally predicted trend of increasing coefficient magnitude with increasing pressure ratio compares favorably with experimental results. However, the magnitude of the difference between predicted and averaged experimental results increases with increasing pressure ratio.

Dynamic Results - Seal C1. For the constant 29 mil clearance smooth seal, direct stiffness (Fig. 61) is underpredicted for prerotation in the direction of rotor rotation and overpredicted for the other two prerotation conditions. Best agreement is seen in the case for no prerotation. The predictions are generally 60% to 70% low for prerotation in the direction of rotor rotation, 70% to 80% low for prerotation opposing rotor rotation, and from 23% low to 30% high for no prerotation.

In the cross-coupled stiffness comparison for this seal (Fig. 62), theory overpredicts the magnitude for both prerotation conditions, and underpredicts for the non-prerotated case. The

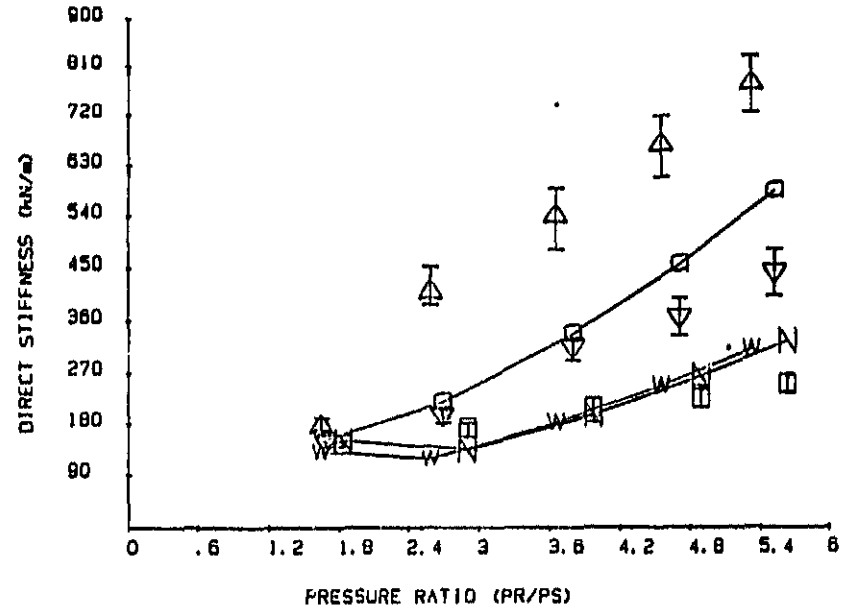

Fig. 61. Direct stiffness of seal C1 (29 mil clearance): theoretical and experimental.

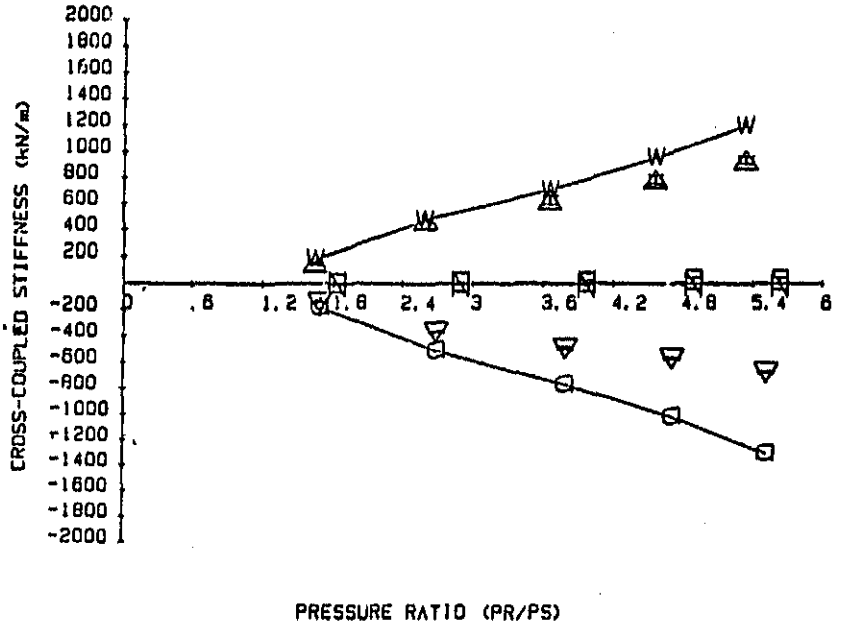

Fig. 62. Cross-coupled stiffness of seal C1: theoretical and experimental.

non-prerotated case shows a divergence both in magnitude and sign. It should be noted, however, that the magnitudes for this case are significantly smaller than for either of the prerotated cases. The cross-coupled stiffness magnitude is overpredicted by 27% or less for prerotation in the direction of rotor rotation and by 32% to 96% for prerotation opposing rotor rotation.

Agreement between theory and experiment for direct damping (Fig. 63) is the most favorable of all the dynamic coefficients. Theory underpredicts for the case of no prerotation by less than 8% for the highest three reservoir / sump pressure ratios and up to 33% for the lower two pressure ratios. For the other prerotation conditions, the direct damping is underpredicted at the lower pressure ratios and overpredicted at higher pressure ratios. These predictions are within 13% of the average measured direct damping at all pressure ratios.

Cross-coupled damping (Fig. 64) for this smooth seal generally shows agreement in the trends for the theoretical and experimental results. For prerotation in and opposing the direction of rotor rotation, the theory underpredicts cross-coupled damping magnitude by approximately 60% and 35%, respectively. For the non-prerotated case, the theory predicts coefficients so small as to be considered negligible. This is not inconsistent with the test results, however, as the magnitudes for this case are significantly smaller than for either prerotated case.

Dynamic Results - Seal C2. The direct stiffness of the constant 16 mil clearance smooth seal (Fig. 65) was underpredicted for all prerotation conditions. An increase of direct stiffness with increasing pressure was again predicted and measured, but the order of

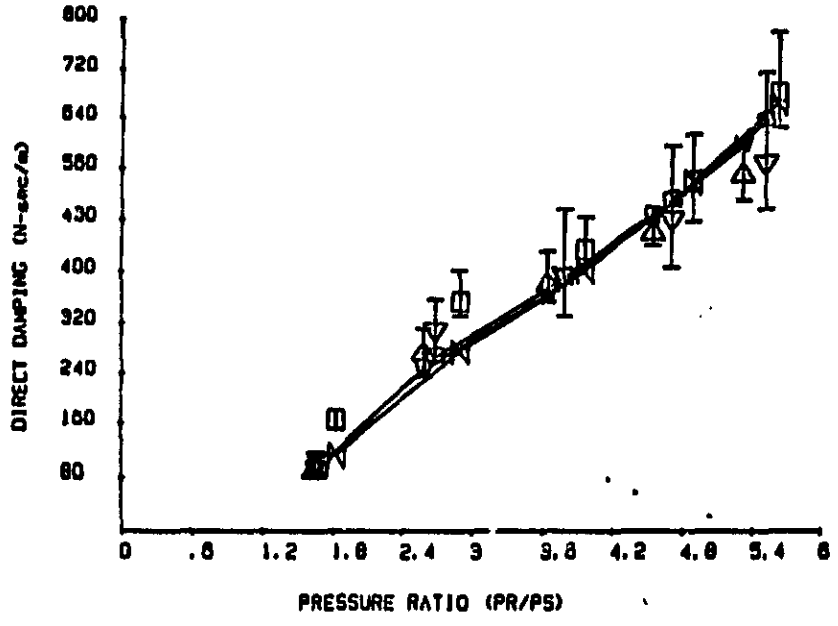

Fig. 63. Direct damping of seal C1 (29 mil clearance): theoretical and experimental.

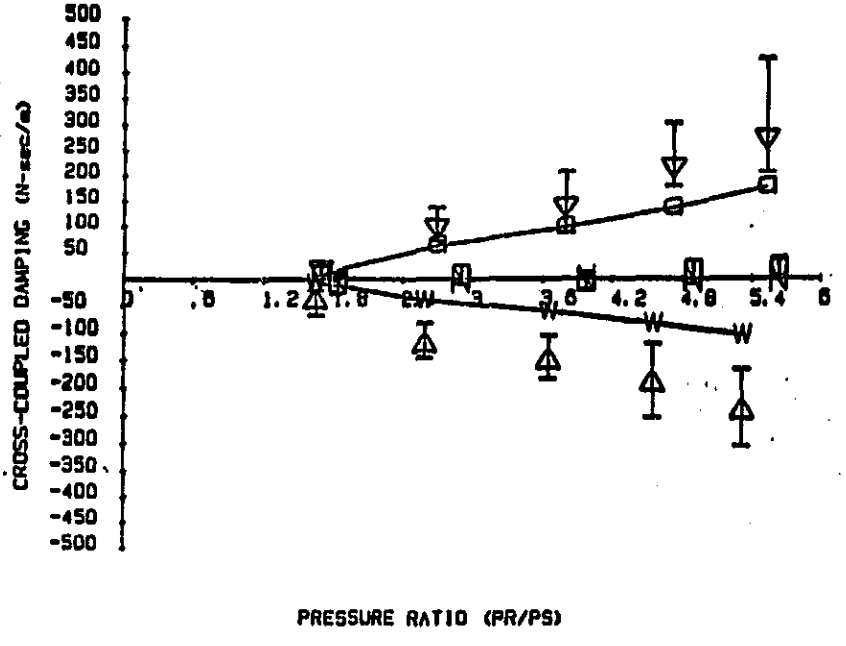

Fig. 64. Cross-coupled damping of seal C1: theoretical and experimental.

C-2

increasing stiffness with swirl configuration differs for theory and experiment. The highest direct stiffness was predicted for high speed prerotation against rotor rotation, followed by high speed prerotation with rotor rotation and low speed prerotation against rotor rotation, followed by low speed prerotation with rotor rotation and no prerotation. The highest measured direct stiffness was for high speed prerotation with rotor rotation, followed by low speed prerotation with rotor rotation, no prerotation, low speed prerotation against rotor rotation, and high speed prerotation against rotor rotation. For prerotation in the direction of rotor rotation, the predictions are below the average measured stiffnesses by from 81% to 84%. For no prerotation, the predictions are low by from 71% to 81%. For low speed prerotation opposing rotor rotation (brass swirl vanes), the predictions are low by 61% to 63%, while for high speed prerotation opposing rotor rotation (aluminum swirl vanes), the predictions are low by 32% to 49%.

Agreement between theory and experiment for cross-coupled stiffness (Fig. 66) is the most favorable of the dynamic coefficients for this seal. The magnitude of the cross-coupled stiffness is overpredicted for both high speed swirl configurations (less than 10% over for swirl opposing rotation, less than 23% over for swirl with rotation), underpredicted for low speed swirl with rotor rotation (18% to 39% under) and for no prerotation, and predicted for low speed swirl against rotor rotation (within 4%). An additional plot of the experimentally determined cross-coupled stiffness of this seal, Fig. 67, illustrates the dependence of this coefficient on the circumferential air velocity. Each of the five curves represents the

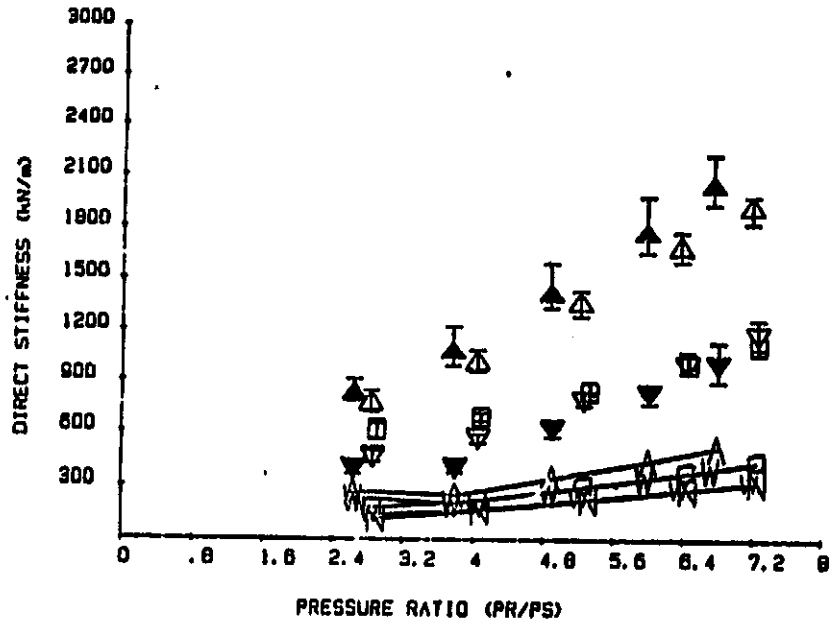

Fig. 65. Direct stiffness of 16 mil clearance seal (C2): theoretical and experimental.

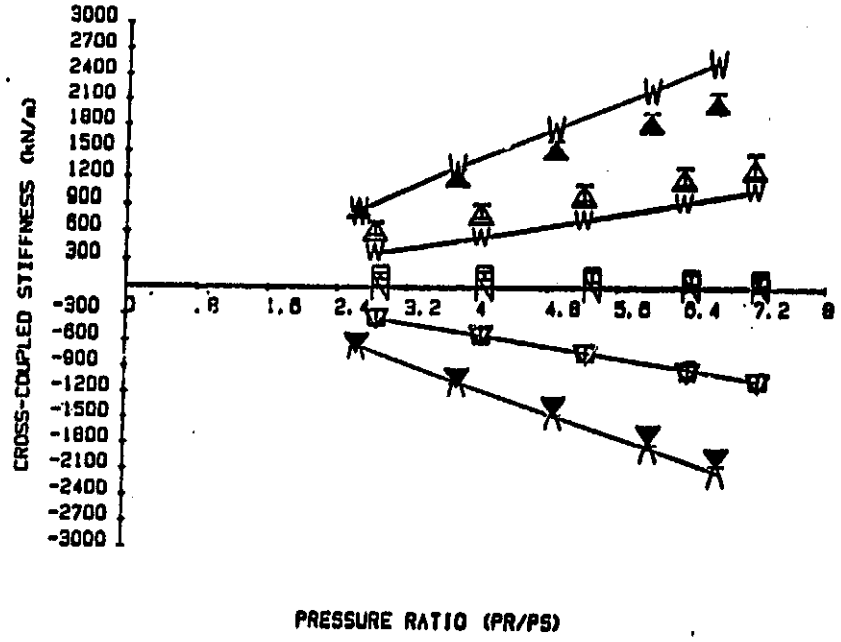

Fig. 66. Cross-coupled stiffness of seal C2: theoretical and experimental

variation of the cross-coupled stiffness at a constant pressure ratio as the swirl vanes are changed. The curves are labeled 2-6 from the lowest to the highest reservoir / · sump pressure ratio. The five labeled points on each curve represent the five swirl vane configurations used in testing this seal. From left to right these are: aluminum guide-vanes against rotor rotation, brass guide-vanes against rotor rotation, no prerotation, brass guide-vanes with rotor rotation, and aluminum guide-vanes with rotor rotation. The figure shows the increasing instability (positive cross-coupled stiffness) with increasing tangential velocity in the direction of rotor rotation (positive tangential velocity), and the increasing stability (negative cross-coupled stiffness) with increasing tangential velocity opposite the direction of rotor rotation (negative tangential velocity). The figure also illustrates the minor dependence of tangential velocity on pressure ratio for a given set of swirl vanes. The results plotted are from tests at 3000 rpm and are typical of tests at other running speeds.

Direct damping (Fig. 68) is underpredicted for all prerotation conditions. The underprediction is greatest for high speed prerotation against rotor rotation and least for low speed prerotation with rotor rotation. Experimental results indicate some dependence of direct damping on prerotation condition, while theory predicts none.

Cross-coupled damping (Fig. 69) for this seal is underpredicted for both prerotations against rotor rotation (78% to 87% low), for low speed prerotation with rotor rotation (26% to 67% low), and for no prerotation, with the magnitude of the underprediction growing with increasing pressure ratio. Predictions for high speed prerotation

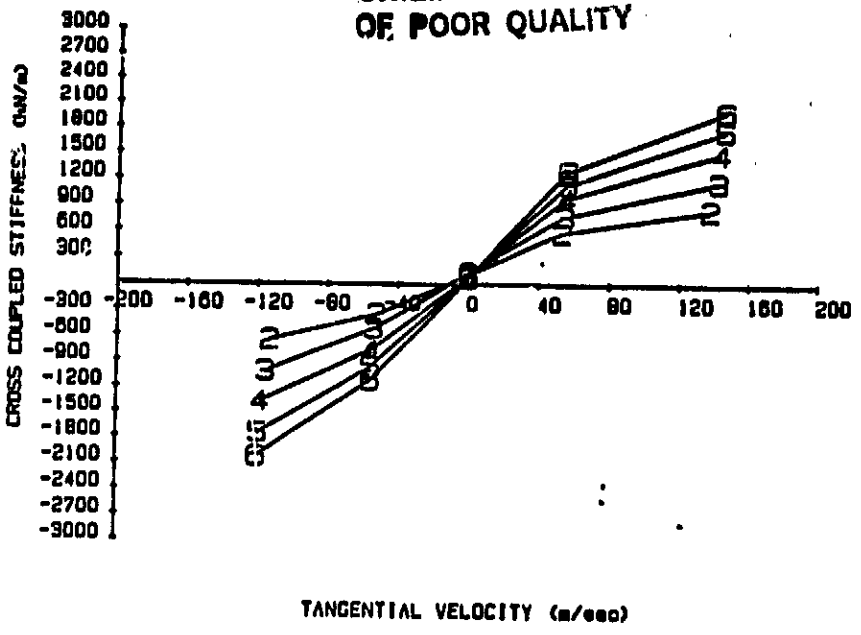

Fig. 67. Dependence of 16 mil clearance seal (C2) cross-coupled stiffness on tangential velocity of inlet air (at 3000 rpm). Pressure ratios 2-6 are identified in Table 7.

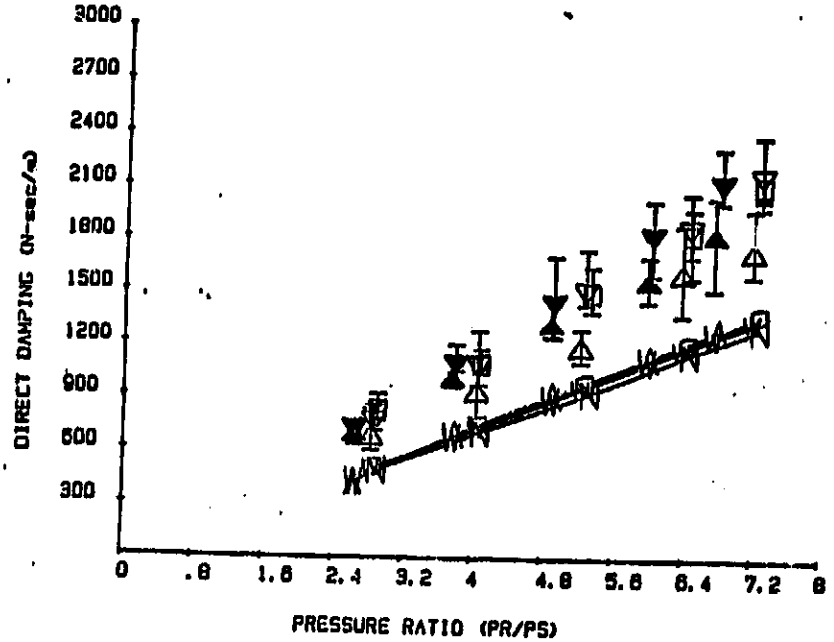

Fig. 68. Direct damping of seal C2: theoretical and experimental.

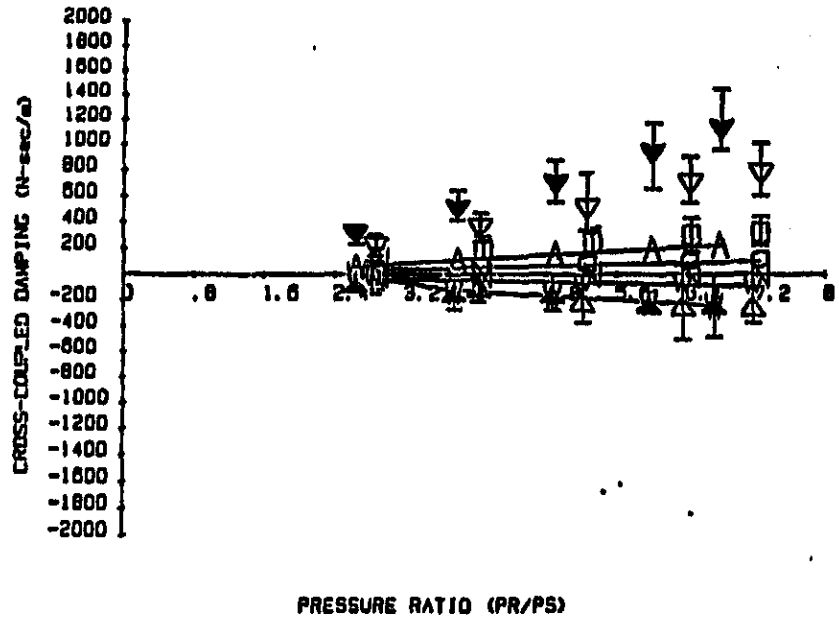

Fig. 69. Cross-coupled damping of 16 mil clearance seal (C2): theoretical and experimental.

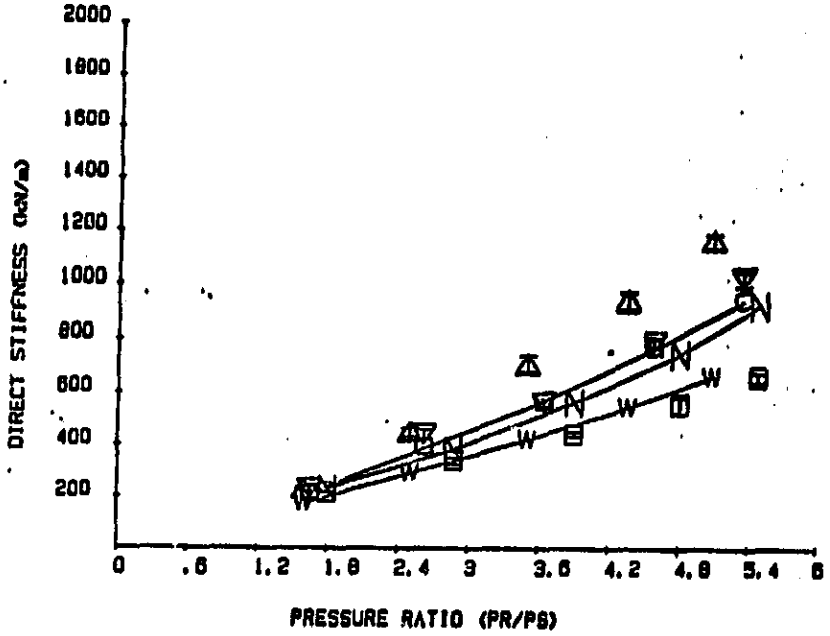

Fig. 70. Direct stiffness of convergent tapered seal (T): theoretical and experimental.

with rotor rotation are the most favorable (within 18% of average measured cross-coupled damping).

Dynamic Results - Seal T. The direct stiffness of the convergent tapered seal (Fig. 70) is underpredicted for both prerotated cases and overpredicted in the case of no prerotation. Best agreement is seen for prerotation opposite rotor rotation (predictions within 13% of average measured direct stiffness). For prerotation with rotor rotation, predictions are from 24% to 43% low. For no prerotation, predictions are from 7% to 39% high.

The magnitude of the cross-coupled stiffness of the tapered seal (Fig. 71) is overpredicted for both prerotated cases: from 24% to 43% high for prerotation in the direction of rotor rotation and from 44% to 86% high for prerotation opposing rotor rotation. The predictions are slightly low in the case of no prerotation.

Direct damping (Fig. 72) is underpredicted for all prerotation conditions. Both theory and experiment show little dependence of the damping magnitude on prerotation condition. All predictions are within 32% of the average measured cross-coupled stiffnesses.

The magnitude of the cross-coupled damping of the tapered seal (Fig. 73) is underpredicted for all prerotation cases. The predictions for the case of prerotation in the direction of rotor rotation are almost zero compared to the other prerotated predictions and to the prerotated measurements.

Dynamic Results - Seal H. The direct stiffness of the honeycomb seal (Fig. 74) is underpredicted by up to 67% for all cases of prerotation. With both experimental and theoretical data, the magnitude of the direct stiffness is greatest for the prerotated cases, with little

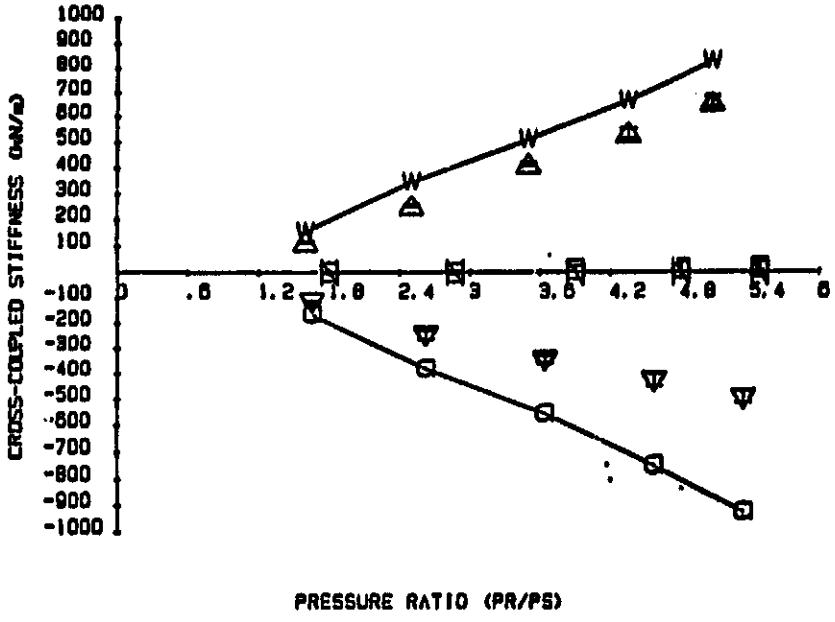

Fig. 71. Cross-coupled stiffness of tapered seal (T): theoretical and experimental.

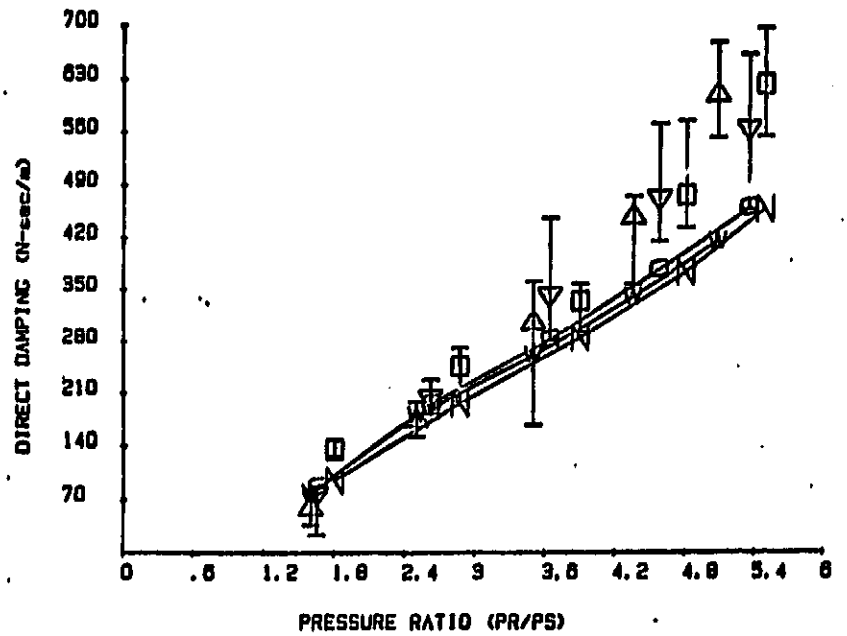

Fig. 72. Direct damping of seal T: theoretical and experimental.

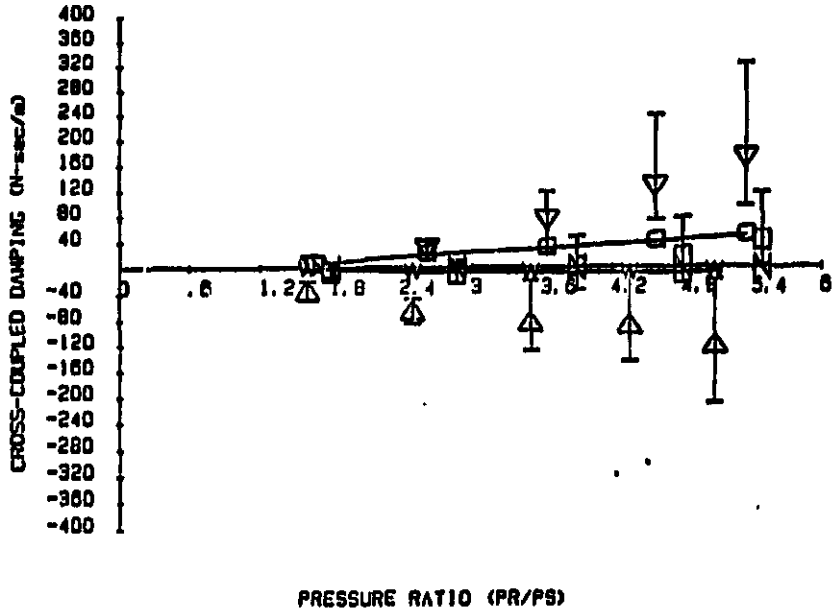

Fig. 73. Cross-coupled damping of tapered seal (T): theoretical and experimental.

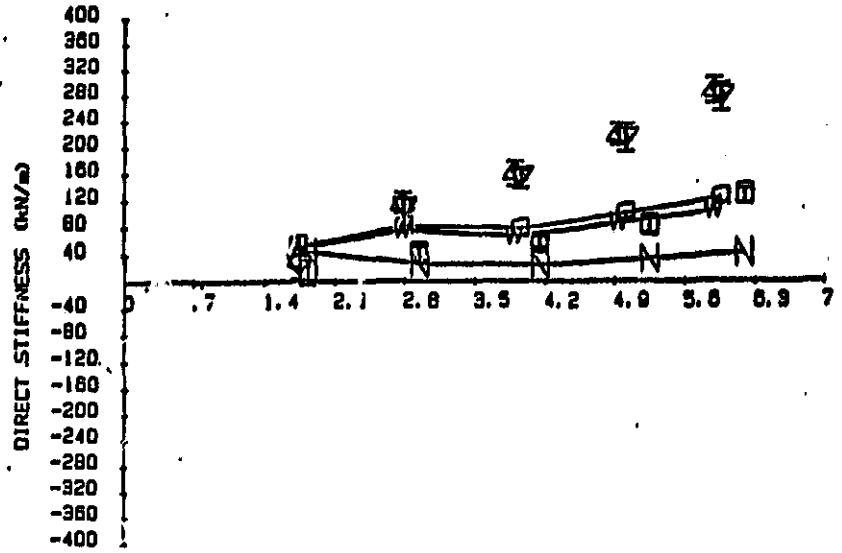

Fig. 74. Direct stiffness of honeycomb seal (H): theoretical and experimental.

dependence on prerotation direction.

In the cross-coupled stiffness comparison (Fig. 75), the theory underpredicts the magnitudes, but correctly predicts the signs of the coefficients. For the non-prerotated case, the predicted stiffnesses are essentially zero. The relative magnitudes of the experimental results for this same case in comparison to either prerotated case are also quite small, however. For prerotation in the direction of rotor rotation, theoretical cross-coupled stiffnesses are from 9% to 26% less the experimental averages. For counter prerotation, theory underpredicts the average experimental magnitudes by from 36% to 51%.

With the exception of the non-prerotated case, agreement between theory and experiment is good for the direct damping coefficients (Fig. 76) of the honeycomb seal. In the non-prerotated case, theory underpredicts the coefficients by approximately 50%. Generally, the prerotated cases show agreement to within 10%.

Theoretical results for the cross-coupled damping coefficients (Fig. 77) of the honeycomb seal are small enough to be considered negligible. In every case, the theory underpredicts the coefficients by a wide margin. However, the trend of increasing magnitude with increasing pressure ratio, as well as the signs of the coefficients, agree.

Dynamic Results - Comparison of Seals. Comparisons of the experimentally obtained rotordynamic coefficients of the two constant clearance smooth seals tested (C1 and C2 described in Table 3) are presented in Figs. 78-81. Comparisons of seals C1 and T are presented in Figs. 82-85. See Table 6 for definitions of the symbols used in these figures. The location of each symbol represents the value of

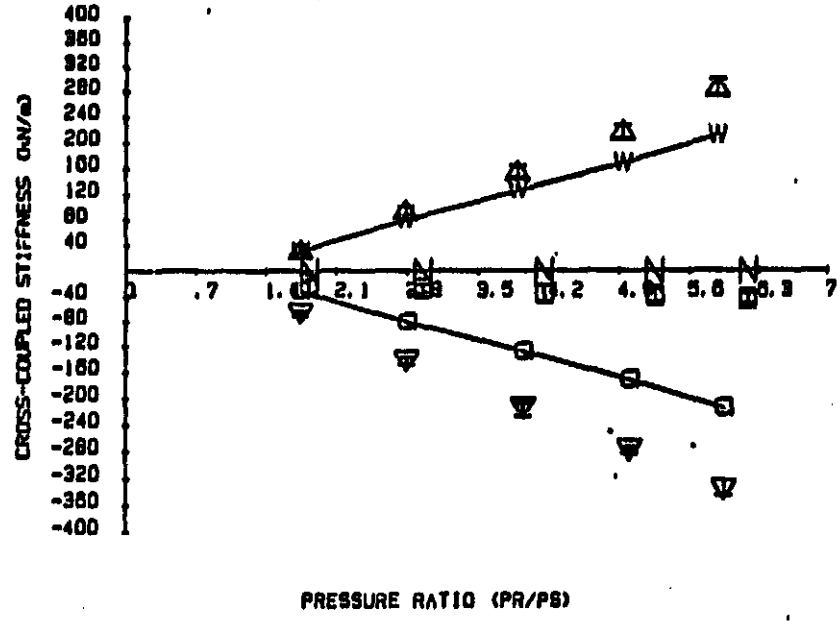

Fig. 75. Cross-coupled stiffness of honeycomb seal (H): theoretical and experimental.

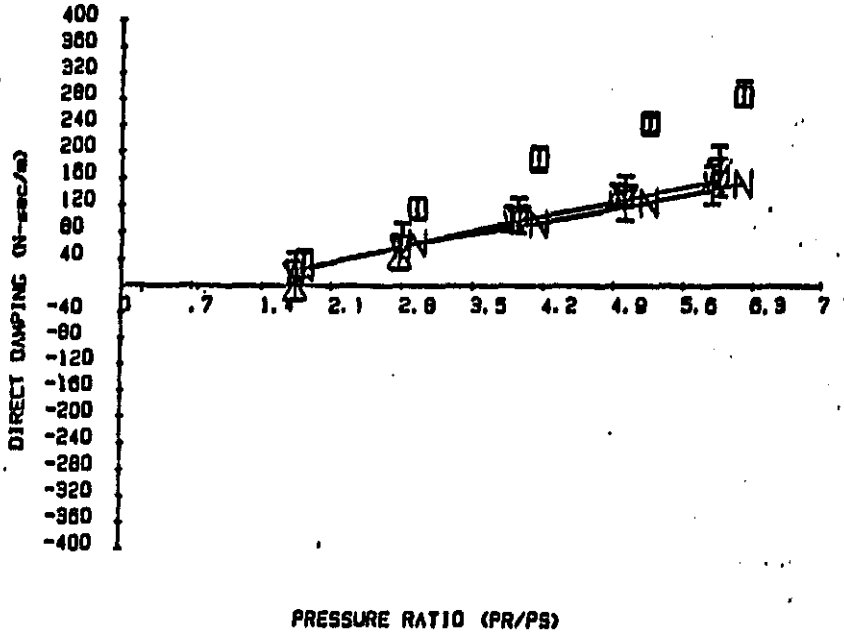

Fig. 76. Direct damping of seal H: theoretical and experimental.

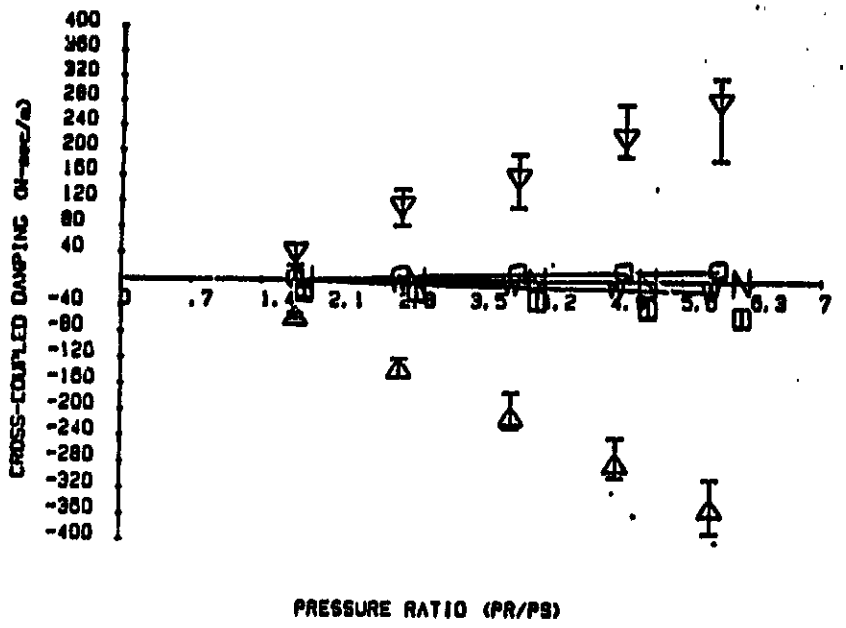

Fig. 77. Cross-coupled damping of honeycomb seal (H): theoretical and experimental.

the coefficient averaged over all running speeds at a reservoir / sump pressure ratio. Coefficient ratios are excluded for the non-prerotated cross-coupled terms because all such terms are near zero.

Dynamic Results - C1 vs. C2. As stated previously, the only significant difference between C1 and C2 is the clearance - 29 mils vs. 16 mils. A comparison of the experimental results from testing the two seals sheds light on the effect of a change in clearance on rotordynamic coefficients.

Fig. 78 provides a comparison of the direct stiffness of C1 and C2. While the direct stiffness for prerotation with rotor rotation is considerably greater than for the other prerotation cases for each seal, the ratio of the direct stiffness of C2 to C1 is generally from 1.8 to 2.0 for both prerotated cases for pressure ratios from 2.8 to 5.5. For no prerotation, the stiffness ratio is from 3.3 to 3.6.

Fig. 79 reveals that the cross-coupled stiffness of C2 exceeds that of C1 for prerotation with rotor rotation, with the ratio decreasing from 1.2 to 1.1 for a pressure ratio from 2.8 to 5.5. For prerotation counter to rotor rotation, the stiffness ratio increases from 0.9 to 1.2 as the pressure ratio increases. For no prerotation, both seals have small positive cross-coupled stiffnesses, with the stiffness of C2 exceeding that of C1 throughout the pressure range.

In a comparison of the direct damping of the two seals (Fig. 80), the ratio of the direct damping of C2 to that of C1 is a constant 2.3 for prerotation in the direction of rotor rotation. In the non-prerotated case, the ratio ranges from 2.3 to 2.5. For prerotation opposing rotor rotation, the ratio increases from 2.4 to 2.9.

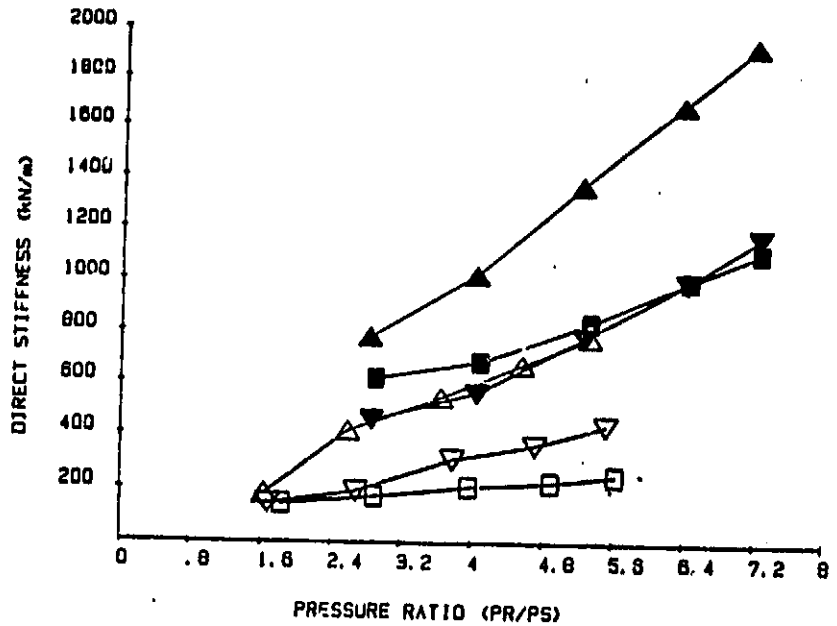

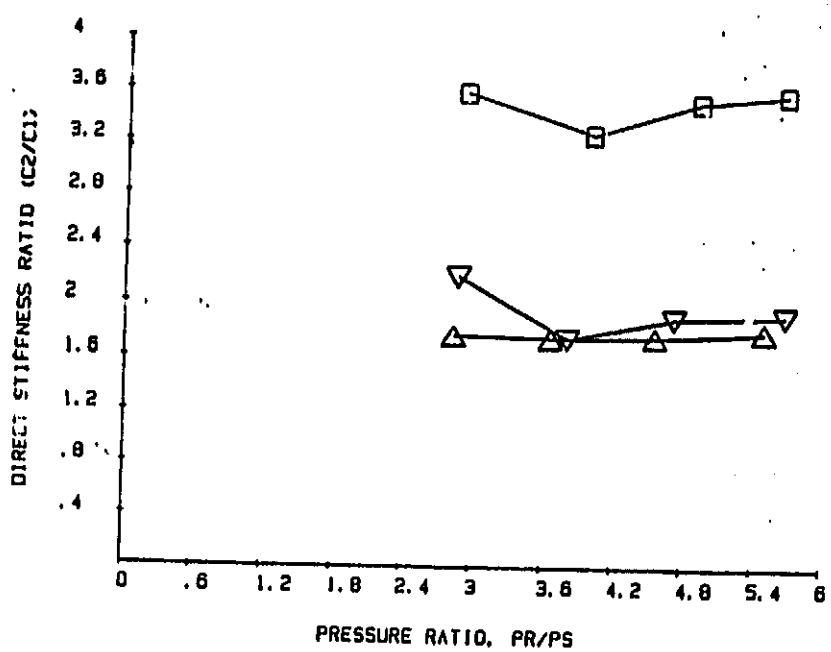

Fig. 78. Direct stiffness comparison of seals C1 and C2. (C1 clearance = 29 mils; C2 clearance = 16 mils)

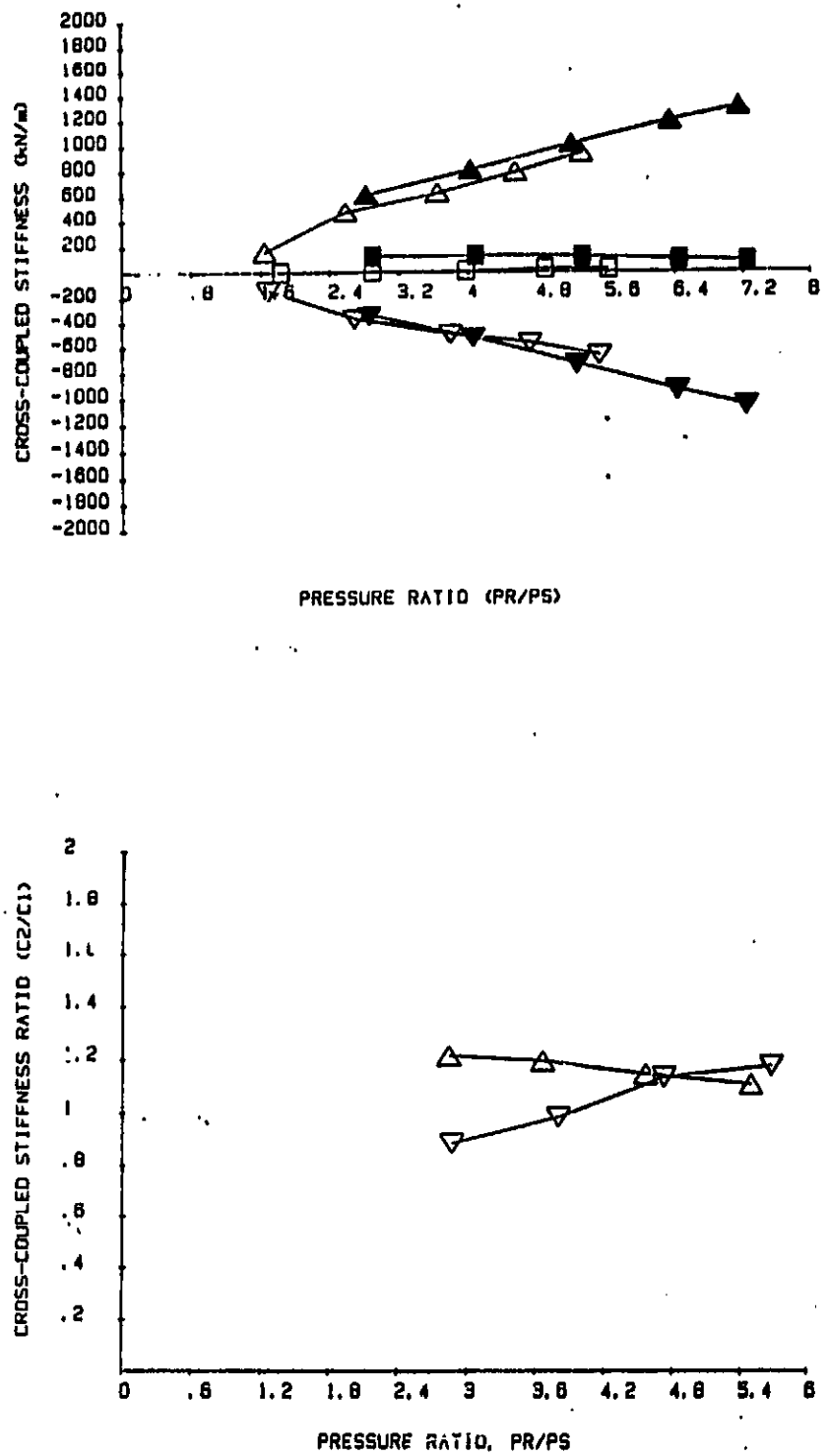

Fig. 79. Cross-coupled stiffness comparison of seals C1 and C2.

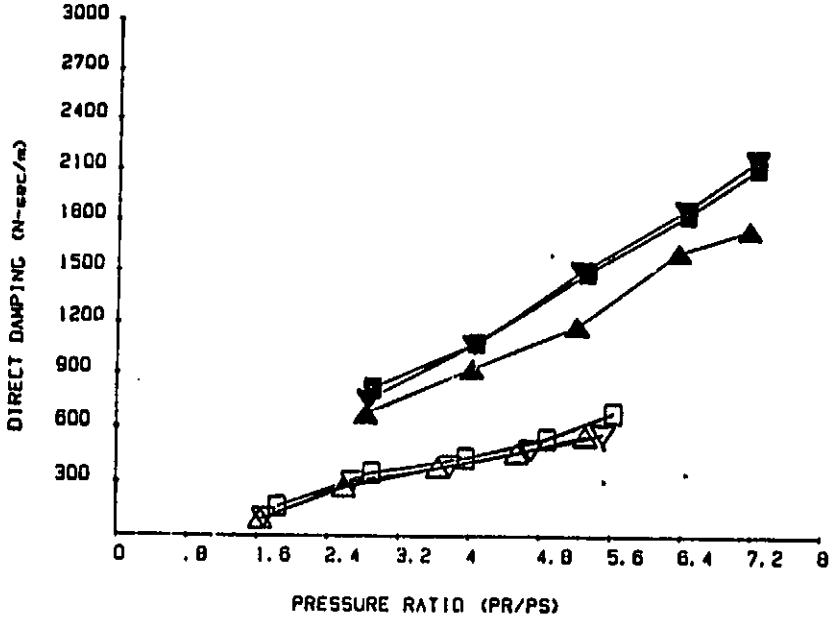

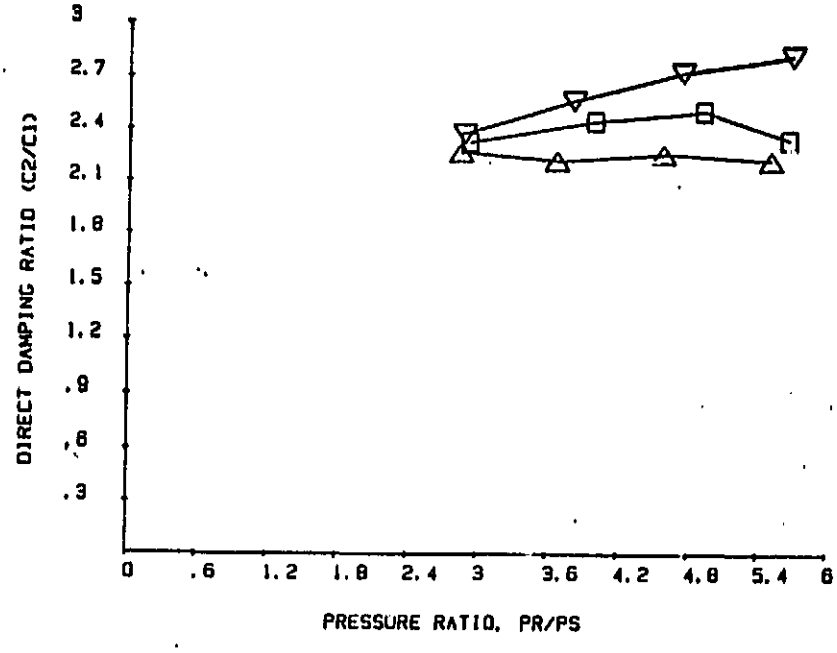

Fig. 80. Direct damping comparison of seals C1 and C2.

The magnitude of the cross-coupled damping of C1 exceeds that of C2 for prerotation with rotor rotation (Fig. 81). The ratio in this case increases from 0.4 to 0.9 as the pressure ratio increases. For the other prerotation cases, the cross-coupled damping of C2 exceeds that of C1. In fact, the non-prerotated cross-coupled damping of C2 exceeds the cross-coupled damping of C1 with prerotation counter to rotor rotation. The ratio of the damping of C2 to that of C1 for pre-rotation against rotor rotation is from 2.1 to 2.4.

When comparing rotordynamic coefficients of the two constant clearance seals, one must recall that, although C2 has considerably greater direct stiffness and damping for a given pressure ratio and swirl condition, it also has only 55% of the radial clearance in which to move. Therefore, a statement like "stiffer is better" would oversimplify the comparison.

Dynamic Results - C1 vs. T. The exit clearances of seals C1 and T are the same - 29 mils. Seal T differs from C1 only in its taper (Table 3). A comparison of the rotordynamic coefficients of the two seals reveals the effect of the particular taper (entrance clearance / exit clearance = 1.55) of T. The symbols used in Figs. 82-85 are defined in Table 6.

In Fig. 82, the ratio of the direct stiffness of T to that of C1 varies the least for prerotation with rotor rotation: from 1.14 to 1.55 for a reservoir pressure / sump pressure ratio from 1.7 to 5.1. For no prerotation, the ratio increases from 1.53 to 2.69. For prerotation counter to rotor rotation, the ratio is between 1.64 and 2.43.

The cross-coupled stiffness of T is less than that of C1 for all

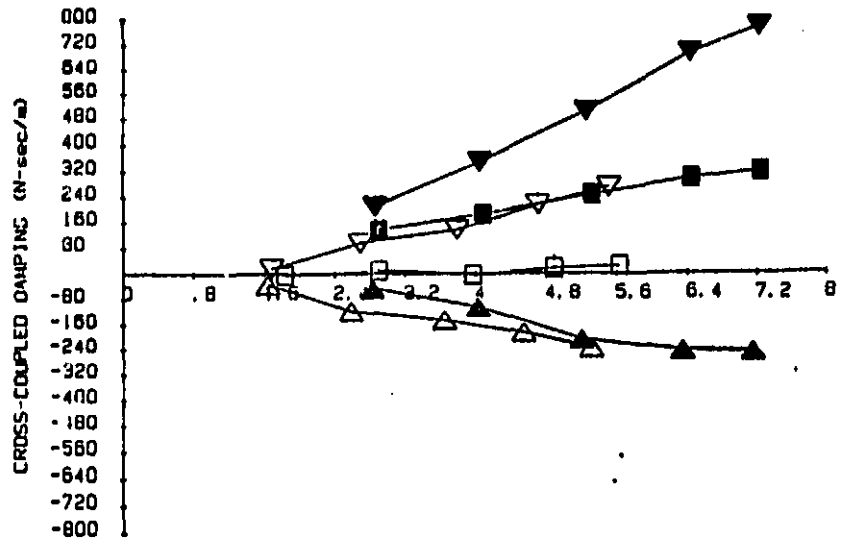

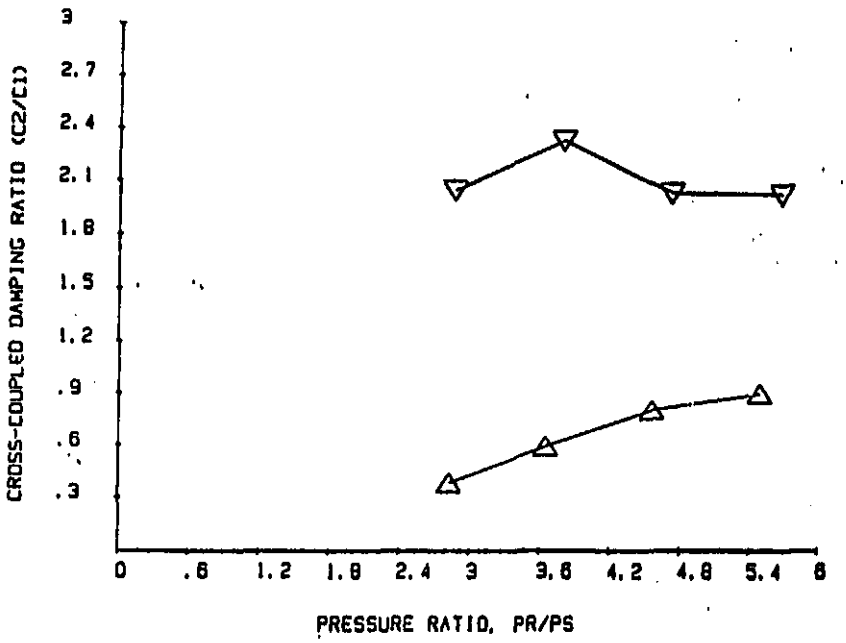

Fig. 81. Cross-coupled damping comparison of seals C1 and C2.

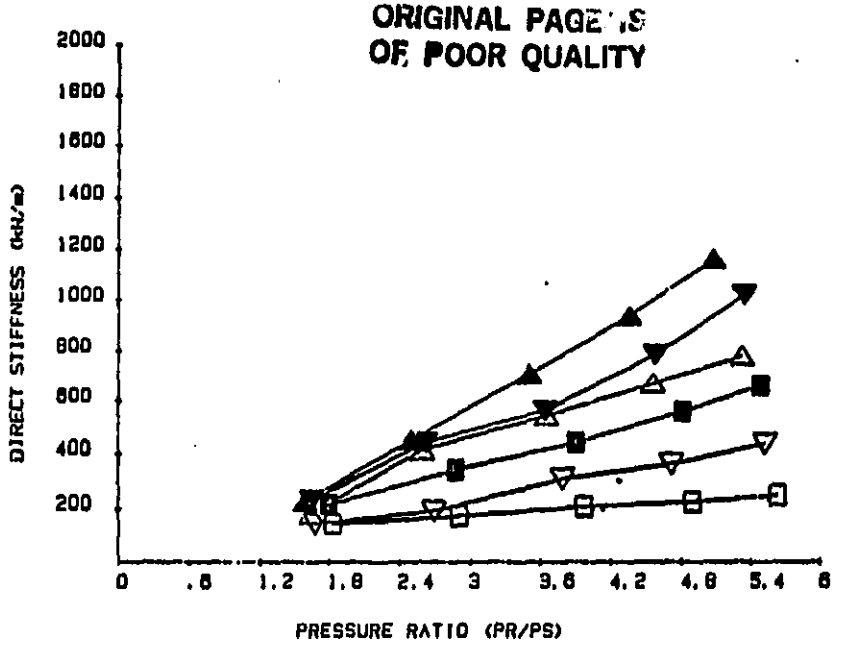

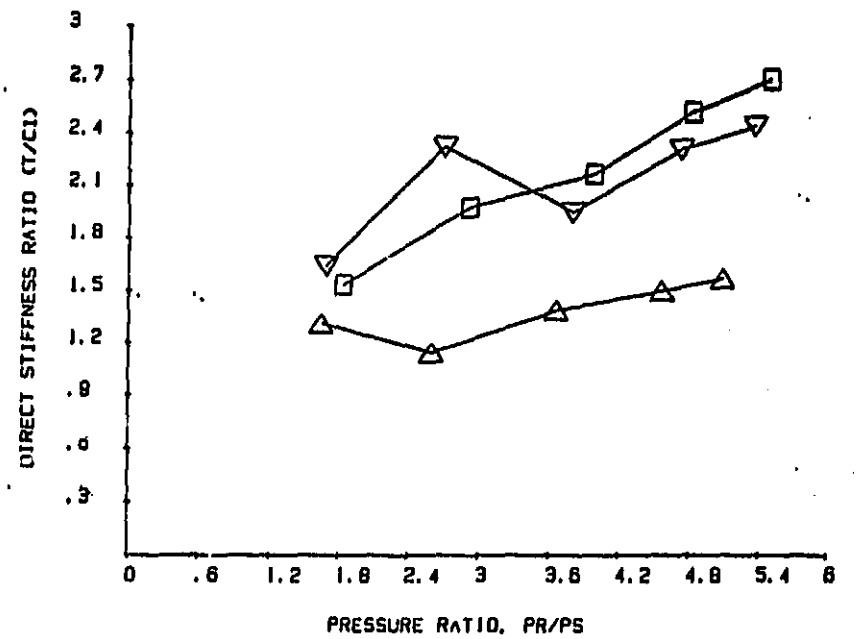

Fig. 82. Direct stiffness comparison of seals C1 and T. (C1: 29 mil clearance seal; T: tapered seal)

prerotation cases (Fig. 83). At each comparison pressure, the ratio of the cross-coupled stiffness of T to that of C1 with prerotation in the direction of rotor rotation is only slightly less than for counter prerotation. The range of stiffness ratios for these two cases is from 0.56 to 0.76 and from 0.69 to 0.86, respectively.

The direct damping of T is slightly less than that of C1 at low pressure ratios for all prerotation cases (Fig. 84). At the higher pressure ratios, the damping of T is higher than that of C1 for prerotation in the direction of rotor rotation, lower for no prerotation, and about equal for prerotation opposite rotor rotation. The ratios (T / C1) for these three swirl cases are from 0.7 to 1.2, from 0.7 to 0.9, and from 0.7 to 1.0, respectively.

Fig. 85 shows the relationship between the cross-coupled damping of seals T and C1. For both cases of prerotation, the cross-coupled damping of T is less than that of C1 for all pressure ratios. For prerotation with rotor rotation, the ratio of the cross-coupled damping of T to that of C1 is 1.0 for the lowest pressure ratio and drops to between 0.5 and 0.6 for all other pressure ratios. For prerotation against rotor rotation, the ratio is about 0.35 for the two lower pressure ratios plotted, and about 0.6 for the higher pressure ratios.

The additional direct stiffness and lower cross-coupled stiffness of the tapered seal compared to the constant 29 mil clearance seal indicates greater stability of the tapered seal. Leakage of the tapered seal, however, is about 10% greater than leakage of the constant clearance seal (Fig. 40).

Another method of comparing the dynamic coefficients of the seals

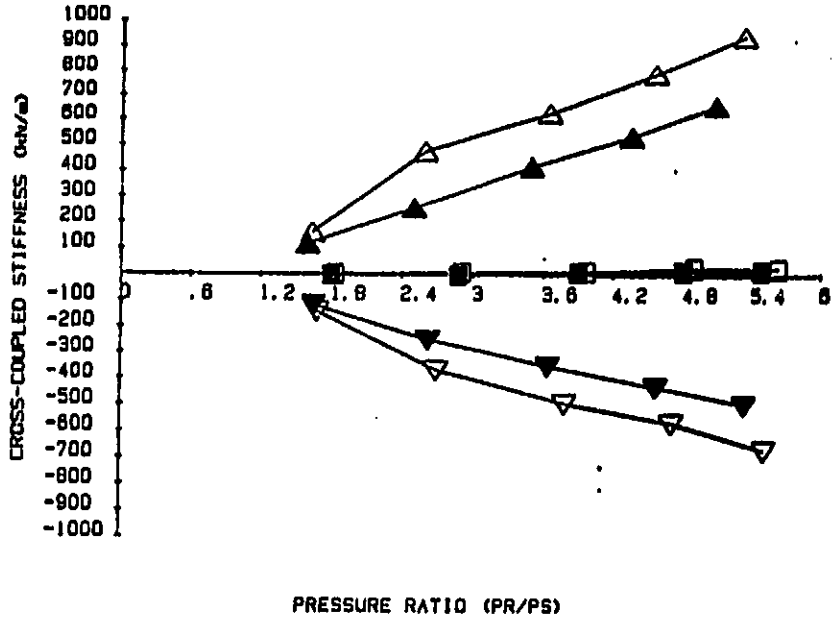

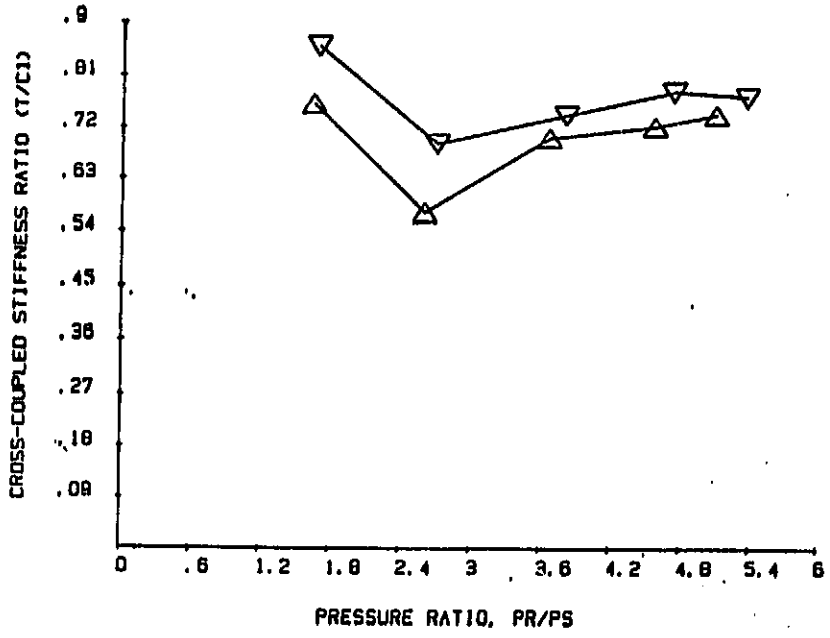

Fig. 83. Cross-coupled stiffness comparison of seals C1 and T.

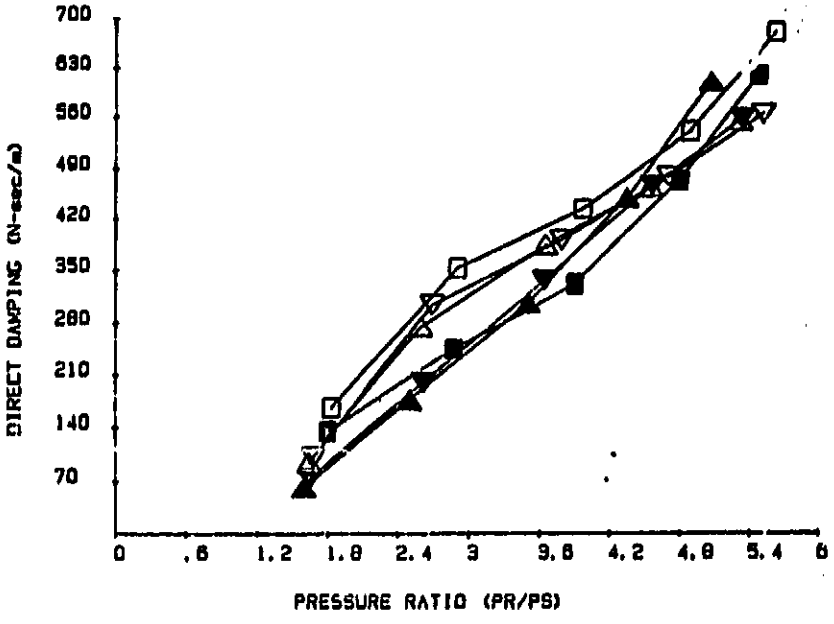

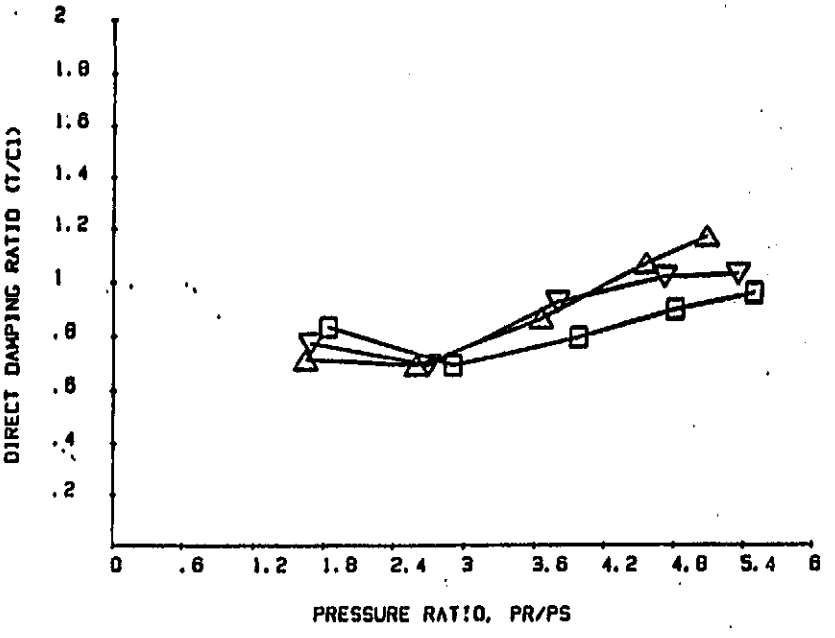

Fig. 84. Direct damping comparison of seals C1 and T.

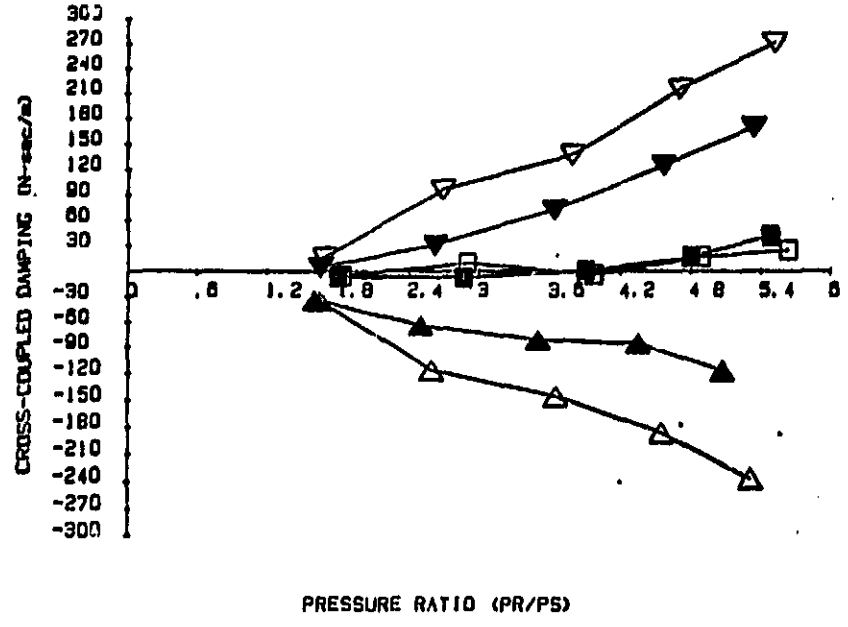

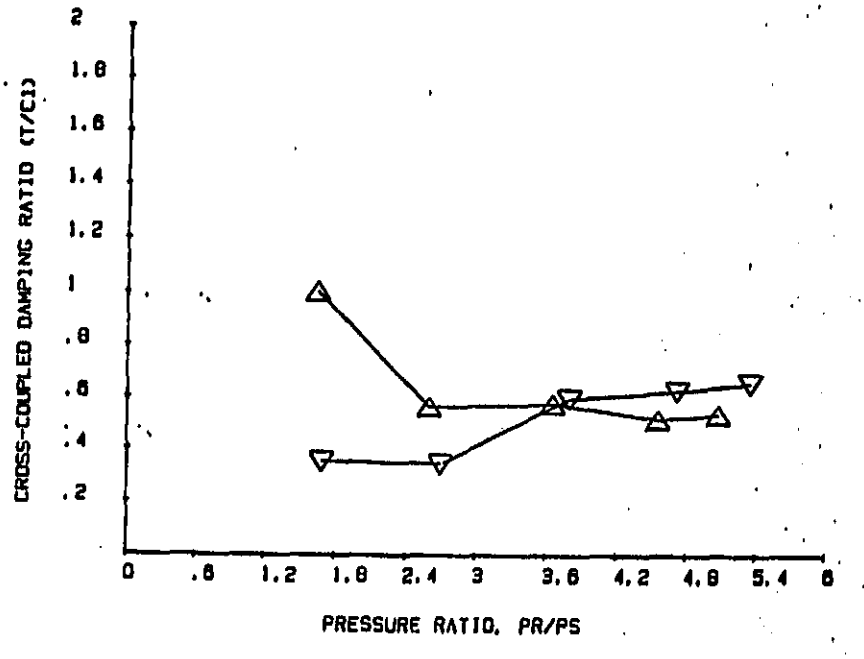

Fig. 85. Cross-coupled damping comparison of seals C1 and T.

is through their respective non-dimensional whirl frequency ratios. Whirl frequency ratio is defined

$$\text{Whirl frequency ratio} = k / C\Omega ,$$

where Ω is the shaking frequency. This ratio is a measure of the destabilizing influence of the cross-coupled stiffness with respect to the stabilizing influence of the direct damping. Generally, a lower positive whirl frequency ratio means a more stable seal. A negative whirl frequency ratio represents a tangential force which opposes forward whirl. Plots of whirl frequency ratio versus running speed with no prerotation are included in Figs. 86-89. The plots for the two constant clearance smooth seals and the convergent tapered seal show small positive whirl frequency ratios over most of the running speed range. Over this speed range, the order of decreasing whirl frequency ratio for these three seals is: C2, C1, T. However, the difference in ratios among the seals is small. In contrast, the honeycomb seal plot shows a negative whirl frequency ratio. The negative sign arises due to a negative cross-coupled stiffness. This negative k exerts a stabilizing influence, resulting in a force which acts in the same direction as the damping force.

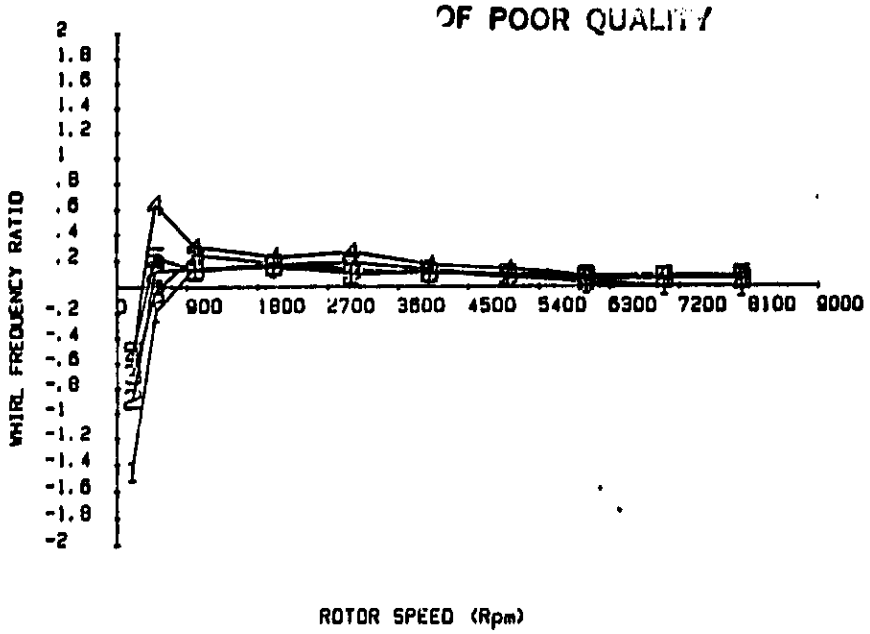

Fig. 86. Whirl frequency ratio of seal C1 (29 mil clearance) - no prerotation of inlet air.

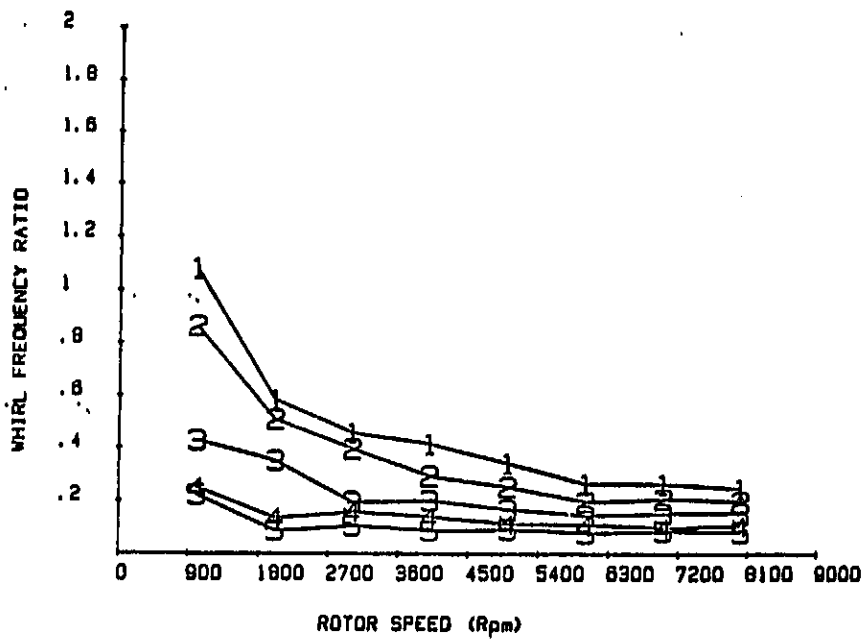

Fig. 87. Whirl frequency ratio of seal C2 (16 mil clearance) - no prerotation of inlet air.

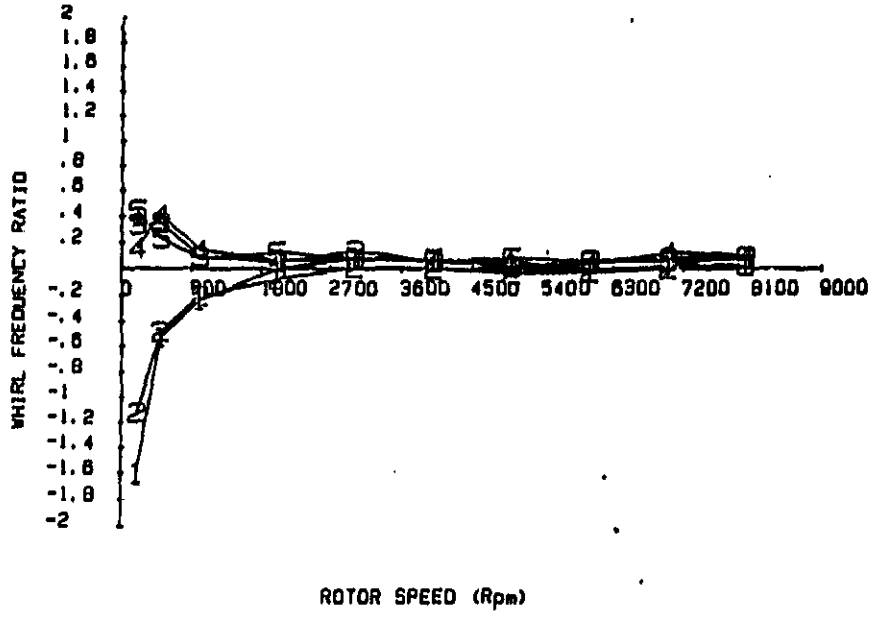

Fig. 88. Whirl frequency ratio of seal T (tapered) - no prerotation of inlet air.

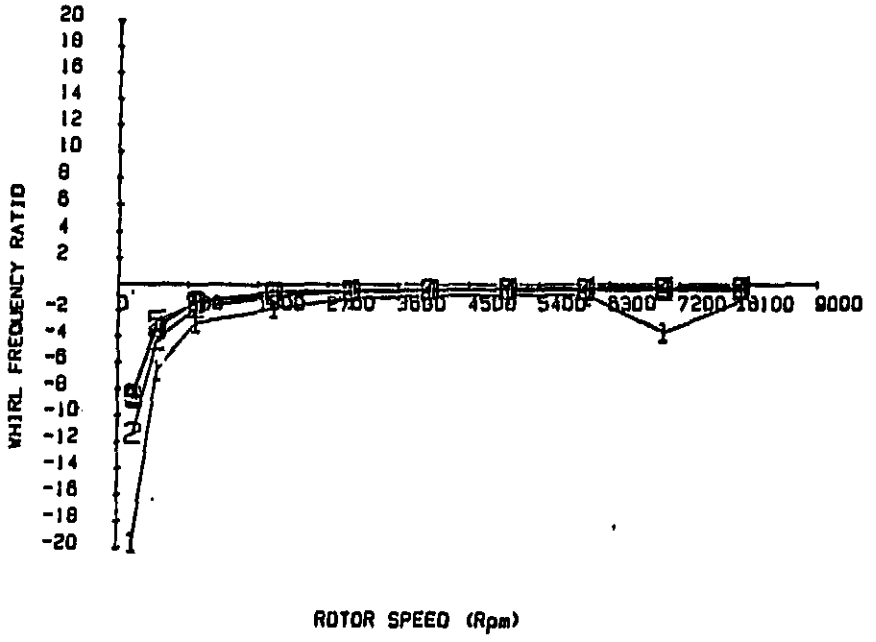

Fig. 89. Whirl frequency ratio of seal H (honeycomb) - no prerotation of inlet air.

CONCLUSIONS

A seal-test facility has been developed for the study of various types of gas seals. A method of determining rotordynamic coefficients has been established, and consistent, repeatable results have been obtained. After some initial failures in the test apparatus, reliability has been satisfactory, and a complete set of experimental results can be acquired in a matter of days.

The experimental and theoretical results of the preceding section support the following conclusions:

(a) Theoretical results for leakage are consistent with test results. Agreement between theory and experiment is satisfactory, with predictions being less than experimental results by 9% or less.

(b) Experimental and theoretical results for the pressure distributions and entrance-loss coefficients are relatively insensitive to running speed for the ranges (0-8500 rpm) and seals tested to date.

(c) In the test results for the honeycomb seal, the steep entrance pressure-loss seems to extend partially inside the seal. Also, the measured pressure at the exit of the seal generally equals the back pressure, rather than being greater, as is predicted by compressible flow theory for choked flow. Visual inspection revealed that the last pressure quill in the honeycomb is actually downstream of the effective seal due to manufacturing techniques, and therefore should measure the back pressure. These phenomena do not occur for the other seals.

(d) Test results for the direct stiffness of all seals show much

greater sensitivity to fluid prerotation than predicted by theory. Prerotation of the fluid (in either direction) results in measured direct stiffnesses which are significantly larger than for no prerotation. An exception is the constant 16 mil clearance smooth seal, which has significantly larger direct stiffnesses only for prerotation with rotor rotation. Theory predicts the direct stiffness to be less sensitive to fluid prerotation than it is. Furthermore, theory incorrectly predicts the relative effect on direct stiffness of changing the swirl configuration.

(e) Theoretical predictions of the influence of fluid prerotation on cross-coupled stiffness and damping are consistent with the test results. In general, theory underpredicts the magnitudes of these cross-coupled coefficients, while correctly predicting their trends with respect to prerotation.

(f) Agreement between theory and test results for the direct damping coefficients is favorable.

(g) Over the speed range tested, none of the rotordynamic coefficients show appreciable sensitivity to the rotational speed of the rotor. This may be due to the lack of development of significant shear forces in the seal. It appears that running speeds above those attained to date may be necessary to produce significant shear force effects.

(h) The effect on leakage and dynamic coefficients of reducing the clearance of a constant clearance smooth seal is shown by a comparison of the test results of the 29 mil clearance and 16 mil clearance seals. The leakage is reduced by 55% to 60%, while the coefficients generally increase. The percentage increase is seen to

depend on the swirl configuration except in the case of direct damping where the increase is about 150%.

(j) The leakage and dynamic coefficients of a constant 29 mil clearance smooth seal are compared to those of a convergent tapered smooth seal with an inlet to outlet clearance ratio of 1.55 and outlet radial clearance of 29 mils. The leakage of the tapered seal exceeded that of the constant clearance seal by about 10%. The direct stiffness of the tapered seal was higher; the direct damping was generally slightly lower, and the magnitude of the cross-coupled coefficients was lower. This indicates the tapered seal was slightly more stable with slightly more leakage.

(k) For the non-prerotated case, only the honeycomb seal has a negative cross-coupled stiffness, while k for all other seals is positive. The negative cross-coupled stiffness of the honeycomb seal, and hence negative whirl frequency ratio, indicates that the stability performance of the honeycomb seal is more favorable than that of the other seals.

REFERENCES

1 Black, H.F., and Jenssen, D.N., "Dynamic Hybrid Properties of Annular Pressure Seals," Proc. J. Mech. Engin., Vol. 184, pp. 92-100, 1970.

2 Jenssen, D.N., "Dynamics of Rotor Systems Embodying High-Pressure Ring Seals," Ph.D. dissertation, Herriot-Watt Univ., Edinburgh, Scotland, July 1970.

3 Black, H.F., and Jenssen, D.N., "Effects of High-Pressure Ring Seals on Pump Rotor Vibrations," ASME Paper No. 71-WA/FF-38, 1971.

4 Childs, D.W., "The Space Shuttle Main Engine High-Pressure Fuel Turbopump Rotordynamic Instability Problem," ASME Trans. J. of Engineering for Power, pp 48-57, Jan. 1978.

5 Childs, D.W., and Moyer, D.S., "Vibration Characteristics of the HPOTP (High-Pressure Oxygen Turbopump) of the SSME (Space Shuttle Main Engine)," ASME Paper No. 84-GT-31, 29th International Gas Turbine Conference and Exhibit. Amsterdam, 1984.

6 Black, H.F., Allaire, P.E., and Barrett, L.E., "The Effect of Inlet Flow Swirl on the Dynamic Coefficients of High-Pressure Annular Clearance Seals," Ninth International Conference in Fluid Sealing, BHRA Fluid Engineering, Leeuwonhorst, The Netherlands, Apr. 1981.

7 Childs, D.W., "Finite-Length Solutions for Rotordynamic Coefficients of Turbulent Annular Seals," ASME J. of Lubrication Technology, Vol. 105, pp. 437-444, July 1983.

8 Hirs, G.G., "A Bulk-Flow Theory for Turbulence in Lubricant Films," ASME Journal of Lubrication Technology, Vol. 95, pp. 137-146, April 1973.

9 Fleming, D.P., "Stiffness of Straight and Tapered Annular Gas Path Seals," ASME Journal of Lubrication Technology, Vol.101, pp. 349-355, July 1979.

10 Fleming, D.P., "Damping in Ring Seals for Compressible Fluids," NASA CP 2133, Rotordynamic Instability Problems in High-Performance Turbomachinery, proceedings of a workshop held at Texas A&M University, 12-14 May 1980, pp. 169-188.

11 Nelson, C.C., "Rotordynamic Coefficients for Compressible Flow in Tapered Annular Seals," Mechanical Engineering Dept., Texas A&M University.

12 Nelson, C.C., "Analysis for Leakage and Rotordynamic Coefficients of Surface-Roughened Tapered Annular Gas Seals," ASME Paper No. 84-GT-32, 1984. Texas A&M University.

13 Benckert, H., and Wachter, J., "Flow Induced Spring Coefficients of Labyrinth Seals for Application in Rotor Dynamics," NASA CP 2133, Rotordynamic Instability Problems in High-Performance Turbomachinery, proceedings of a workshop held at Texas A&M University, 12-14 May 1980.

14 Childs, D.W., and Dressman, J.B., "Testing of Turbulent Seals for Rotordynamic Coefficients," NASA CP 2250, Rotordynamic Instability Problems in High-Performance Turbomachinery, proceedings of a workshop held at Texas A&M University, 10-12 May 1982.

15 Chameih, D.S., Acosta, A.J., Brennen, C.E., Caughey, T.K., and Franz, R., "Experimental Measurement of Hydrodynamic Stiffness Matrices for a Centrifugal Pump Impeller," NASA CP 2250, Rotordynamic Instability Problems in High-Performance Turbomachinery, proceedings of a workshop held at Texas A&M University, 10-12 May 1982.

16 Shoji, H., and Ohashi, H., "Lateral Fluid Forces Acting on a Whirling Centrifugal Impeller in Vaneless and Vaned Diffuser," presented at the Third Workshop on Rotordynamic Instability Problems in High-Performance Turbomachinery, 28-30 May 1984.

17 Adams, M.L., and Makay, E., "Measurement of Interstage Fluid-Annulus Dynamical Properties," NASA CP 2250, Rotordynamic Instability Problems in High-Performance Turbomachinery, proceedings of a workshop held at Texas A&M University, 10-12 May 1982.

18 Iino, T., and Kaneko, H., "Hydraulic Forces Caused by Annular Pressure Seals in Centrifugal Pumps," NASA CP 2133, Rotordynamic Instability Problems in High-Performance Turbomachinery, proceedings of a workshop held at Texas A&M University, 12-14 May 1980.

19 Bowen, W.L., and Bhateje, R., "The Hollow Roller Bearing," ASME Paper No. 79-Lub-15, ASME-ASLE Lubrication Conference; Dayton, Ohio, 16-18 October 1979.

20 Cohen, H., Rogers, G.F.C., and Saravanamuttoo, H.I.H., Gas Turbine Theory, Longman Group Limited, 1972.

21 Childs, D.W., "Finite-Length Solution for the Rotordynamic Coefficients of Convergent-Tapered Annular Seals," 3rd International Conference on Vibrations in Rotating Machinery, 11-13 Sep., 1984.

22 Holman, J.P., Experimental Methods for Engineers, McGraw Hill, 1978, pg. 45.